

FERMILAB-THESIS-1988-01

Order Number 8916308

**Study of muons associated with jets in proton-antiproton
collisions at $\sqrt{s} = 1.8$ TeV**

Smith, David Austen, Ph.D.

University of Illinois at Urbana-Champaign, 1989

STUDY OF MUONS ASSOCIATED WITH JETS
IN PROTON-ANTIPROTON COLLISIONS
AT $\sqrt{s} = 1.8$ TeV

BY

DAVID AUSTEN SMITH

B.A., University of California, Berkeley, 1981
M.S., University of Illinois, 1982

THESIS

Submitted in partial fulfillment of the requirements
for the degree of Doctor of Philosophy in Physics
in the Graduate College of the
University of Illinois at Urbana-Champaign, 1989

Urbana, Illinois

UNIVERSITY OF ILLINOIS AT URBANA-CHAMPAIGN

THE GRADUATE COLLEGE

November 22, 1988

WE HEREBY RECOMMEND THAT THE THESIS BY

David Austen Smith

ENTITLED Study of Muons Associated With Jets in Proton-Antiproton

Collisions at $\sqrt{s} = 1.8$ TeV

BE ACCEPTED IN PARTIAL FULFILLMENT OF THE REQUIREMENTS FOR

THE DEGREE OF Doctor of Philosophy

Director of Thesis Research

Head of Department

Head of Department

Committee on Final Examination†

Chairperson

† Required for doctor's degree but not for master's.

STUDY OF MUONS ASSOCIATED WITH JETS
IN PROTON-ANTIPROTON COLLISIONS
AT $\sqrt{s} = 1.8$ TeV

David Austen Smith, Ph.D.
Department of Physics
University of Illinois at Urbana-Champaign, 1989
Professor L.E. Holloway, advisor

Production of heavy quark flavors in proton-antiproton collisions with a center-of-mass energy of 1.8×10^{12} electron volts is studied for events containing hadronic jets with a nearby muon track, where both the jet and the muon are produced at large angles from the incident beams. The muon tracking system and pattern recognition are described. Detailed calculations of the muon background due to meson decay and hadron noninteractive punchthrough are presented, and other background sources are evaluated. Distributions of muon transverse momentum relative to the beam and to the jet axis agree with QCD expectations for semileptonic charm and beauty decay. Muon identification cuts and background subtraction leave 57.5 ± 17.1 muon-jet pairs, a rate consistent with the established production cross sections for charm and beauty quarks and the acceptance for minimum ionizing particles overlapping with nearby jets. A small dimuon sample clarifies the muon signature. No signatures of undiscovered phenomena are observed in this new energy domain.

Acknowledgments

I am grateful to all my teachers. Every person who has been able to share some knowledge or insight with me will stay in my heart throughout my life. During my years in Urbana there have been many and I gladly mention some of the most prominent.

As advisor and ally, Professor Lee Holloway has been a model in his mastery of experimental physics. Dr. Tom Westhusing has been a staunch friend and accomplice and I am proud to have teamed with him in building our huge tracking system. Mr. V.J. Simaitis' work as design engineer for the chambers and associated electronics was indispensable, and I thank him for many valuable lessons. The smooth operation of our computing systems is a tribute to the professionalism and personal grace of Messrs David Lesny and Jerry Wray. This research was supported in part by the U.S. Department of Energy under contract DE-AC02-76ERO1195.

Greatest thanks go to my mother as my first and most faithful teacher.

Contents

1	Motivation	1
1.1	Why Study Muons and Jets?	1
1.2	Beauty at the Fermilab Collider	2
1.2.1	The Standard Model	2
1.2.2	Heavy Quark Production	3
1.2.3	Muon Rates	5
1.3	Signatures and Backgrounds	10
1.3.1	Momentum Transverse to the Jet Axis, p_t^{rel}	10
1.3.2	Muons from Other Processes	16
1.3.3	Fake Muons	17
1.4	Outline of the Thesis	17
2	Apparatus	19
2.1	The Tevatron	19
2.1.1	Luminosity	19
2.1.2	Colliding Beams	22
2.2	The Collider Detector Facility	24
2.2.1	Overview of the Detector	24
2.2.2	Central Tracking	24
2.2.3	Calorimetry	32
2.3	Central Muon Chambers	37
2.3.1	Principles of Operation	37
2.3.2	Geometry	37
2.3.3	Mechanical Details	43
2.3.4	Main Ring Background	45
2.4	Data Acquisition Electronics	45
2.4.1	Overview	45

2.4.2	Rabbit Electronics System	47
2.4.3	The Muon ADC/TDC card	49
2.4.4	Vax and MX	50
2.4.5	System Calibration	53
2.5	Trigger	56
2.5.1	Brass Muons	57
2.5.2	Golden Muons	59
2.5.3	Jet Triggers	62
3	Muon Identification at CDF	64
3.1	Muon Signatures	64
3.1.1	Matching Cuts	64
3.1.2	Minimum Ionization Cut	69
3.1.3	Acceptance	71
3.2	Fake Muons	73
3.2.1	Noninteractive Punchthrough and Decay-in-Flight	73
3.2.2	Other Sources	80
4	Data Analysis	83
4.1	Event Selection	83
4.1.1	Data Samples	83
4.1.2	Jet Algorithm	83
4.2	Prompt Muons	84
4.3	Momentum Transverse to the Jet Axis, p_t^{rel}	87
5	Conclusion	92
5.1	The Past	92
5.2	The Future	93
A	Coordinate Systems	94
A.1	CDF Global Coordinates	94
A.2	Local Wedge Coordinates	94
B	Noninteractive Punchthrough Probability	96
B.1	Motivation	96
B.2	Sources	99
B.3	Central Calorimeter Test Beam Data	102

B.3.1	Data Sample	102
B.3.2	Analysis for (EM + Hadron)	105
B.3.3	Analysis for the EM Shower Counter	108
B.4	Λ_{wedge} Calculations	108
B.4.1	Central Hadron	109
B.4.2	Central EM	109
B.4.3	Entire Wedge	110
B.5	Low Energy Extrapolation	111
B.6	Muon Background Charge Asymmetry	113
B.7	Conclusion	117
C	Decay-in-Flight Acceptance	118
C.1	Why Use the Monte Carlo?	118
C.2	The Method	120
C.2.1	Event Generation	120
C.2.2	Track Reconstruction	122
C.3	Sample Calculations	124
C.3.1	Flat Input Spectrum	124
C.3.2	Jet $\frac{dN}{dp_t}$ Distribution	125
C.3.3	Do-It-Yourself	125
C.4	Charge Asymmetry	127
C.5	Conclusions	128
D	Dimuons	129
D.1	Generalities	129
D.2	Invariant Mass Distribution	130
D.3	Like and Unlike Charge Ratios	132
E	Rabbit Testing	135
	Bibliography	141
	Vita	145

List of Tables

1.1	Two-to-two parton subprocesses. The third column gives the value of $ A ^2$ at 90° at 2 TeV. The gg process dominates.	4
1.2	Properties of the charm and beauty mesons.	5
1.3	Efficiency of jet trigger for semileptonic B decay.	10
2.1	List of rates.	21
2.2	Accelerator parameters.	23
2.3	Calorimetry Characteristics	33
2.4	Drift Cell Parameters.	38
2.5	Typical Parameters of the ADC/TDC card.	50
2.6	List of Calibration Constants.	53
3.1	Muon identification cuts.	65
3.2	Fraction of heavy particles in charged track spectrum.	76
4.1	Muon candidates and background subtraction.	87
B.1	Parameters for the power-law fit to the A-dependence of the absorption cross-section for 60 GeV/c particles.	97
B.2	Absorption cross sections (mb) and lengths (cm) for 60 GeV/c hadrons incident on different targets.	103
B.3	Material thicknesses and numbers of absorption lengths for the components of the central electromagnetic shower counter. Notes are given in the text. .	109
B.4	Total number of absorption lengths per wedge, Λ_0 , such that $\Lambda = \Lambda_0 / \sin(\theta)$, for 60 GeV/c hadrons.	110
B.5	Fit parameters for the momentum dependence of Λ_0	112
C.1	Some properities of kaons and pions. $R_{mu} = 347$ cm is the radius of the central muon chambers. $B.R.$ is the branching ratio to $\mu\nu$	119

C.2	Values of the cuts made on the CTC tracks, and on the match between the CTC track and the CMU stub. The parameters are described in the text. .	122
E.1	Abbreviated checklist for testing the Muon ADC/TDC Rabbit cards. . . .	140

List of Figures

1.1	Feynmann diagrams for heavy flavor production	4
1.2	Heavy flavor cross sections using ISAJET lowest order calculations.	6
1.3	Predicted transverse momentum distributions of quarks, mesons, and muons in $b\bar{b}$ and $c\bar{c}$ production [13].	7
1.4	Fraction of heavy flavor muons coming from charm decay.	8
1.5	The decay $B \rightarrow \mu X$, showing the momentum component p_t^{rel} transverse to the jet axis, and the variables for the simplified calculation.	11
1.6	Muon p_t^{rel} measured by UA1. Solid curves come from Isajet. p_t^{rel} for muons from B decay is larger than for charm decay.	12
1.7	QCD calculation of the B meson momentum transverse to the beam	14
1.8	Muon momentum spectrum from the decay $B \rightarrow \mu X$, in the B rest-frame, as measured in e^+e^- collisions by the Argus collaboration.	15
1.9	Muon p_t^{rel} spectrum for muons from $B \rightarrow \mu X$, calculated using the simpli- fied model.	15
2.1	Peak luminosity for each $p\bar{p}$ store, versus day number into the run. Day 1 is February 1, 1987. The peak value exceeded the goal for this run of $\mathcal{L}_0 = 10^{29} \text{ cm}^{-2} \text{ s}^{-1}$	20
2.2	Isometric view of the CDF detector.	25
2.3	Elevation view of the CDF detector.	26
2.4	Graphics display of an event in the Central Tracking Chamber.	28
2.5	Graphics rz -view of an event, beam in the plane of the page. Tracks in the VTPC, stereo CTC hits, calorimeter response and muon hits are all shown. . . .	30
2.6	Central calorimeter 'wedge'. Note the opening for the muon chambers. . . .	35
2.7	Central wedge shown in relation to the rest of the central detector.	36
2.8	Cross section of a single module of the central muon chambers. There are three modules per wedge.	39

2.9	Drift velocity in argon-ethane gas mixture, as a function of field strength. Muon chamber cells are designed so that v_{drift} is always above the ‘knee’ of the curve.	40
2.10	Electric field profile inside a cell of the central muon chambers. Drift velocity is roughly constant for field strengths above minimum value.	41
2.11	Circuit used in the end-electronics to extract the charge pulses from the chamber wires. Pulses are sent directly into the MAT card.	43
2.12	Plot of main ring beam intensity and muon chamber anode current. Chamber current soars at beam injection and extraction times due to beam losses and consequent radiation.	46
2.13	Overview of the central muon electronics system, showing both the data and trigger paths from the chambers, through the front-end electronics, and into the FastBus network.	48
2.14	Simplified schematic of the muon charge-to-voltage converter and the time-to-voltage converter circuits (QVC and TVC).	51
2.15	Muon ADC/TDC timing.	52
2.16	Distribution of δ used to measure the drift velocity.	55
2.17	Overview of the electronics for the Golden muon trigger. Drift time information from both the central muon chambers and the central tracking chamber is translated into stub and track coordinates, which are matched in the muon matchbox.	57
2.18	Relation between track curvature, transverse momentum, and track angle at the muon chambers.	58
2.19	Trigger level 1 gate width as a function of gate setting. Useful in conjunction with the following plot.	59
2.20	p_t threshold vs the cut on the drift time difference for alternate layers, ignoring multiple scattering.	60
2.21	Brass trigger efficiency for multiply scattered muons of transverse momentum p_t	60
2.22	Jet differential cross section for different $\sum E_t$ trigger thresholds.	63
3.1	Raw dx distribution for muon candidates. Vertical lines show cut.	65

3.2	dx distributions after dz and minimum ionizing cuts, for different p_t thresholds.	66
3.3	Correlation of the matching parameters $d\alpha$ and dx	68
3.4	Raw $d\alpha$ distribution for muon candidates (bold) and after dx cuts (light). Vertical lines show the $d\alpha$ cuts.	70
3.5	Raw dz distribution for muon candidates, showing cuts.	70
3.6	Sum of EM and Hadron energies for muons passing the matching cuts. . . .	71
3.7	Hadron vs. EM energy for CTC/Muon matches after the dx , dz and $d\alpha$ cuts.	72
3.8	Azimuth angle distribution of muon-candidates, showing inefficiency due to Main Ring background.	73
3.9	p_t distribution for all charged tracks from the jet data, scaled to the geometric acceptance of the muon chambers.	74
3.10	Charged track transverse momenta for events with a jet above different transverse energy thresholds.	75
3.11	Muon background for different K/π ratios. Dashed line is the decay-in-flight contribution, dotted line shows noninteractive punchthrough with typical error bars due to the uncertainty in the absorption cross sections, and solid line is the sum of the two.	77
3.12	Same as preceding figure, except that the minimum ionization cut has been applied to the parent tracks.	77
3.13	Total background (decay + noninteractive) for different K/π , comparing magnitude of uncertainty due to K/π error with uncertainty from absorption length error.	79
3.14	Fraction of jets with an associated CTC/stub match.	81
4.1	Momentum distribution of muon candidates from the $jet \cdot \mu$ data, before the minimum ionizing cut. Region within the dashed lines is the expected background from decay-in-flight and noninteractive punchthrough.	85
4.2	Momentum distribution of muon candidates from the $jet \cdot \mu$ data, after the minimum ionizing cut. Region within the dashed lines is the expected background from decay-in-flight and noninteractive punchthrough.	86

4.3	Differences in pseudorapidity and azimuth angle between matched jets and muons, showing the $\Delta\phi$ cut.	88
4.4	Momentum component transverse to the jet axis for muon candidates and for background tracks, before the minimum ionization cut.	90
4.5	Same as preceding figure, after the minimum ionizing cut.	90
4.6	Probability, in percent, for a charged track to appear as a muon candidate. Lines are to guide the eye.	91
A.1	The CDF coordinate system.	95
B.1	Meson-proton cross sections as a function of meson energy, taken from the Particle Data Group. In each plot, the top curve is σ_{total} , the bottom curve is $\sigma_{elastic}$, and the third curve comes from subtracting the fits to the first two, $\sigma_{inelastic} = \sigma_{total} - \sigma_{elastic}$	98
B.2	Particle Data Group Proton-proton (left) and antiproton-proton (right) cross sections as a function of energy. Curves are as in preceding figure. . .	100
B.3	Pi-iron inelastic cross sections from the various authors. Absorption lengths (CDHS) or interaction probabilities (CITF) have been converted to cross sections. The solid curve is $(\sigma_{\pi^+p} + \sigma_{\pi^-p})/2$ from figure 1, to allow for the equal proton and neutron mix in iron, scaled to match Denisov at 30 GeV.	102
B.4	Total (EM + Hadron) pulse height distribution of 57.1 GeV μ^+ 's at tower 2 center (coarse binning). Note the 92 underflow entries.	103
B.5	Total (EM + Hadron) pulse height distribution of 57.1 GeV μ^+ 's at tower 2 center, with finer binning than figure 4.	104
B.6	(EM + Hadron) pulse height distribution of 57.1 GeV π^+ 's at tower 2 center, showing a small peak corresponding to minimum ionizing particles (non-interactive punchthrough and untagged muons). Note the 52 underflow entries.	105
B.7	Ratio $\frac{\pi}{\mu}$ of number of entries per bin in the pulse height distributions for pions and muons. Left-hand plot is for the total pulse height (EM + Hadron), right-hand plot is for the EM pulse height.	106
B.8	EM pulse height distribution of 57.1 GeV μ^+ 's at tower 2 center.	107
B.9	EM pulse height distribution of 57.1 GeV π^+ 's.	107

B.10	Number of absorption lengths at normal incidence on a central wedge for different hadrons.	112
B.11	Noninteractive punchthrough probability (right) and inverse probability (left) for hadrons incident on a central wedge, averaged over the η coverage of the central muon chambers. Includes $\frac{dE}{dx}$ correction.	113
B.12	Overall noninteractive punchthrough probability and inverse probability assuming $\frac{K}{\pi} = \frac{p+\bar{p}}{\pi} = 0.35$ (solid curve). Number of hadrons per noninteractive punchthrough is also shown (dashed curve).	114
B.13	Limits on predicted charge asymmetry for tracks in the muon chambers. a) $\frac{K}{\pi} = \frac{(p+\bar{p})}{\pi} = 0.10$, b) $\frac{K}{\pi} = \frac{(p+\bar{p})}{\pi} = 0.36$	116
C.1	Distribution of radii at which a parent meson decays into a muon. The solid curve (+’s) includes the dE/dx losses that slow down the parent mesons, thereby increasing the decay probability in the calorimeter. The dashed curve (X’s) is uncorrected. The two curves are the same until the beginning of the calorimeter ($r \simeq 150$ cm). The curves are only intended to guide the eye.	121
C.2	Transverse momentum distributions for muons from the decay of simulated kaons that pass the ‘loose’ matching cuts. Primary kaon p_t is shown in each plot.	123
C.3	Acceptance for muons from kaon decay-in-flight assuming a flat distribution of parent momenta. In the top curve, loose cuts for the match between the CTC track and the CMU stub have been applied, while the lower curve had tight cuts.	125
C.4	Transverse momentum distribution of observed decay muons, $(\frac{d\sigma_\mu}{dp_t})_{obs}$, based on a parent meson distribution similar to that of charged tracks in jet events. The contributions from pions and kaons are shown, together with the sum of the two, for two different particle mixtures.	126
C.5	Charge asymmetry in the central muon chambers. The curves combine non-interactive punchthrough with meson decay-in-flight. The solid curve includes the meson dE/dx losses in the calorimeter, while the dashed curve is uncorrected. The points come from 1987 muon data.	127

D.1	Invariant mass of unlike- and like-charge muon pairs.	131
D.2	Azimuth angle between the muons for unlike- and like-charge pairs.	133
D.3	Ratio of unlike-sign dimuons to like-sign pairs, for three ranges of the difference in azimuth angle between the two tracks. Single μ data provides a background estimate.	133
E.1	Illinois BlackBox (BBX) electronics used for reference timing in calibration and debugging of the Muon ADC/TDC cards.	136
E.2	Digitized QVC output voltage versus input charge, for eight QVC channels (artificial offsets for clarity).	138
E.3	Digitized TVC output voltage versus time of charge injection, for eight TVC channels (artificial offsets for clarity).	139

Chapter 1

Motivation

1.1 Why Study Muons and Jets?

The Collider Detector Facility, CDF, is a brand new instrument operating at the world's highest energy hadron collider, exploring a new domain. A wealth of new physics measurements are within CDF's reach. But before new natural phenomena can be observed, the detector's response to 'standard' physics must be understood.

Our group built, installed, and ran the muon tracking chambers covering the region between 55° and 125° from the beam axis. In the 1987 collider run, the chambers detected the muonic decays of the intermediate vector bosons, the W^\pm and Z^0 particles, for the first time in this new energy domain [2,3]. But the signature of $W \rightarrow \mu\nu$ is clean: processes that could fake an isolated, high momentum muon are rare. Any attempt to detect more ambiguous signals, which means any physics process producing a muon with transverse momentum $p_t < 20$ GeV/c, requires closer scrutiny ¹. This class of processes includes a tremendous range of important topics, where heavy flavor physics and the search for the Top quark head the list.

One way to understand the muon data at medium and low p_t is to study inclusive muons,

$$p\bar{p} \rightarrow \mu + \text{anything.}$$

Any $p\bar{p}$ collision generating a muon candidate is recorded, and then the data is compared with the calculated rates of all physics processes (charm and beauty decay, Drell-Yan, etc.) and all background processes (hadron punchthrough, meson decay-in-flight, etc.).

¹Throughout this thesis, transverse momentum p_t is always relative to the beam axis. p_t^{jet} is always the momentum component transverse to the jet axis.

Reconciling the data with the calculations results in a quantitative understanding of the detector performance.

Such a study is impractical with the 1987 data. The muon trigger, which selects which collisions are recorded, was commissioned during the run so no large data sample with a stable muon trigger exists. Fortunately, the calorimeter trigger accepted events where the total energy deposition in the detector was above some threshold, which includes events where

$$p\bar{p} \rightarrow \mu + \text{jets}.$$

This important subset of the inclusive muon data is enriched by the semileptonic decay of beauty mesons,

$$\begin{aligned} p\bar{p} \rightarrow b\bar{b} &\rightarrow \text{jet or } \mu^+ \bar{c} \bar{\nu} \\ &\hookrightarrow \mu^- c \nu, \quad c \rightarrow \text{jet} \end{aligned}$$

Beauty production provides several tests of elementary particle theory, including QCD cross section calculations and $B^0 \bar{B}^0$ oscillations². Beauty is the principal background in a search for the top quark, and hence beauty must be understood before top can be discovered. So a study of muons associated with jets leads to fundamental physics measurements and to an understanding of the detector performance.

1.2 Beauty at the Fermilab Collider

1.2.1 The Standard Model

The standard model of elementary particle physics, with its three generations of quarks and leptons,

$$\begin{array}{cccc} \begin{pmatrix} q = +2/3 \\ q = -1/3 \end{pmatrix} & \begin{pmatrix} u \\ d \end{pmatrix} & \begin{pmatrix} c \\ s \end{pmatrix} & \begin{pmatrix} t \\ b \end{pmatrix} \\ \begin{pmatrix} q = -1 \\ q = 0 \end{pmatrix} & \begin{pmatrix} e \\ \nu_e \end{pmatrix} & \begin{pmatrix} \mu \\ \nu_\mu \end{pmatrix} & \begin{pmatrix} \tau \\ \nu_\tau \end{pmatrix} \end{array}$$

is well known. These, along with the vector bosons γ , W^\pm , Z^0 that mediate the electroweak couplings and the gluons that carry the ‘color’ force have been described in detail many times and I will not repeat the exercise here [11,12].

²QCD is Quantum Chromodynamics, the theory of the strong force.

The discovery of the Upsilon meson (Υ) implies the existence of a third quark generation [10]. Hence a key test of the standard model is the discovery of the other member of the third quark doublet, the top quark. Top decays primarily to beauty. Hence, a search for top requires that we first understand beauty physics in hadron colliders.

But in its own right, beauty physics provides fertile ground for testing QCD. QCD predictions for charm production disagree with measurements by an order of magnitude, because the charm quark is too light compared to the QCD coupling constant α_s for perturbative methods to succeed. But the beauty quark is more massive than charm, and QCD calculations of beauty production agree more closely with experiment.

1.2.2 Heavy Quark Production

Mechanics

Figure 1.1 shows the dominant Feynmann diagrams for heavy quark production in $p\bar{p}$ collisions. To lowest order, the differential cross section comes from summing over the Born diagrams,

$$d\sigma(p\bar{p} \rightarrow BX) \approx \sum_{a,b} \int dx_1 dx_2 f_a(x_1, Q^2) f_b(x_2, Q^2) d\hat{\sigma}(ab \rightarrow b\bar{b}), \quad (1.1)$$

where $d\hat{\sigma}(ab \rightarrow b\bar{b})$ is the fundamental cross-section for a given process, and f_a and f_b are the proton structure functions [4]. The relative strengths of the subprocess cross sections $\hat{\sigma}$ are listed in table 1.1. Since gluon production is the most abundant QCD process, the 2^{nd} order process

$$gg \rightarrow gg, \quad g \rightarrow Q\bar{Q}$$

is an important contribution in spite of the suppression by a factor of α_s .

Detailed Calculations - ISAJET

Table 1.1 gives the magnitudes of the parton subprocesses, but calculating the total cross section for $p\bar{p} \rightarrow Q\bar{Q}$ is more difficult. The $\hat{\sigma}$'s have to be convoluted with the empirical structure functions of the p and \bar{p} to find the momentum distributions of the final parton. To calculate jet properties and lepton spectra requires the empirical fragmentation functions and a phenomenological treatment of the hadronization of the partons. Large

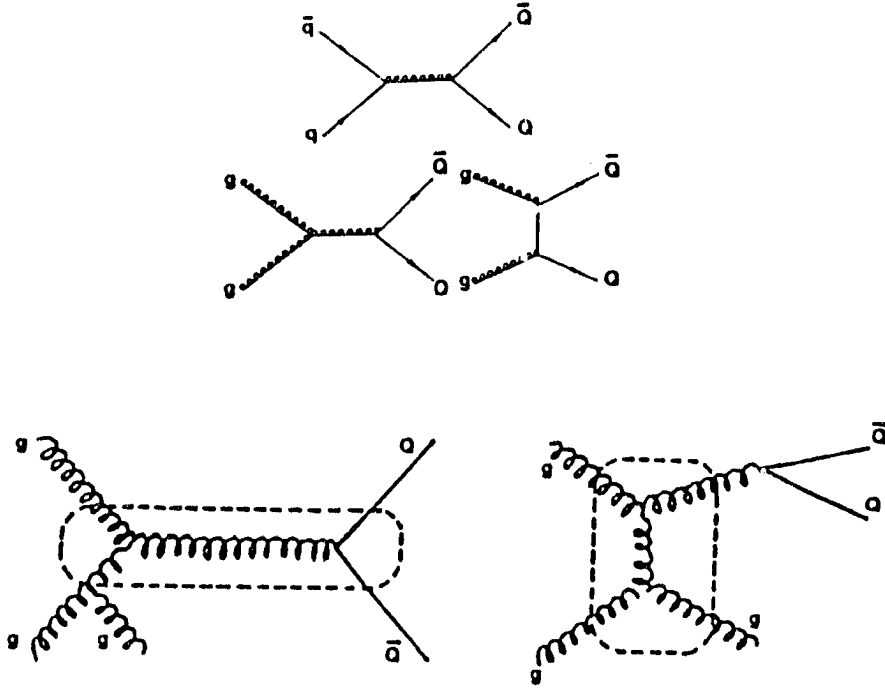


Figure 1.1: Feynmann diagrams for heavy flavor production

Process	$ A ^2$	$\theta = \pi/2$
$qq' \rightarrow qq'$	$\frac{4}{9} \frac{s^2 + \hat{u}^2}{\hat{t}^2}$	2.22
$qq \rightarrow qq$	$\frac{4}{9} \left(\frac{s^2 + \hat{u}^2}{\hat{t}^2} + \frac{s^2 + \hat{t}^2}{\hat{u}^2} \right) - \frac{8}{27} \frac{s^2}{\hat{u}\hat{t}}$	3.26
$q\bar{q} \rightarrow q'\bar{q}'$	$\frac{4}{9} \frac{\hat{t}^2 + \hat{u}^2}{s^2}$	0.22
$q\bar{q} \rightarrow q\bar{q}$	$\frac{4}{9} \left(\frac{s^2 + \hat{u}^2}{\hat{t}^2} + \frac{\hat{t}^2 + \hat{u}^2}{s^2} \right) - \frac{8}{27} \frac{\hat{u}^2}{s\hat{t}}$	2.59
$q\bar{q} \rightarrow gg$	$\frac{32}{27} \frac{\hat{t}^2 + \hat{u}^2}{\hat{t}\hat{u}} - \frac{8}{3} \frac{\hat{t}^2 + \hat{u}^2}{s^2}$	1.04
$gg \rightarrow q\bar{q}$	$\frac{1}{6} \frac{\hat{t}^2 + \hat{u}^2}{\hat{t}\hat{u}} - \frac{3}{8} \frac{\hat{t}^2 + \hat{u}^2}{s^2}$	0.15
$gq \rightarrow gq$	$-\frac{4}{9} \frac{s^2 + \hat{u}^2}{s\hat{u}} + \frac{s^2 + \hat{u}^2}{\hat{t}^2}$	6.11
$gg \rightarrow gg$	$\frac{9}{2} \left(3 - \frac{\hat{t}\hat{u}}{s^2} - \frac{s\hat{u}}{\hat{t}^2} - \frac{s\hat{t}}{\hat{u}^2} \right)$	30.4

Table 1.1: Two-to-two parton subprocesses. The third column gives the value of $|A|^2$ at 90° at 2 TeV. The gg process dominates.

	Mass (MeV)	muon B.R.	$c\tau$ (mm)	$\sigma(\sqrt{s} = 1800)$
D^\pm	1869.3	12%	0.28	260 μb
B^\pm	5271.2	11%	0.43	23 μb

Table 1.2: Properties of the charm and beauty mesons.

monte carlo programs are available to perform these calculations, of which we have used ISAJET [17].

In ISAJET, hard scattering processes are calculated using QCD matrix elements to lowest order in α_s . In the heavy flavor excitation mechanism, a heavy quark from the sea undergoes a hard scattering with a light quark or a gluon from the other incident hadron. ISAJET uses the heavy quark structure function of Eichten et al [18]. The heavy quark sea at large Q^2 is obtained by evolving initial parton distributions at $Q_0^2 = 5 \text{ GeV}^2/c^2$, without any intrinsic heavy quark component.

Hard partons participating in the large- Q^2 subprocesses are evolved using the basic QCD branching processes $q \rightarrow qg$, $g \rightarrow gg$, and $g \rightarrow q\bar{q}$. This is how the important higher-order diagrams are included in the monte carlo. Partons produced in the scattering process are then hadronized according to the independent fragmentation model of Field and Feynmann [8]. This model reproduces the measured properties of low-energy jets ($\sim 6 \text{ GeV}$) as well as many features of the jet fragmentation properties at Sp \bar{p} S collider energies [9].

Figure 1.2 shows ISAJET predictions for heavy flavor production as a function of \sqrt{s} , using only the lowest order diagrams in the calculation [13]. The beauty cross section at the Fermilab collider ($\sqrt{s} = 1800 \text{ GeV}$) is predicted to be 3.7 times greater than the cross section at the CERN Sp \bar{p} S ($\sqrt{s} = 630 \text{ GeV}$). Table 1.2 summarizes some properties of charm and beauty mesons.

1.2.3 Muon Rates

Momentum Acceptance

While the charm cross section is predicted to be an order of magnitude higher than the beauty cross section, and the branching ratios to muons are comparable (see table 1.2),

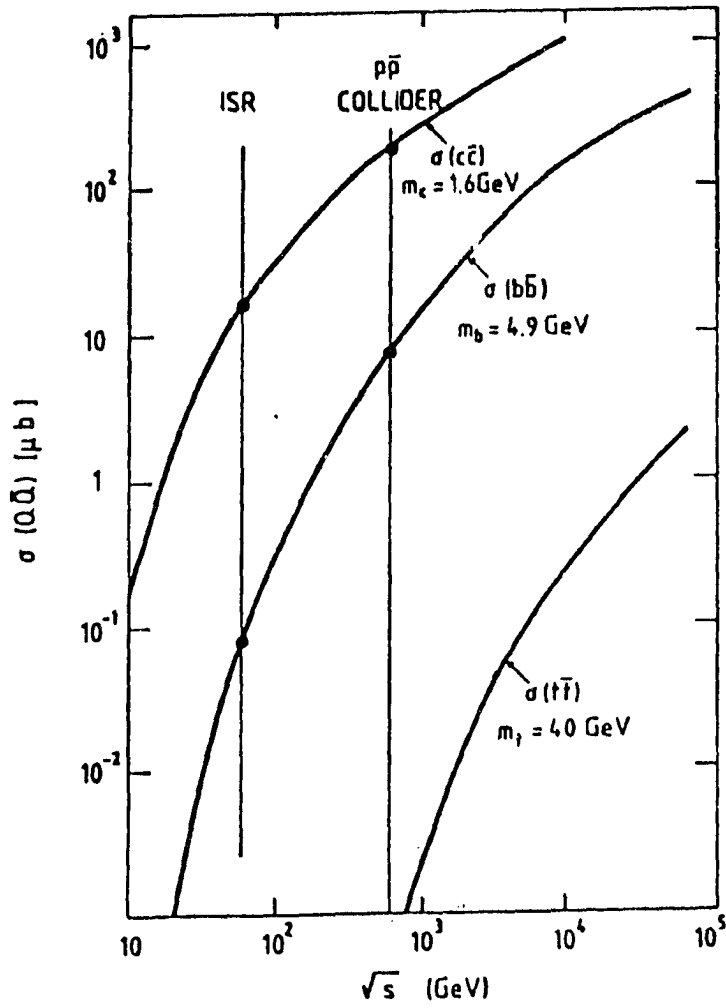


Figure 1.2: Heavy flavor cross sections using ISAJET lowest order calculations.

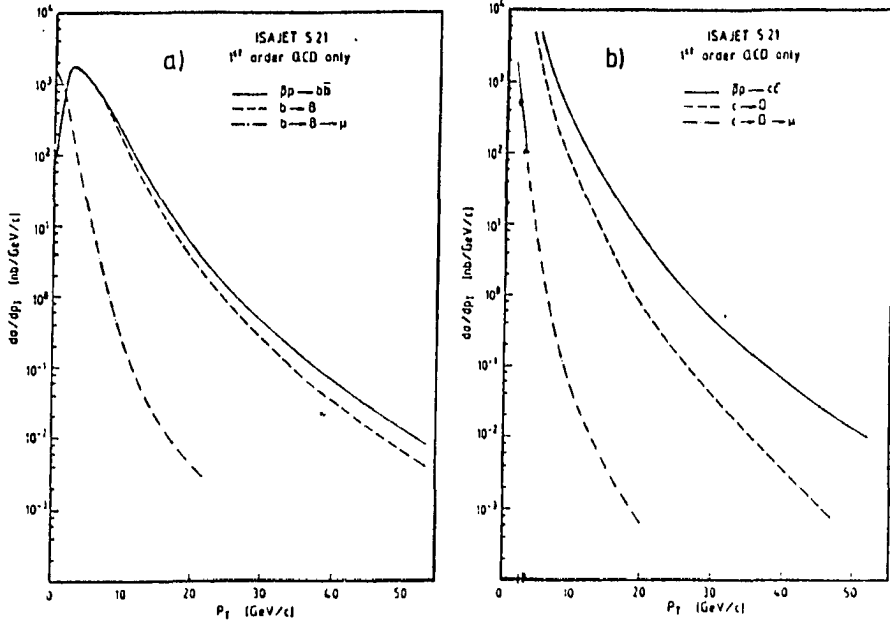


Figure 1.3: Predicted transverse momentum distributions of quarks, mesons, and muons in $b\bar{b}$ and $c\bar{c}$ production [13].

two thirds of the muons in the CDF central muon chambers are expected to come from beauty rather than charm, for $p_t^\mu > 3$ GeV/c. This is because the daughter muons from the more massive beauty meson have, on average, larger p_t than muons from D decay. Figure 1.3 shows the ISAJET transverse momentum distributions for muons from charm and beauty decay, calculated using the lowest order diagrams, in the pseudorapidity range $|\Delta\eta| < 2.0$ [13]. B production within this η range is η -independent [4]. The ISAJET study was made at the CERN collider energy of $\sqrt{s} = 630$ GeV, hence we scale to the Tevatron energy of $\sqrt{s} = 1800$ GeV according to figure 1.2. Integrating both the $b \rightarrow \mu$ and the $c \rightarrow \mu$ curves,

$$\sigma = \int_{p_1}^{p_2} \left(\frac{d\sigma}{dp_t} \right) dp_t \quad (1.2)$$

gives the relative abundance of beauty muons and charm muons. For the low statistics of the 1987 data, $p_2 = 15$ GeV/c is a reasonable upper limit since almost all of the muon candidates in the jet sample have lower p_t . Then figure 1.4 shows the fraction of muons from heavy flavor decay that come from charm, as a function of p_t .

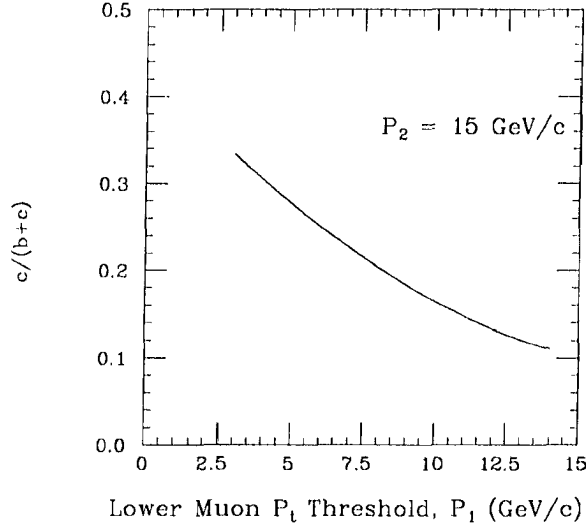


Figure 1.4: Fraction of heavy flavor muons coming from charm decay.

Figure 1.3 gives an upper limit on the number of muons from B decay. With $p_1 = 3$ GeV/c in equation (1.2), $\sigma = 290 \text{ nb}$ and the number of muons from beauty and charm decay is

$$N_\mu = \sigma_b \left(\int \mathcal{L} dt \right) f(\sqrt{s}) (1 + c/b) \epsilon_\eta \epsilon_\phi \quad (1.3)$$

where

$\int \mathcal{L} dt = 24.7 \text{ nb}^{-1}$ is the integrated luminosity for 1987;

$f(\sqrt{s}) = 3.7$ is the increased production cross section for CDF;

$\epsilon_\eta = \frac{0.7}{2.0}$ gives the pseudorapidity coverage of the central muon chambers;

$\epsilon_\phi = 0.76$ gives the azimuth coverage;

$(1 + c/b)$ accounts for the contribution from charm decay, taken from figure 1.4.

Note that $(1 + c/b) = [1 - (\frac{c}{b+c})]^{-1}$, where figure 1.4 shows that $\frac{c}{b+c} = .33$ for $P_1 = 3$ GeV/c. The result is

$$N_\mu = 290 \text{ nb} \times 24.7 \text{ nb}^{-1} \times 3.7 \times 1.5 \times 0.35 \times 0.76 = 10,575 \text{ muons.} \quad (1.4)$$

Trigger Acceptance

N_μ is the number of muons that were produced during our data run. They are of no use unless they were recorded on magnetic tape, which is the trigger's job. The jet trigger

tested the total transverse energy deposition in the calorimeters, $\sum E_t = \sum(E \sin \theta)$. B mesons produced in hard scatters between the partons of the protons and antiprotons decay into collimated sprays of hadrons, producing clusters of energy in the detector. But these jets tend to be fairly soft, and the probability is high that $b\bar{b}$ and especially $c\bar{c}$ pairs are produced without significant $\sum E_t$. These events will fail the trigger and reduce the observed N_μ .

A monte carlo study gives an idea of the magnitude of the inefficiency, and is summarized in table 1.3 [7]. In this study, ISAJET generated

$$p\bar{p} \rightarrow b\bar{b} \rightarrow \mu^+ \bar{c} \bar{\nu}$$

events, and the complete detector response was simulated. Included in the detector simulation is a detailed trigger simulation, giving the efficiencies of the different trigger $\sum E_t$ thresholds listed in the first column of table 1.3. When combined with the fraction of the total recorded integrated luminosity $\int \mathcal{L} dt$ in our data, the last column gives the fraction of the events that came from a given trigger setting. The overall trigger efficiency is about 4%, so that only

$$0.04 \times N_\mu \approx 425 \tag{1.5}$$

of the muons made it to tape. The systematic errors in this conclusion have not been studied.

Why not lower the $\sum E_t$ threshold? Theoretical calculations [6] suggest that at most 10% of the jet events will contain heavy flavors, and with a muon branching ratio of 10% the noise-to-signal is about 100:1 (assuming 100% trigger efficiency). The data acquisition capabilities of the detector would be swamped, and we would still reap a small harvest of $B \rightarrow \mu X$. The better solution is to trigger on the muons, but as stated above this was impractical for the 1987 run.

Minimum Ionization and Jet Overlap

Assuming that a semileptonic heavy flavor decay satisfied the jet trigger, the muon still has to pass the identification cuts (described in detail later in the thesis). Briefly, the largest source of fake muons is hadronic shower leakage in the calorimeter (interactive punchthrough). Interactive punchthrough is rejected by requiring that a muon candidate deposit energy in the calorimeter that is consistent with a minimum ionizing particle. But

ΣE_t threshold	Trigger Efficiency	Fraction of $\int \mathcal{L} dt$	Fraction of Data
20 GeV	0.114	0.016	0.047
30 GeV	0.058	0.48	0.718
40 GeV	0.022	0.23	0.131
50 GeV	0.015	0.27	0.104

Table 1.3: Efficiency of jet trigger for semileptonic B decay.

this cut also rejects muons that overlap with the hadron jet. This is a large rejection, greatly reducing the observed N_μ . The thesis conclusion shows that, between the trigger inefficiency and noise rejection, most (but not all!) of the muon signal is lost.

1.3 Signatures and Backgrounds

B^\pm and D^\pm decays are not the only sources of prompt muons in $p\bar{p}$ collisions, and neither is the number of observed muons the only means of distinguishing them. This section outlines signatures of heavy flavor decay, and backgrounds.

1.3.1 Momentum Transverse to the Jet Axis, p_t^{rel}

Since the B meson is more massive than pions or kaons, its decay muons have more momentum in the meson rest frame. When boosted to the lab frame, this appears as a larger p_t^{rel} , the momentum transverse to the jet axis. Figure 1.5 shows an approximation to p_t^{rel} . A Lorentz-invariant expression is

$$p_t^{rel} = p \sqrt{\tanh^2(\Delta\eta) + \sin^2(\Delta\phi)} \quad (1.6)$$

where p is the total momentum of the track, and

$\Delta\eta = \eta_{jet} - \eta_{track}$ is the difference in pseudorapidities of the jet and the track, and

$\Delta\phi = \phi_{jet} - \phi_{track}$ is the difference in azimuth angles of the jet and the track.

UA1 used p_t^{rel} to separate charm from beauty in their heavy flavor studies, their result is shown in figure 1.6 ³.

³UA1 is CDF's cousin detector at the CERN $p\bar{p}$ collider, where high energy $p\bar{p}$ collisions were pioneered.

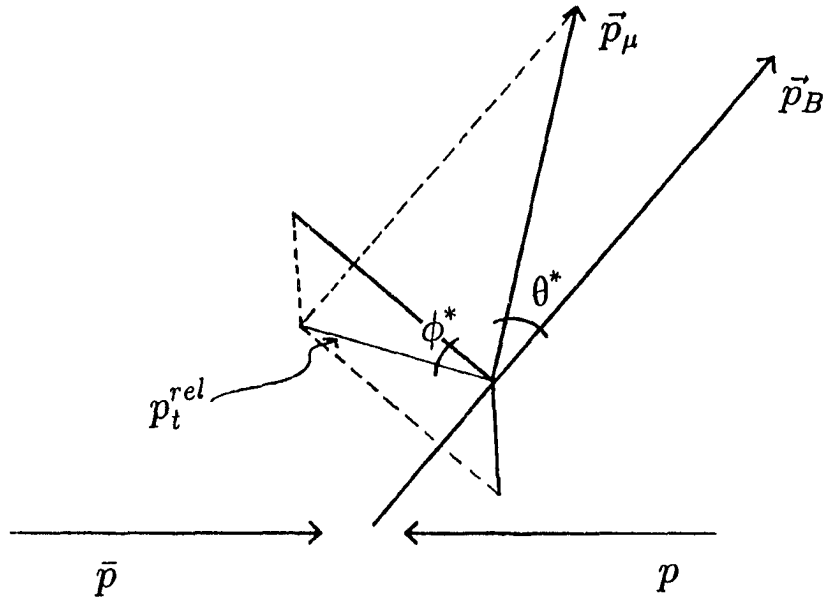


Figure 1.5: The decay $B \rightarrow \mu X$, showing the momentum component p_t^{rel} transverse to the jet axis, and the variables for the simplified calculation.

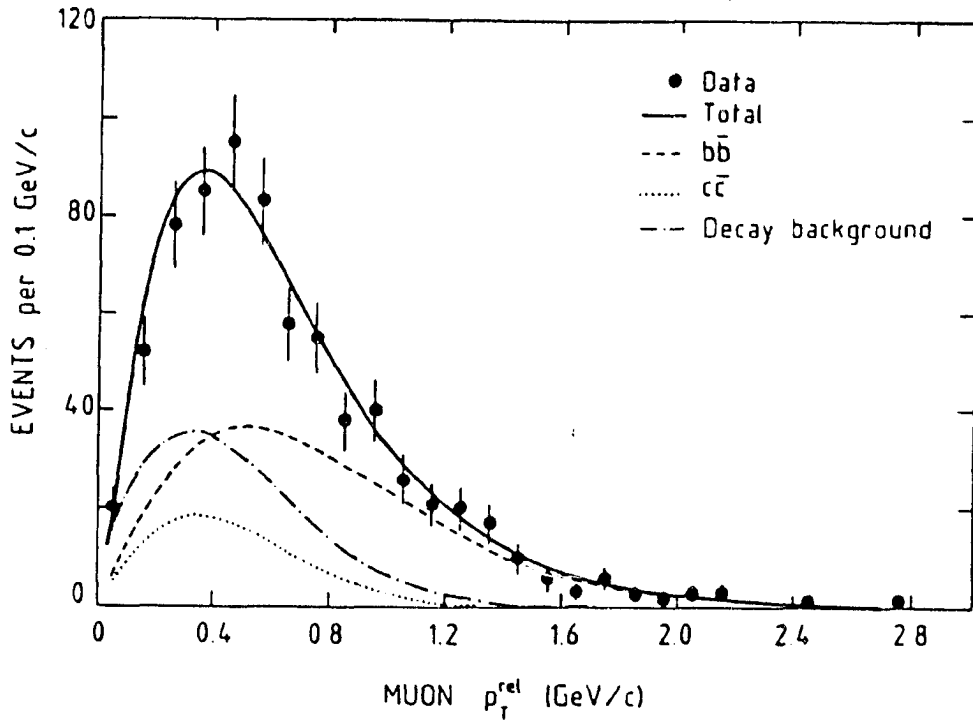


Figure 1.6: Muon p_t^{rel} measured by UA1. Solid curves come from Isajet. p_t^{rel} for muons from B decay is larger than for charm decay.

A simple calculation clarifies the kinematics of the beauty signature, and gives the same qualitative results as the full monte carlo. Quantitative conclusions require ISAJET and detector simulation, but the following argument gives conceptual insight.

Assume that $p\bar{p} \rightarrow b\bar{b}$ produces back-to-back B and \bar{B} mesons leaving the collision vertex. One of the mesons then decays directly into a muon and a jet,

$$B^\pm \rightarrow \mu^\pm \nu \text{ jet}$$

while the other meson hadronizes into a jet. This gives back-to-back jets, accompanied by a muon. The muon momentum is determined by the momentum and direction of the parent B . Figure 1.7 shows the calculated distribution of the transverse momenta of the B 's relative to the beam axis [4]. The exponential distribution

$$N(p_t^B) = N_0 e^{-p_t^B/3.6}, \quad p_t^B \text{ in GeV}$$

approximates the curve in the range $2 < p_t^B < 20$ GeV/c. The decay into a muon in the B rest-frame is isotropic, so the azimuth angle distribution of the muons about the B axis is flat, while θ^* of the muon relative to the B axis comes from assuming a flat distribution in $\cos \theta^*$, so that all elements of solid angle $d\Omega = d\phi^* d(\cos \theta^*)$ are uniformly populated. (The starred (*) variables are in the B rest frame.) Figure 1.5 illustrates these variables.

The muon momentum in the B frame has been measured by the ARGUS collaboration (figure 1.8) [16]. Since $\frac{dN}{d\eta_B}$ is flat in the region covered by the muon chambers ($-0.65 < \eta < 0.65$) [4], all the information necessary to simulate the decay $B \rightarrow \mu X$ in a short monte carlo program and to boost the muon from the B frame to the lab frame is at hand.

Figure 1.9 shows the result. (We assume that the initial B direction defines the jet axis.) The peak is at higher p_t^{rel} than in figure 1.6. The reason is that the simple calculation completely ignores the process

$$B^\pm \rightarrow D^{*\pm} X, \quad D^{*\pm} \rightarrow \mu X \tag{1.7}$$

which contributes muons with much less 'kick' relative to the B axis (lower p_t^{rel}). The simple calculation also yields

$$\frac{dN_\mu}{dp_t} = N_0 e^{-p_t/p_0}$$

with $p_0 \simeq 1.7$ as compared to $p_0 \simeq 1.2$ from figure 1.3. Again, the relative stiffness of the simple calculation comes from the omission of the processes (1.7), but the rough agreement affords insight into the dynamics.

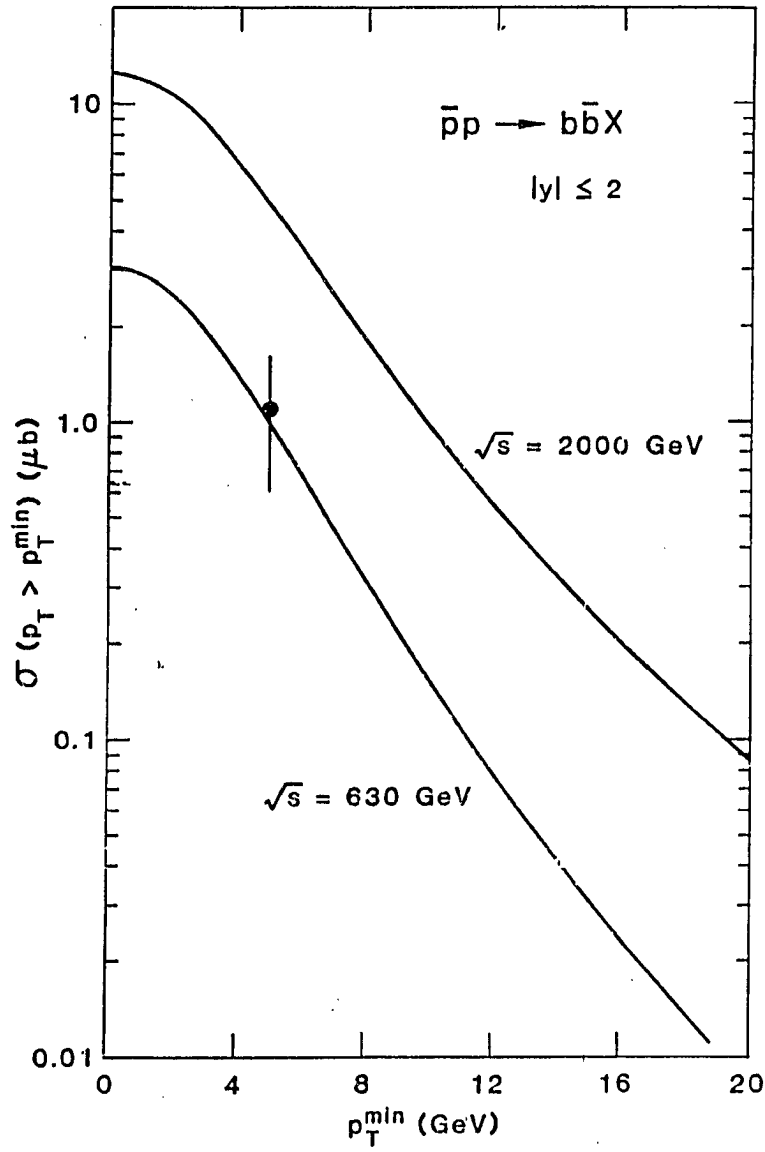


Figure 1.7: QCD calculation of the B meson momentum transverse to the beam .

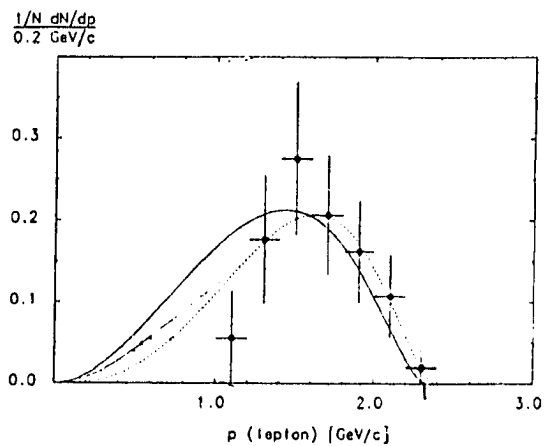


Figure 1.8: Muon momentum spectrum from the decay $B \rightarrow \mu X$, in the B rest-frame, as measured in e^+e^- collisions by the Argus collaboration.

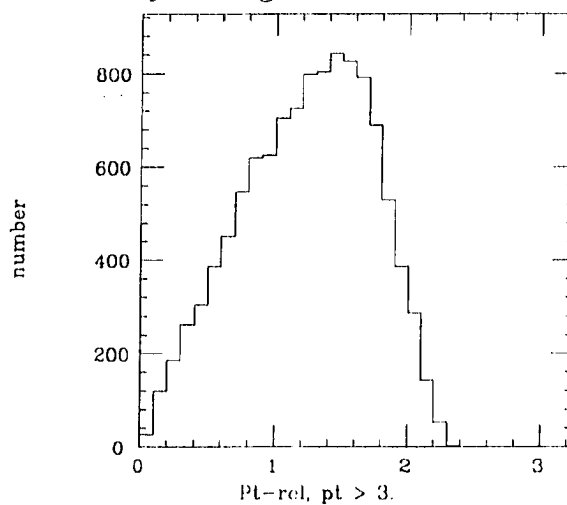


Figure 1.9: Muon p_t^{rel} spectrum for muons from $B \rightarrow \mu X$, calculated using the simplified model.

1.3.2 Muons from Other Processes

All the fundamental interactions contribute to muon production in $p\bar{p}$ collisions:

- Weak interactions produce Z^0 and W^\pm particles, which decay directly into muons. A search for $Z^0 \rightarrow \mu^+ \mu^-$ and $W \rightarrow \mu \nu$ in our data sample has yielded 7 W 's and 1 Z^0 [2]. These muons are unaccompanied by jets and will not be considered.
- The electromagnetic force produces $\mu^+ \mu^-$ pairs directly by the Drell-Yan mechanism. The rate is lower than for single muons produced by heavy flavor decay.
- Strong interactions (QCD) produce J/Ψ , Υ , D , and B particles, which all decay into muons with branching ratios around 10%.

The signature for J/Ψ 's and Υ 's is unambiguous: the distribution of invariant masses for isolated unlike-sign dimuons shows sharp peaks above the Drell-Yan continuum. Unfortunately, the trigger efficiency for dimuons is the single muon efficiency squared, and was very low. An appendix shows the few dimuon events recorded in 1987. In a study of muons from B and D decay, the single muons from Drell-Yan and J/Ψ , Υ decays constitute background. (The second muon having been lost through gaps in the detector coverage.) The issue is how to distinguish muons from B decay from muons produced by other processes. Two more handles are available.

Muon Isolation

A muon from B decay tends to be accompanied by hadron jets, whereas Drell-Yan and J/Ψ or Υ events tend to have low $\sum E_t$. Hence cuts on calorimeter clusters or $\sum E_t$ enhance the B content of a data sample. But in both cases the picture is clouded by large fluctuations in the hadron energy: the jets can be soft or diffuse so that B events fail cuts, and energy from the underlying event of Drell-Yan and J/Ψ or Υ events can cluster together to mimic a jet, contaminating a B sample. In the UA1 detector the hadronic noise from the underlying event is about 3.6 GeV per unit of rapidity, with large fluctuations [13, p. 77]. Poor energy resolution in the calorimeter compounds the problem. ISAJET and the CDF detector simulation make the muon isolation useful in identifying beauty.

Missing E_t

The semileptonic decay of the heavy quark produces a neutrino which appears as a transverse energy imbalance. On average, however, the magnitude of the neutrino transverse momentum is comparable to the resolution of the missing transverse energy measurement,

$$\delta E_\nu = 0.9\sqrt{\sum E_t}$$

so that neutrino measurement is not useful as an indicator of charm or beauty in our data.

On the other hand, as stated above, the largest source of fake muons is shower leakage in the calorimeter. But cuts to reject leakage also reject muons imbedded in the jet. Hence a handle that distinguishes the two types of events is powerful. Preliminary studies indicate that missing E_t is correlated with muon quality.

1.3.3 Fake Muons

A thin calorimeter and a large central tracking volume combine to produce a large background to the prompt muon signal. Prompt means muons coming directly from the $p\bar{p}$ collision. Sources of fake muons include

- non-interactive hadron punchthrough;
- meson decay-in-flight;
- interactive punchthrough (shower leakage);
- cosmic rays;
- central track/central muon mismatch (misassociation);
- gaps in the detector.

The rate for each process is calculated in chapter 3.

1.4 Outline of the Thesis

Chapter 1 outlines the goal of the thesis, to identify muons from heavy flavor decay in jet events. The rest of the thesis describes the path followed to reach the goal. Chapter

2 describes the experimental apparatus used. Chapter 3 examines the muon signature and the backgrounds to the muon signal. Chapter 4 contains the data analysis and the background subtraction, showing the muon signal. In chapter 5 we summarize the results of the study.

Chapter 2

Apparatus

Fermi National Accelerator Laboratory is home to the world's highest energy proton-antiproton collider, a two-kilometer diameter superconducting synchrocyclotron called the Tevatron. The Collider Detector Facility (CDF) is the multipurpose particle detector that measures the collision products. The High Energy Physics Group at the University of Illinois built the muon tracking chambers covering the region at large angles from the beam, and has used the chambers, as well as every other part of CDF, to study the physics of this new energy domain. This chapter describes the aspects of the Tevatron and of CDF that are relevant to the $B \rightarrow \mu X$ study.

2.1 The Tevatron

The accelerator design energy is 1000 GeV per beam (1000 GeV = 1 TeV, whence the name), and the colliding beams currently operate at $\sqrt{s} = 1.8$ TeV. The Tevatron shares the tunnel with the original Fermilab accelerator, called the Main Ring, made of conventional magnets and with a maximum energy of 400 GeV per beam. The Main Ring serves as a booster for the Tevatron, and provides primary protons to the antiproton source. The first collider test in October, 1985 proved that the basic design of the accelerator and detector were sound. The data for this thesis came from the first data run, which began in late January and ended in mid-May of 1987.

2.1.1 Luminosity

A single event tells almost nothing about a physical process. Measurements require statistical distributions, and more events allows better measurements. Events occur at a

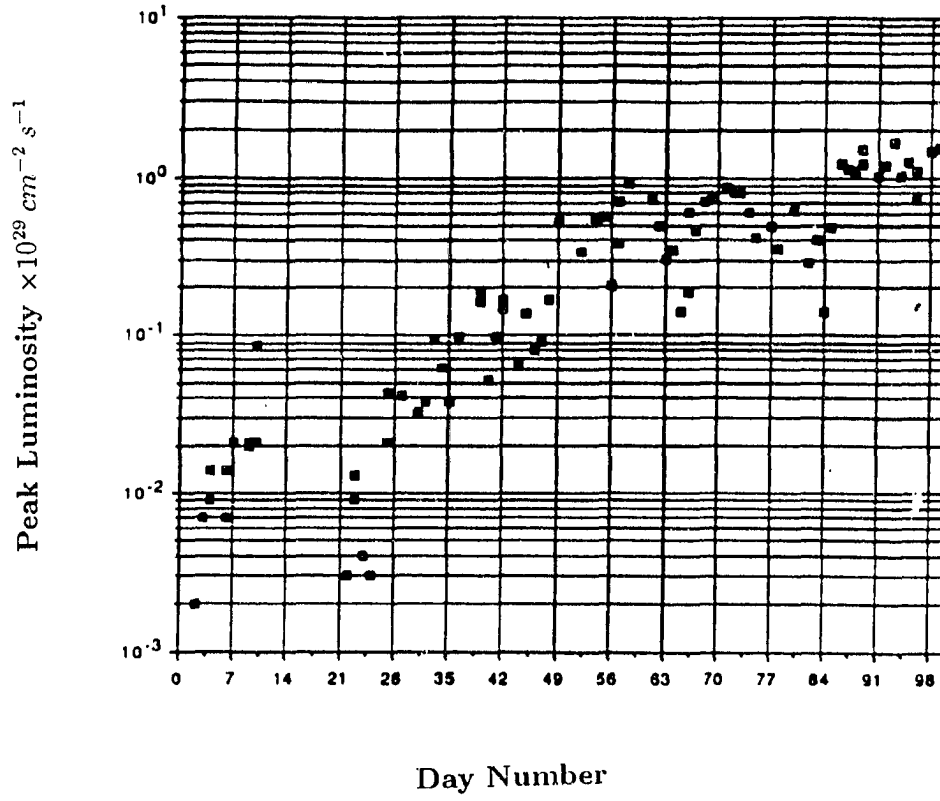


Figure 2.1: Peak luminosity for each $p\bar{p}$ store, versus day number into the run. Day 1 is February 1, 1987. The peak value exceeded the goal for this run of $\mathcal{L}_0 = 10^{29} \text{ cm}^{-2} \text{ s}^{-1}$.

Process	Rate at $\mathcal{L} = 10^{29} \text{ cm}^{-2} \text{ s}^{-1}$
Bunch crossings	147 kHz
$p\bar{p}$ inelastic collisions	7 kHz
$B \rightarrow \mu X, 3 \leq p_t^\mu \leq 15 \text{ GeV}/c$	0.124 Hz
Brass muon trigger, $p_t > 5 \text{ GeV}/c$	9 Hz
Golden muon trigger, $p_t > 5 \text{ GeV}/c$	0.2 Hz
$\Sigma E_t \geq 30 \text{ GeV}$ trigger	0.6 Hz
Events to tape	$\sim 1 \text{ Hz}$

Table 2.1: List of rates.

rate

$$R = \sigma \mathcal{L} \quad (2.1)$$

where σ is the cross section for a given process, and the luminosity \mathcal{L} reflects the intensity of the colliding beams. For example, the inelastic cross section for protons on antiprotons is

$$\sigma_{p\bar{p}}(\sqrt{s} = 1.8 \text{ TeV}) \approx 70 \text{ mb}.$$

The geometric acceptance of the CDF trigger reduces this to 44 mb . Figure 2.1 shows luminosities near $\mathcal{L} = 10^{29} \text{ cm}^{-2} \text{ s}^{-1} = 0.1 \mu\text{b}^{-1} \text{ s}^{-1}$, so the rate for $p\bar{p}$ collisions is 4400 hz^1 . On the other hand, equation (1.4) showed that, neglecting detector acceptance,

$$\sigma(B \rightarrow \mu X; 3 \leq p_t^\mu \leq 15) = 1.24 \mu\text{b}$$

so only 1 in 56,000 $p\bar{p}$ collisions yields an event for this thesis. Table 2.1 lists some rates.

The total number of events accumulated is more important than the instantaneous rate, and is

$$N = \int R dt = \sigma \int \mathcal{L} dt$$

where $\int \mathcal{L} dt$ is the integrated luminosity. To understand $\int \mathcal{L} dt$ requires a brief description of accelerator operations.

¹ 1 barn = 10^{-24} cm^2 .

2.1.2 Colliding Beams

A pulse of $\sim 10^{11}$ protons passes through a sequence of boosters, is injected into the Main Ring, accelerated to 120 GeV, and extracted onto at a fixed target, generating millions of antiprotons. The \bar{p} 's are collected in a storage ring near the Tevatron. The sequence is repeated and when enough \bar{p} 's have accumulated ($\sim 10^{10}$), three bunches of protons are injected into the Main Ring and left circulating. Three bunches of \bar{p} 's are then extracted from the accumulator and injected into the Main Ring in the opposite direction. All six bunches are accelerated to 120 GeV, transferred into the Tevatron, accelerated to 900 GeV, and then stored. So a $p\bar{p}$ store consists of counter-circulating bunches of protons and antiprotons coasting at high energy.

The bunches pass through each other at six points around the ring. If the bunches are dense, $p\bar{p}$ collisions occur at a useful rate. One of the crossing regions, called B0, accommodates the CDF experiment with a large experimental hall and, importantly, special focussing quadrupole magnets at either side of the crossing region that squeeze the bunches in the transverse direction, increasing the density. The beam profile is gaussian with size $\sigma^2 = \sigma_x^2 + \sigma_y^2$, where σ_x, σ_y are the rms beam widths in the horizontal and vertical directions. The luminosity is

$$\mathcal{L} = \frac{N_p N_{\bar{p}} C}{4\pi\sigma^2} \quad (2.2)$$

where $N_p, N_{\bar{p}}$ are the numbers of protons and antiprotons per bunch, and C is the bunch crossing rate (see table 2.1).

As the colliding beams coast, N_p and $N_{\bar{p}}$ decrease due to collisions with each other and with the accelerator, and also σ^2 increases (emittance growth). The luminosity degrades with a lifetime τ ,

$$\mathcal{L} = \mathcal{L}_0 e^{-t/\tau}. \quad (2.3)$$

Squeezing the beam increases \mathcal{L}_0 but it also decreases τ . Squeezing the particle bunches is like squeezing putty: compress it in one spot, and it will stick out somewhere else. Hence a small beam at B0 implies a fat beam elsewhere, beam-accelerator scraping increases, and τ degrades. More precisely, the emittance ϵ is a characteristic constant of the accelerator, and

$$\epsilon = 6\pi \frac{\sigma^2}{\beta(s)} \quad (2.4)$$

<i>Parameter</i>		<i>1987 run</i>	<i>Design Goal</i>	<i>Units</i>
Luminosity lifetime	τ	6-12	~ 20	hours
Initial luminosity	\mathcal{L}_0	10^{26} - 10^{29}	10^{30}	$\text{cm}^{-2}\text{s}^{-1}$
No. of protons per bunch	N_p	5×10^{10}	10^{11}	
No. of antiprotons per bunch	$N_{\bar{p}}$	10^9	10^{10}	
Transverse beam size	σ	70	70	μM
Emittance (at 900 GeV)	ϵ	0.1π	0.025π	mm-mR
\bar{p} stacking rate		5×10^9	5×10^{10}	\bar{p} 's per hour

Table 2.2: Accelerator parameters.

where the β -function $\beta(s)$ varies with the position s around the ring. Squeezing the beam means reducing β at B0, so σ^2 decreases to maintain constant ϵ and \mathcal{L} increases. Equation (2.4) is important in measuring the actual value of \mathcal{L} . Table 2.2 lists typical values for some accelerator parameters.

Luminosity Measurement

Equation (2.1) shows that a cross section measurement is limited by the accuracy of \mathcal{L} . CDF measures the luminosity using the beam-beam counters (BBC). The BBC provide the simplest $p\bar{p}$ collision trigger, the minimum bias trigger. (All triggers used during the run required a coincidence with the minimum bias trigger.) They are concentric rings of scintillator between the central and the forward/backward detectors, labeled ‘trigger counters’ in figure 2.3. Monte carlo simulation of minimum bias events gives the acceptance of the BBC for different processes. The acceptance is $\sigma_{\text{min bias}} = 44$ mb if one requires at least one hit in the East and one hit in the West. Then the luminosity is

$$\mathcal{L} = \frac{R}{\sigma_{\text{min bias}}}$$

where R is the measured rate of $p\bar{p}$ collisions. The accuracy is limited by how well the $p\bar{p}$ cross sections are known, about 15%.

Main Ring Background

Integrated luminosity depends on

- the initial luminosity, \mathcal{L}_0 , and the luminosity lifetime, τ (equation 2.3);
- the turnaround time for a new store.

The accelerator crew varied the β squeeze to tune \mathcal{L}_0 and τ for optimal $\int \mathcal{L} dt$, but the second item has a serious consequence for muon detection. A typical store lasts a matter of hours before ending, whether by accident or because the luminosity has degraded beyond use. A new store begins only if enough \bar{p} 's are in the Accumulator, and since the accumulation rate was low (table 2.2), antiproton production had to continue during the store. Now, the Tevatron goes through the center of CDF (see figure 2.2) but the Main Ring passes above the detector, inside the collision hall. As described, \bar{p} production means accelerating protons in the Main Ring, and 50% of the protons are lost during acceleration. The losses create large radiation pulses in the detector, and saturate the central muon chambers near the Main Ring beam pipe. This point will be discussed again after the description of the chambers.

2.2 The Collider Detector Facility

2.2.1 Overview of the Detector

The Collider Detector Facility (CDF) is an enormous assembly of 15 subdetector systems, designed to measure the properties of all the particles produced in $p\bar{p}$ collisions at a center-of-mass energy of 2 TeV. Following a track from the collision vertex outward, the detector consists of successive layers of particle tracking, calorimetry, and muon detection. Magnetic fields in the tracking chambers provide momentum analysis for charged particles. To cover almost the full 4π steradians solid angle around the interaction point, CDF is built in three major pieces: the forward and backward sections cover the region from 2° to 10° from the beam, while the central and plug detectors measure particles at larger angles from the beam. Figure 2.2 is an isometric view of the detector and figure 2.3 shows a cross-section of CDF.

2.2.2 Central Tracking

The heart of the central detector is the CTC, or Central Tracking Chamber, mounted inside the world's largest operating superconducting solenoid. The solenoid provides a

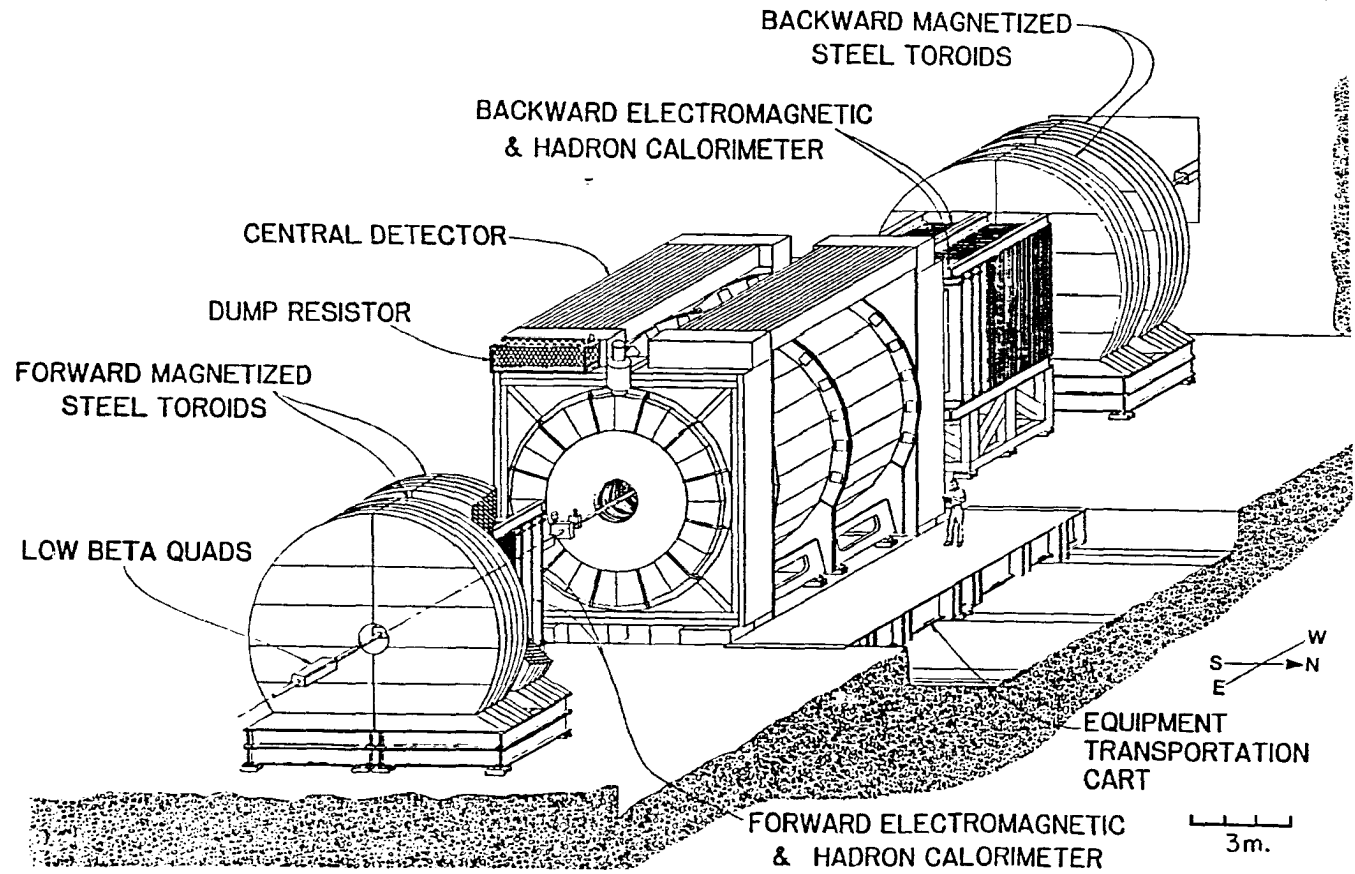


Figure 2.2: Isometric view of the CDF detector.

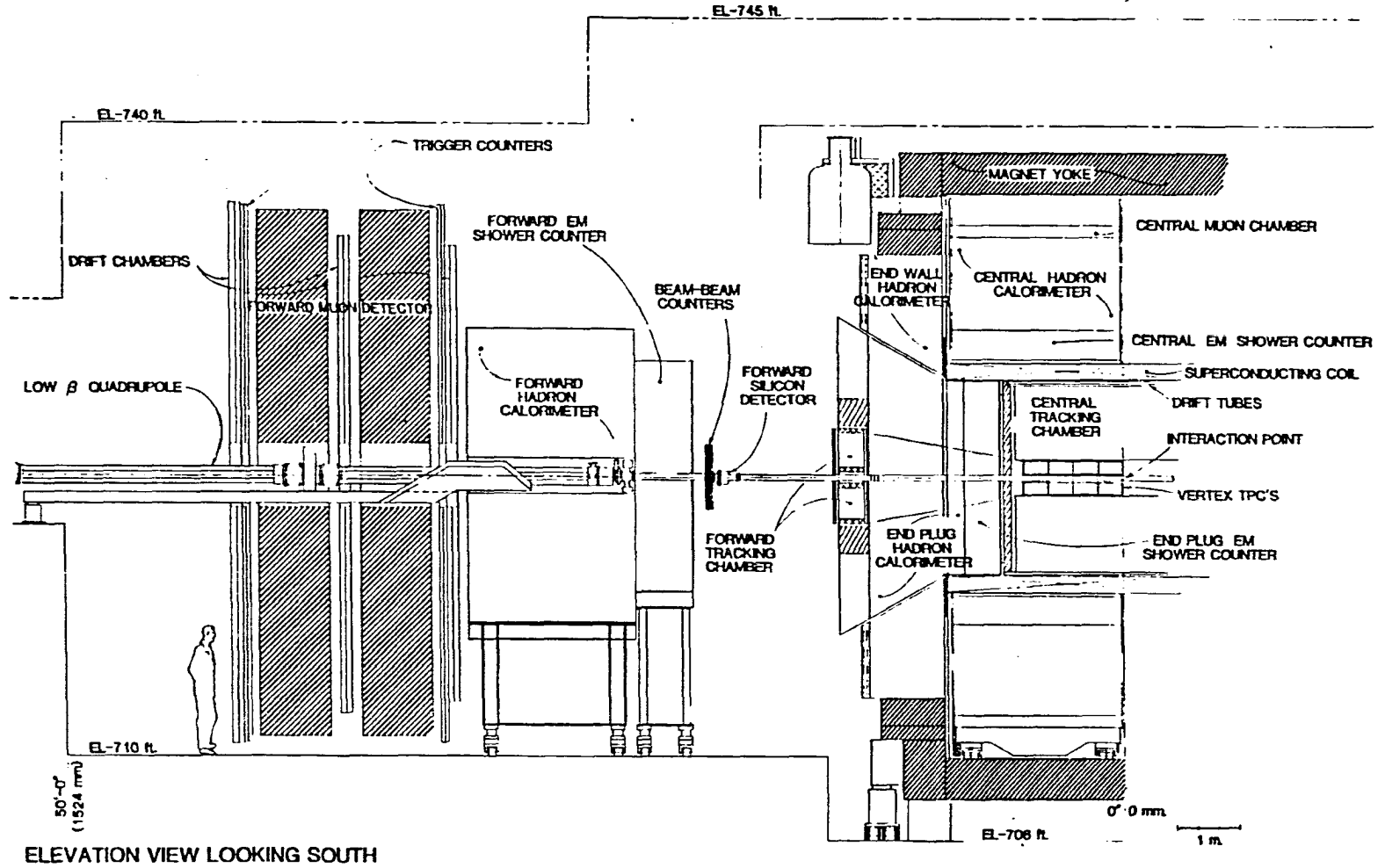


Figure 2.3: Elevation view of the CDF detector.

uniform field of 1.5 Tesla parallel to the beam axis, over a volume 5 meters long and 3 meters in diameter. The CTC, with inner radius of 30 cm and outer radius of 140 cm, has five axial superlayers of sense wires consisting of 12 layers each, and four 3° stereo superlayers of 6 layers each for measurement along the z-direction (appendix A describes the coordinate systems). Cells of wires are tilted $\sim 45^\circ$ relative to the radial direction to compensate for the Lorentz angle of the electrons drifting in the magnetic field, so that the actual drift is perpendicular to the radial direction, i.e., perpendicular to the trajectory of high momentum particles.

The sense wire spacing is $\sim 7\text{mm}$ in the radial direction, and the maximum drift distance is $\sim 35\text{mm}$. There are 6156 sense wires, read by multihit FastBus TDCs. The outermost superlayer covers the region $40^\circ \leq \theta \leq 140^\circ$ while the innermost superlayer covers $14^\circ \leq \theta \leq 166^\circ$. The measured resolution for single hits within a superlayer was $300\mu\text{m}$, dominated mainly by understanding of the drift constants. Resolution of $200\mu\text{m}$ is believed attainable. Momentum resolution (r.m.s.) for tracks that pass through all the superlayers (the tracks of interest in our central muon studies) is

$$\frac{\delta p_t}{p_t} \leq (0.002p_t + 0.003) \quad p_t \text{ in GeV}/c. \quad (2.5)$$

Figure 2.4 shows CTC data in the r - ϕ plane for a typical event, from the CDF display graphics. The high resolution of the CTC is apparent in the ability to reconstruct tracks even in the middle of high multiplicity jets.

Between the CTC and the beampipe is the VTPC, or Vertex Time Projection Chamber, providing accurate tracking in the r - z plane. Figure 2.5 shows VTPC data from the same event as figure 2.4, only in the r - z plane. While displays of VTPC data provide fast feedback on the operation of the accelerator and of the detector (the first $p\bar{p}$ collisions at Fermilab were identified by the VTPC) the main use of the VTPC in this analysis has been to locate the collision vertex.

Just outside the CTC, but still inside the solenoid, are the Central Drift Tubes (CDT). The CDT provides a more accurate z -measurement than the stereo layers of the CTC, useful for pattern recognition. CDT data is visible in figure 2.4. The CDT was designed, built, and operated by a team from the University of Illinois, led by Professor Steven Errede.

Figure 2.4: Graphics display of an event in the Central Tracking Chamber.
($r\phi$ -view of the detector, beam normal to page.) The VTPC is at the center, with the Central Drift Tubes at the outer edge of the CTC. Energy in the central wedges, integrated over η , shown outside of the CDT. Tracks in the muon chambers appear as x's outside the calorimetry.

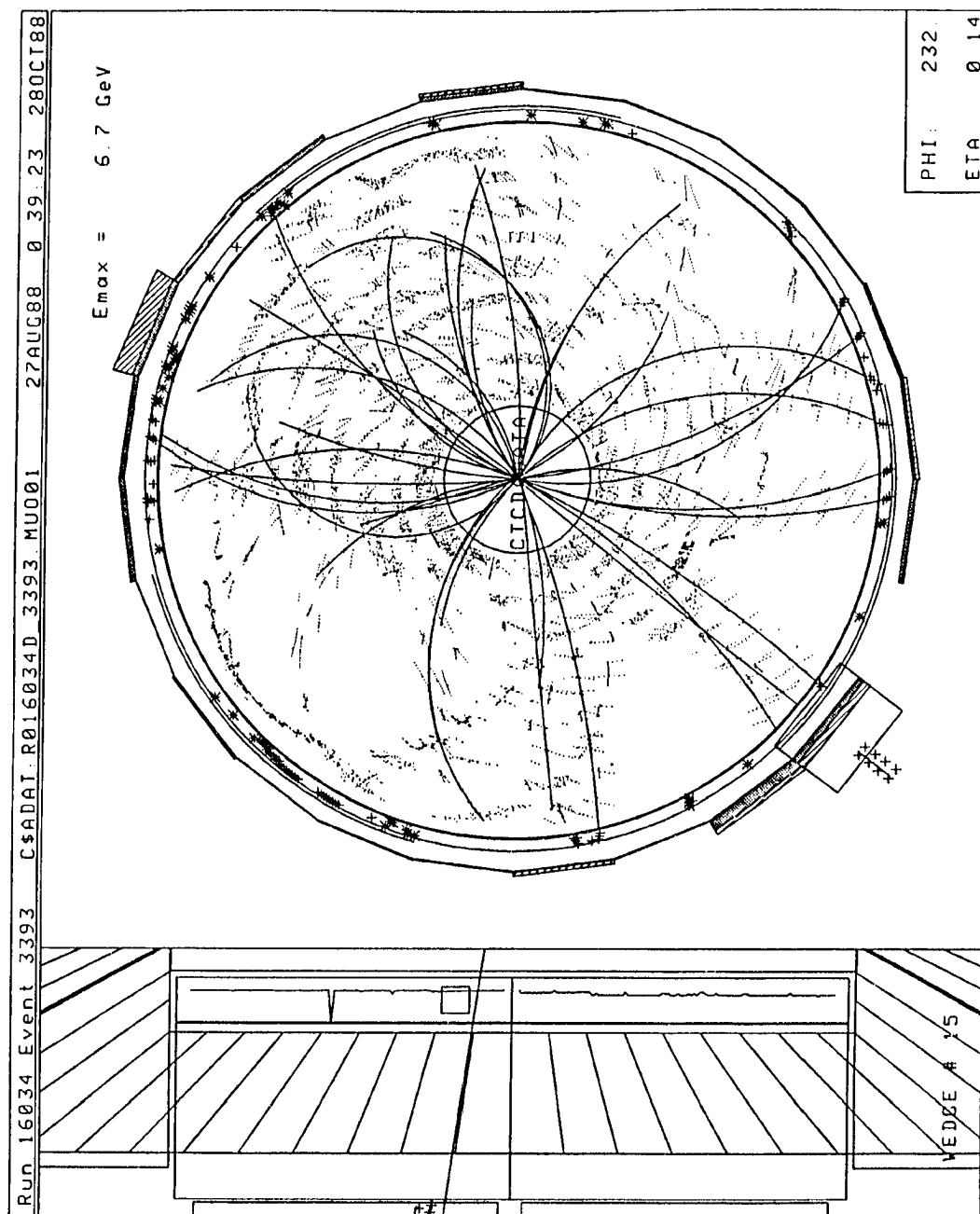
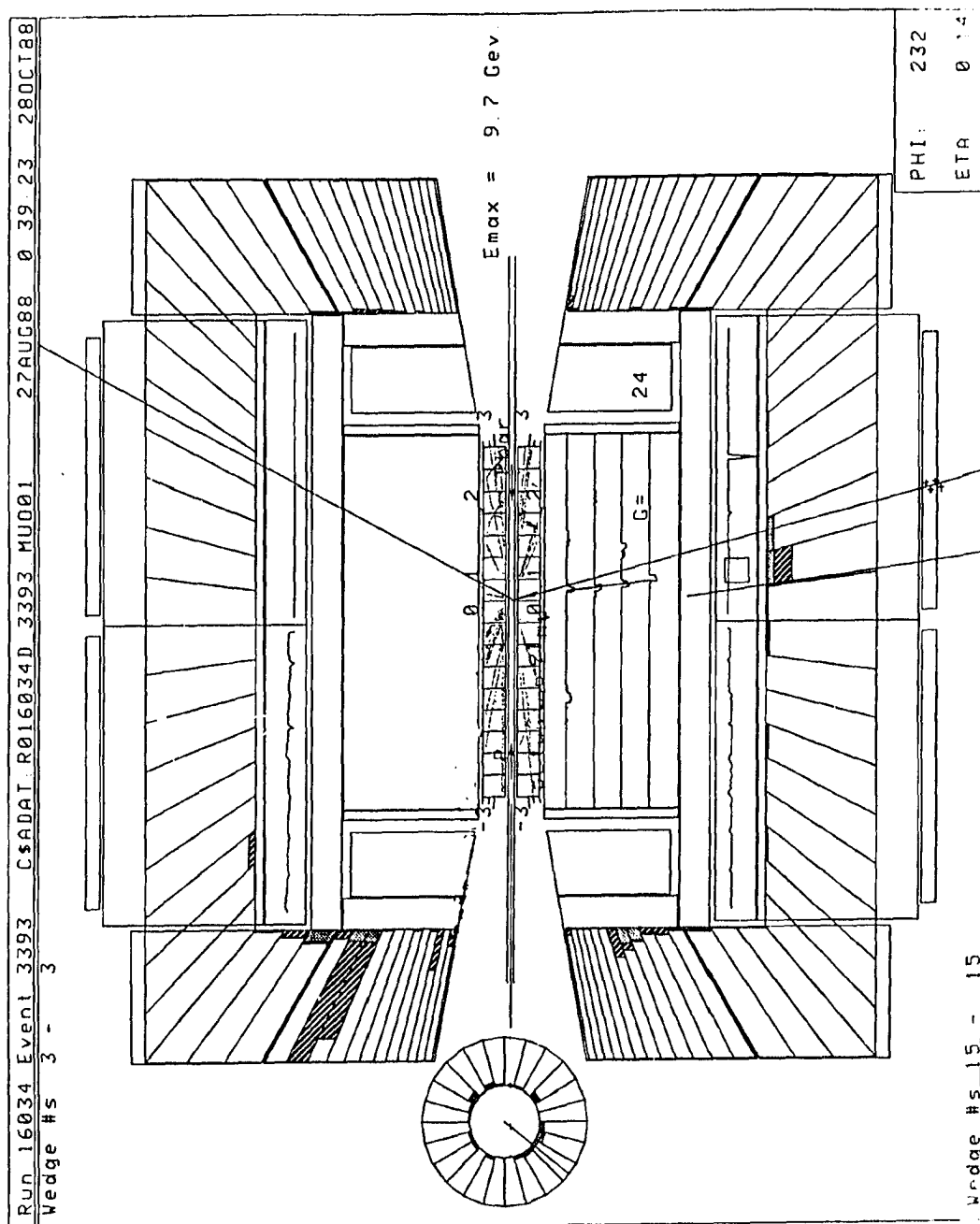


Figure 2.5: Graphics rz -view of an event, beam in the plane of the page. Tracks in the VTPC, stereo CTC hits, calorimeter response and muon hits are all shown.



2.2.3 Calorimetry

Outside of the tracking chambers sit the electromagnetic and hadronic calorimeters. The strengths of the CDF calorimetry are good granularity, the projective tower structure, and good energy resolution. The specifics are shown in table 2.3. The calorimeters cover ± 4 units in pseudorapidity η and the full 2π azimuth. The hadron calorimeters alternate layers of steel with the sampling layers, while the shower counters use lead. In the central region ($|\eta| \leq 1.1$) the sampling medium is scintillator, chosen for its good energy resolution, while outside of this region the sampling medium is gas proportional tubes, chosen for their economy, resistance to radiation damage, and adaptable geometry. The calorimeter tower shape allows unambiguous spatial localization of the energy deposition within the calorimeter. Each tower subtends a solid angle of roughly constant $\Delta\eta$ and $\Delta\phi$ when viewed from the nominal $p\bar{p}$ collision point. In the central region a single tower has

$$\Delta R = \sqrt{(\Delta\phi)^2 + (\Delta\eta)^2} \simeq \sqrt{(.25)^2 + (.1)^2} \simeq 0.27.$$

The parameter ΔR is useful in describing jets in subsequent chapters.

Gas Calorimetry

This thesis concerns jets and muons in the central rapidity region of CDF. Consequently the forward and backward gas calorimetry is of secondary interest. Also, during the first run of CDF there were teething problems for the gas calorimetry. The problems come from the late construction start of the forward detectors relative to the central detector, and from the fact that gas calorimetry is intrinsically more difficult to operate: gas calorimeter gains depend on the gas pressure and temperature, which vary with the weather, and the tubes must be calibrated quasi-continuously, using elaborate apparatus that scintillator groups never have to contend with. Furthermore, wire chambers are more susceptible to electronic noise. During the run the forward calorimeter groups discovered that stray neutrons from the accelerator create large spurious pulses, contaminating the data and raising trigger rates. These problems have been corrected since the end of the 1987 run, but the $B \rightarrow \mu jet$ analysis did not use the gas calorimeters.

EM Shower Counter				
	<i>Central</i>	<i>End Plug</i>	<i>Forward</i>	
Coverage	$37^\circ < \theta < 90^\circ$	$10^\circ < \theta < 37^\circ$	$2^\circ < \theta < 10^\circ$	
Tower size	$0.087 < \Delta\eta < 0.13$ $\Delta\phi = 15^\circ$	$0.05 < \Delta\eta < 0.1$ $\Delta\phi = 5^\circ$	$\Delta\eta \sim 0.1$ $\Delta\phi = 5^\circ$	
Sampling	Scintillator	Gas	Gas	
Radiation lengths	26	34	31	
$\Delta E/E$	$14\%/\sqrt{E}$	$24\%/\sqrt{E}$	$27\%/\sqrt{E}$	
Spatial resolution	2-4 mm	1-2 mm	1.5-3 mm	
Absorption lengths	$\sim 1\lambda_{abs}$			
Radiation lengths	$19X_0$			

Hadron Calorimeter				
	<i>Central</i>	<i>End Wall</i>	<i>End Plug</i>	<i>Forward</i>
Coverage	$45^\circ < \theta < 90^\circ$	$30^\circ < \theta < 45^\circ$	$10^\circ < \theta < 30^\circ$	$2^\circ < \theta < 10^\circ$
Tower size	$0.1 < \Delta\eta < 0.15$ $\Delta\phi = 15^\circ$	$0.08 < \Delta\eta < 0.12$ $\Delta\phi = 15^\circ$	$\Delta\eta = 0.09$ $\Delta\phi = 5^\circ$	$\Delta\eta = 0.1$ $\Delta\phi = 5^\circ$
Sampling	Scintillator	Scintillator	Gas	Gas
$\Delta E/E$	$70\%/\sqrt{E}$	14% at 50 GeV	14% at 50 GeV	$125\%/\sqrt{E}$
Absorption lengths	$\sim (4/\sin\theta)\lambda_{abs}$			
Radiation lengths	$(64/\sin\theta)X_0$			

Table 2.3: Calorimetry Characteristics

Central Calorimeters: Wedges and Arches

Just outside the solenoid are the four ‘arches’ of the central calorimeter. An arch is 12 calorimeter wedges stacked on top of each other, to form an upright semi-circle. Two arches side-by-side touch at $\eta = 0$ and extend to $\eta = \pm 1.0$. Arches face each other from opposite sides of the detector to cover the full $\phi = 2\pi$ azimuth. A wedge is the basic unit of the central calorimeter, and is shown in figures 2.6 and 2.7. The figures show several key features:

- There are 10 projective towers, with $\Delta\eta = 0.1$. Tower 0 has an edge at $\theta = 90^\circ$;
- Wedge azimuthal coverage is $\phi = \frac{\pi}{12} = 0.26$ radians, or 15° ;
- Light from the scintillator layers travels through a lightpipe to photomultiplier tubes (PMTs) sitting at the top of the wedge. Each tower has 2 PMTs, at left and right. Relative pulse heights in the left and right PMTs give ϕ information;
- The hadronic and EM calorimeters have separate PMTs. Light from the shower counter is wave-shifted before transport in the light pipe;
- Above the hadronic calorimeter there is an opening allowing access to the enclosure where the central muon chambers are installed. Tracks from the CTC traverse wedges to reach the muon chambers;
- All electronics, gas systems and high voltage for a wedge are mounted on the deck where the PMTs are;

Muon Tracking

Muon detection at CDF is divided into three distinct regions of angular coverage. The central region ($55^\circ \leq \theta \leq 125^\circ$) is a main topic of this thesis and is reviewed in the next section. The intermediate regions ($17^\circ \leq \theta \leq 55^\circ$ and $125^\circ \leq \theta \leq 163^\circ$) have no muon detection, although upgrades are on the drawing boards. The forward and backward regions ($2^\circ \leq \theta \leq 17^\circ$ and $163^\circ \leq \theta \leq 178^\circ$) each have twin magnetized steel toroids between three sets of drift chambers. As one of the last major subsystems in CDF to be built, the FMU detector had many problems with background radiation, triggering, and

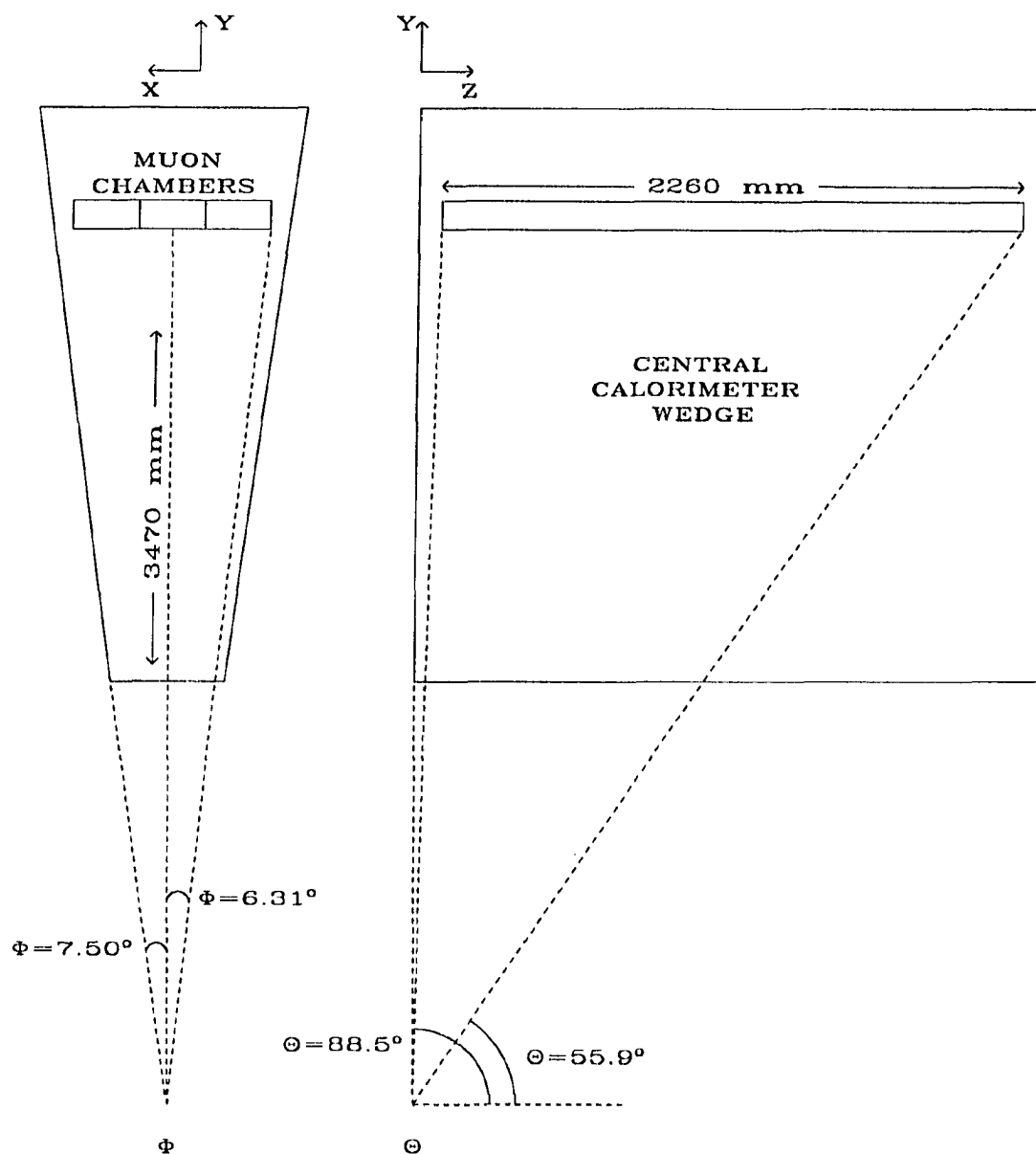


Figure 2.6: Central calorimeter 'wedge'. Note the opening for the muon chambers.

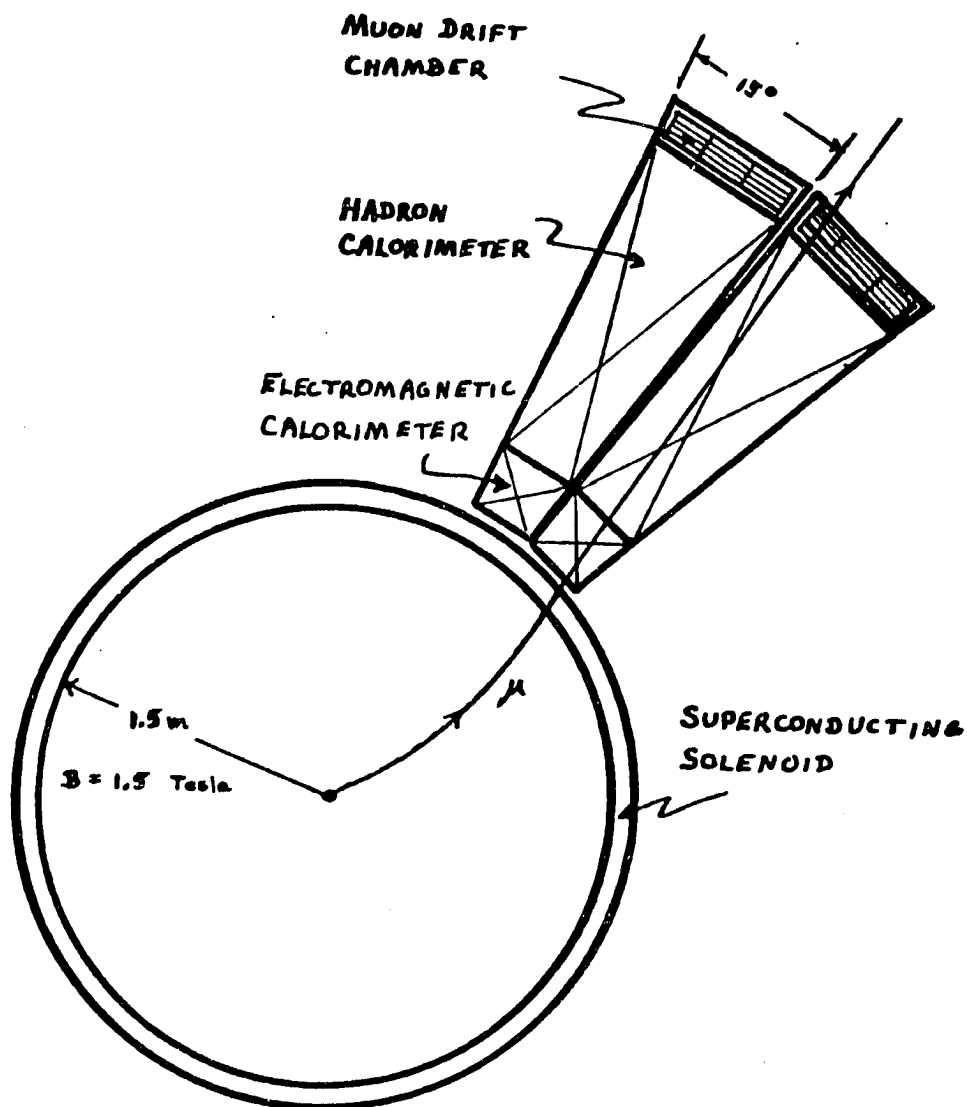


Figure 2.7: Central wedge shown in relation to the rest of the central detector.

electronic noise during the 1987 run. Very little useful forward muon data was recorded, and none of that data was used in the Beauty search.

2.3 Central Muon Chambers

The central muon system uses wire proportional drift chambers to measure charged particle tracks passing through the central calorimeter wedges. Reference [1] describes the chambers in detail, but this section reviews the main features.

2.3.1 Principles of Operation

Charged particles traversing matter ionize some of the molecules. In a wire chamber, that matter is a gas surrounding a fine wire at high positive voltage. The electric field around the wire makes the cations drift away from and the electrons drift towards the wire. The electron drift is not uniform: an electron accelerates in the field until it strikes a gas molecule and scatters in some new direction. The net drift of the electron cloud towards the wire is much slower than the speed of single electrons. Given enough energy, an electron will ionize the molecule when it scatters, making more free electrons. The electric field strength near the wire increases as $V(r) \propto \frac{1}{r}$, so as the electron cloud approaches the wire the electrons reach higher energies between collisions, produce more free electrons, and make an electron avalanche. Particle detection in a wire chamber consists of measuring the charge pulse deposited on the wire [19]. Table 2.4 gives a feel for the quantities involved.

2.3.2 Geometry

Gross features

Each central calorimeter wedge contains a set of three muon chambers. Figure 2.8 illustrates a single chamber. The chambers are aluminum except for G-10 strips insulating the I- and C-beams (field shaping cathodes) from the grounded planes between layers, and except for the G-10 outer walls. The set is divided into three separate chambers allowing installation through the access hole shown in figure 2.6. The 3 chambers have different projective geometries, for the different ϕ positions. The wires run the length of the wedge, about 230 cm. Since there are 48 wedges in the central detector, the central muon system

Gas	50-50 Ar-ethane, 1% ethanol
Pressure	Atmospheric
V_{anode}	+3100 V
$V_{cathode}$	-2500 V
Wire length	460 cm
Wire diameter	50 μm
Wire resistance	1.1 $k\Omega/\text{m}$
Ionization	75 ion-electron pairs per cm
Charge per pulse	100 pC
Drift Velocity	45 $\mu\text{m}/\text{nS}$
^{55}Fe sources	2 per cell (4 per wire)
Maximum drift time	700 nS

Table 2.4: Drift Cell Parameters.

uses 144 drift chambers. The chambers have 4 layers in the radial direction, the direction along which the particles travel, and there are 4 cells per layer, or 16 cells per chamber. Wires from alternating cells in the same layer are connected together at the $\theta = 90^\circ$ end of the wedge so that there are 8 anode sense wires per chamber, and 1152 in the entire detector.

Charge Division

A particle traversing the chambers ‘hits’ a wire in each of the four planes. The z-coordinate of the hit comes from charge division. That is, the wire is resistive so that as the charge pulse propagates to both ends of the wire, it is attenuated by an amount proportional to the distance traveled. The relative pulse heights at the two ends of the wire give the location of the hit along the wire. The unitless coordinate is

$$R = \frac{Q_L - Q_R}{Q_L + Q_R}$$

where Q_L and Q_R are the charge collected from the left and right ends of the wire, respectively. Charge integrating amplifiers measure Q_L and Q_R . To convert R to the coordinate z requires calibration of the impedances in the amplifier circuit and of the wire

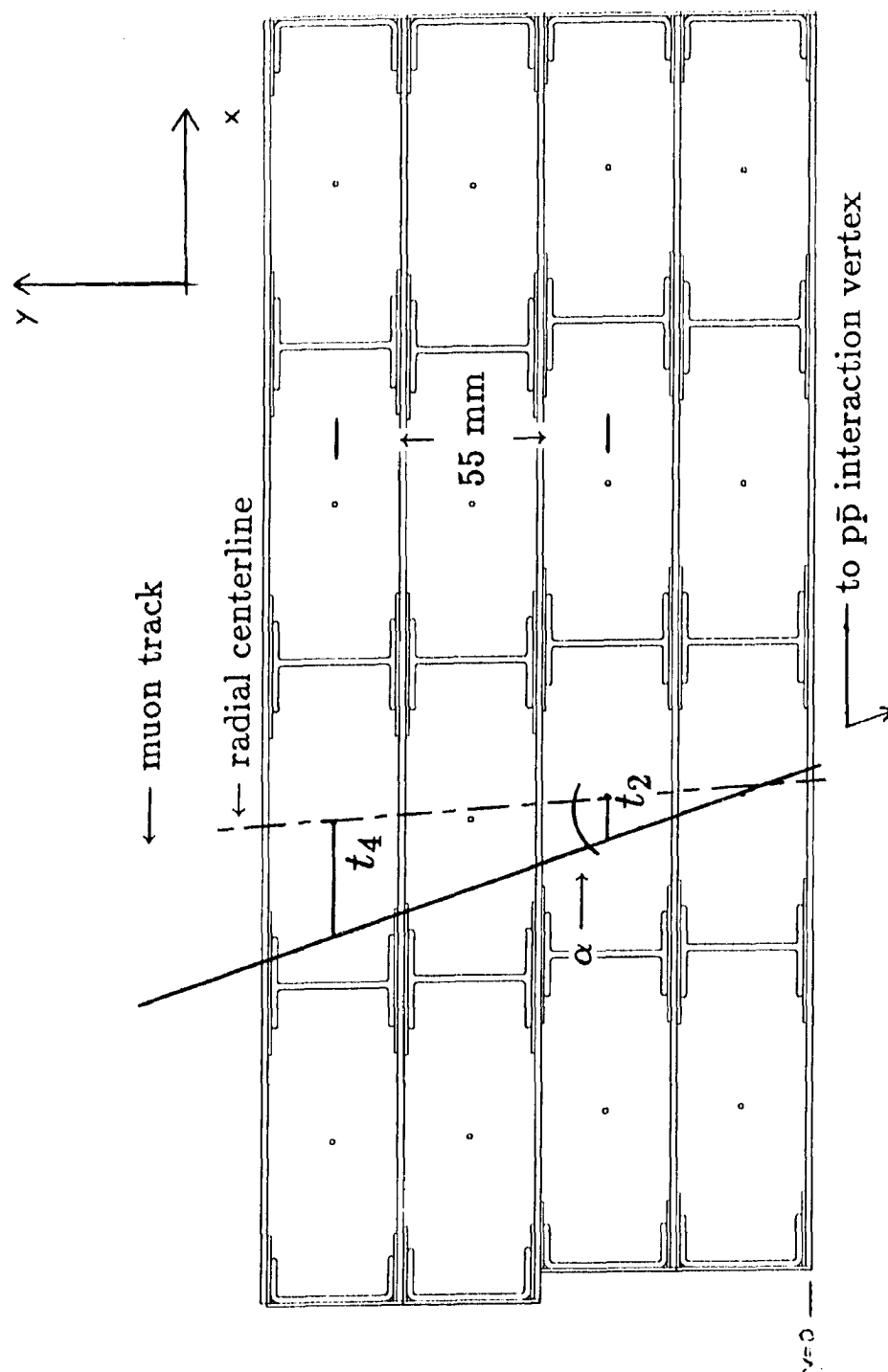
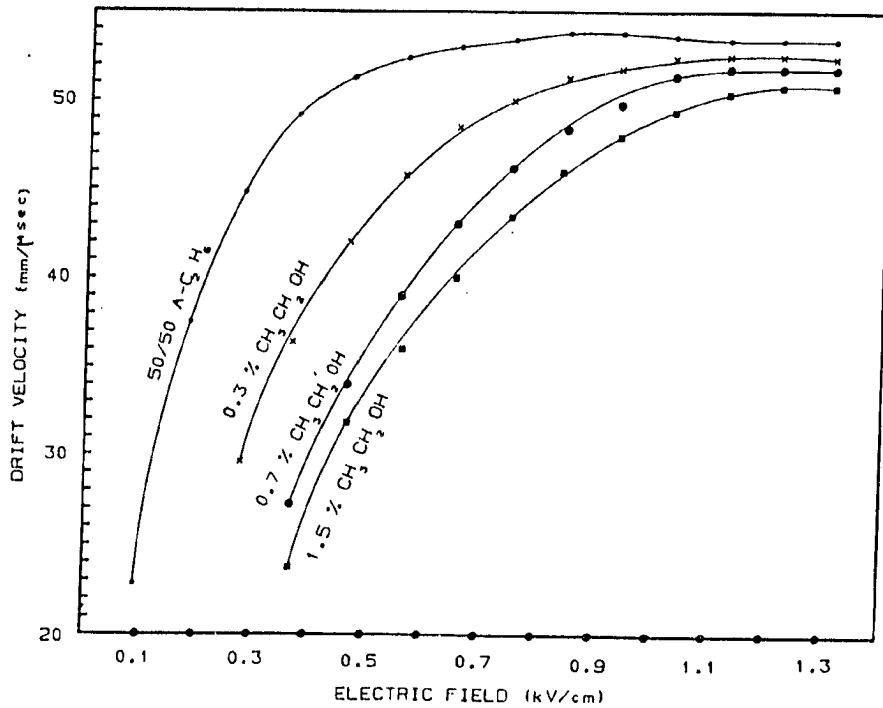


Figure 2.8: Cross section of a single module of the central muon chambers. There are three modules per wedge.



M. Atac, private communication (1983)

Figure 2.9: Drift velocity in argon-ethane gas mixture, as a function of field strength. Muon chamber cells are designed so that v_{drift} is always above the ‘knee’ of the curve.

location. The chambers contain weak ^{55}Fe x-ray sources at precise locations along the wires for fiducial z measurements. These and other details are explained in reference [1].

If a given wire receives more than one hit, the charge pulses interfere and the z -information is lost. A knock-on electron (δ -ray) from a track passing through the aluminum wall of the chambers may hit the wire in the cell adjacent to the cell where the track passed. Such a δ -ray would obscure the z -position of the track. So alternate cells, instead of adjacent cells, are ganged together.

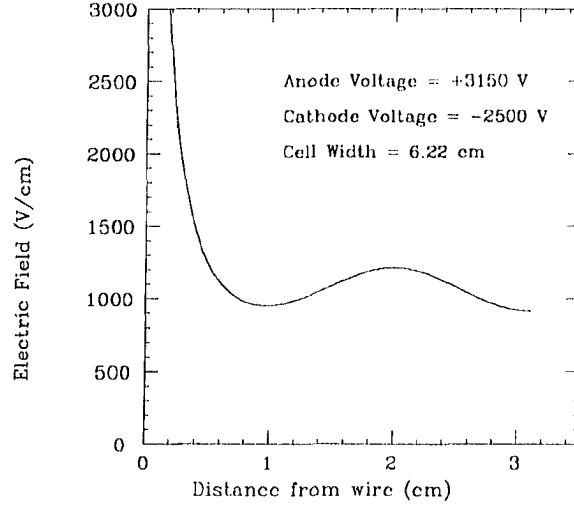


Figure 2.10: Electric field profile inside a cell of the central muon chambers. Drift velocity is roughly constant for field strengths above minimum value.

Drift Distance

Pulse timing and the electron drift velocity v_{drift} together give the position of the track in the direction transverse to the wire,

$$x = v_{drift} t_{drift},$$

where t_{drift} is the time after the $p\bar{p}$ collision that the hit reached the wire, and x is the transverse coordinate. (Various offsets due to the transit time of the particle between the vertex and the chambers, cable lengths, etc., are compensated for.) Time-to-Voltage circuits measure the drift time, as described in the section on electronics. To insure a constant drift velocity over the cell volume, the side walls of the cell are at -2500 volts, giving the field strength profile shown in figure 2.10. Figure 2.9 shows the drift velocity of the electron cloud as a function of the electric field. (Our gas mixture includes about 1% alcohol, intermediate between the lowest two curves in figure 2.9.) Above 900 V/cm the drift velocity depends weakly on field strength. The minimum field strength in figure 2.10 is above 900 V/cm.

Wires in alternate layers, in a given ϕ cell, lie on a radial centerline for reasons explained below. The offset between the centerlines of the two pairs of wires in a ϕ cell is 2 mm, as can be seen in figure 2.8. The offset yields the drift velocity,

$$v_{drift}^{-1} = [(t_1 - t_4) - 3(t_2 - t_3)]/4d \quad (2.6)$$

where t_1, t_2, t_3 , and t_4 are the drift times for each of the four wires in a tower, and $d = 2\text{mm}$ is the offset. A drift velocity measurement is shown in figure 2.16. The 2 mm offset also eliminates any left-right ambiguity in track reconstruction.

Track Angle and Momentum Selection

The locations of the hits in z and ϕ give the directions of a track in both the rz - and $r\phi$ -planes. Tracks in the muon chambers are treated as straight lines (the chambers are outside of all but the weakest fringes of the magnetic field):

$$z = \alpha_z r + z_0 \quad x = \alpha_x r + x_0. \quad (2.7)$$

(x is a coordinate in the ϕ -direction in the local wedge coordinate system. See appendix A.) The $r\phi$ -track direction is particularly interesting because of the deflection of the track in the central magnetic field. Measuring the angle of the track relative to its original direction gives the track momentum. Unfortunately, multiple scattering in the steel causes poor momentum resolution (r.m.s.),

$$\frac{\delta p}{p} \simeq 60\% \quad (p < 100\text{GeV}/c) \quad (2.8)$$

independent of track momentum. Even so, the momentum determination by angle measurement helps reduce the trigger rate, and reference [24] describes the central muon level 1 trigger system that makes a cut on track angle to reject soft muons in our chambers.

For the hardware angle cut (momentum cut) to work (and also to simplify offline pattern recognition) the chambers are constructed so that pairs of wires on alternate layers, in the same ϕ cell, point to the interaction vertex along a radial centerline. An infinitely stiff track emanating from the collision vertex would follow a radial centerline. The angle of a track relative to this centerline is inversely proportional to its momentum,

$$\alpha = 140 \text{ mR}/p_t.$$

(Refer to figure 2.18. For this reason the ϕ cells of the muon chambers are projective: close examination of figure 2.8 shows that cells further from the center (in ϕ) are canted so that all the cells point back to the vertex. During installation the chambers are adjusted so that wire pairs are indeed aligned with radial centerlines. This is the purpose of the electronic alignment system described in reference [23].

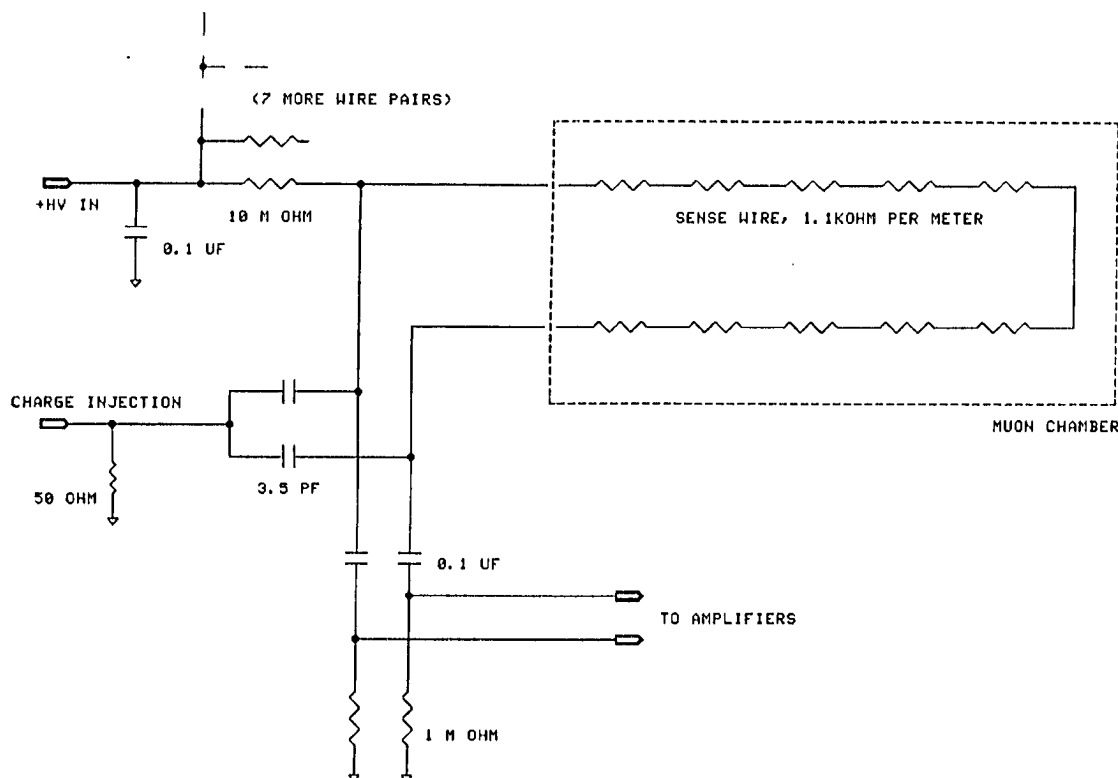


Figure 2.11: Circuit used in the end-electronics to extract the charge pulses from the chamber wires. Pulses are sent directly into the MAT card.

2.3.3 Mechanical Details

End Electronics

Small electronics modules bolted to the ends of the chambers get voltages in and signals out. Short pieces of conductive rubber compressed between metal pads on the end electronics and copper feed-throughs connected to the wires and to the shaping cathodes assure the high voltage connections. Signal connectors bring the charge pulses from the wires to the Rabbit front-end amplifiers. Figure 2.11 shows a schematic of the circuit used to read out the wires. The large blocking capacitors transmit only the high-frequency pulse to the wires, and the large resistance provides current-limiting to prevent wire damage.

The wires can be ‘pulsed’ for testing, diagnostics, and calibration by injecting charge through the end electronics. There are coaxial cable connectors and capacitive couplings

to the wires for this purpose. Pulsing was used to measure channel-to-channel variations in cable delays for drift time calibrations.

Plus Volts

The wires are held at +3100 volts. A LeCroy HV4032 system supplied positive high voltage. Each wedge had a separate voltage channel, with the 3 chambers in the wedge daisy-chained together. Computer and CAMAC control of the LeCroy system allowed monitoring of the currents and voltages.

Minus Volts

The field shaping cathodes (the I- and C-beams) are at -2500 volts to provide the voltage profile shown in figure 2.10. The cathodes are more robust than the wires and require less care to prevent damage from excessive current. Eight channels of Droege-type power supplies were used, and half-arches were daisy-chained together through a distribution box built for that purpose. The Droege supplies, like the LeCroy supplies, have adjustable current-threshold circuit-breakers. Trips induced by hot wires or sudden radiation bursts from the accelerator were monitored by computer.

Gas

A 50-50 mixture of argon-ethane with 1% ethanol flowed through the chambers via a manifold on the arches. The ethanol quenches hot spots that sometimes occur in wire chambers, a hot spot being a localized corona on the wire or on a speck of dirt in the chamber that can cause electronic noise and/or chamber damage. Bubblers at the output end of each wedge monitored flow. Technicians monitored oxygen leaks and generally caused trouble. Gas was a pain in the neck: what more can I say?

Installation

The chambers are inserted into the opening at the top of the wedge (figure 2.6): first the outside chambers, then the middle chamber. The 3 chambers are bolted together. Machined mounting plates, epoxied to the 90° end of the outside chambers and to the 55° end of the middle chamber, align with holes in the steel of the top deck of the wedge. This

deck accommodates the front-end electronics, gas and high-voltage distribution systems, etc, for all the wedge systems. A special bolt passes through the hole and attaches to the mounting plate. Tightening the bolts lifts the set of chambers so that they hang inside the enclosure. The 3-point suspension makes adjusting the chamber orientation in the rz - and $r\phi$ -planes very easy. The bolts are not rigidly attached to the steel deck, but slide freely on C-plates screwed to the deck so that thermal expansion and contraction cause no stresses or strains on the chambers.

2 3.4 Main Ring Background

Antiproton production continues during a store, and the proton loss during Main Ring acceleration sends a large flux of particles into the CDF detector. The eight wedges at the top of the detector are exposed to the Main Ring through a gap in the steel of the magnetic field yoke that shields the other wedges. The muon chambers covering the region

$$60^\circ < \phi < 120^\circ$$

were saturated for most of the run. This is one-sixth of the coverage! Figure 2.12 shows the muon chamber wire current for a set of chambers near the main ring and for chambers at the bottom of the detector, which are shielded from the main ring by the calorimeter. Also shown, in arbitrary units, is the intensity of the Main Ring beam. The currents can permanently damage the wires, and we had to reduce the voltages from the nominal +3100 volts to 2800-2900 volts, making the chambers inefficient. The effect of the voltage reduction on the ϕ -acceptance of the muon system is discussed later.

2.4 Data Acquisition Electronics

2.4.1 Overview

Most of the information available from the CDF detector is useless. That's because the interesting events are rare. Only a fraction of the $p\bar{p}$ collisions produce reactions of interest to a given physics study, and events produce zeroes in most of the electronics channels. To keep the physicists and the computers from being overwhelmed by a flood of irrelevant numbers, the data acquisition system is designed to reduce the flood to a trickle. Also,

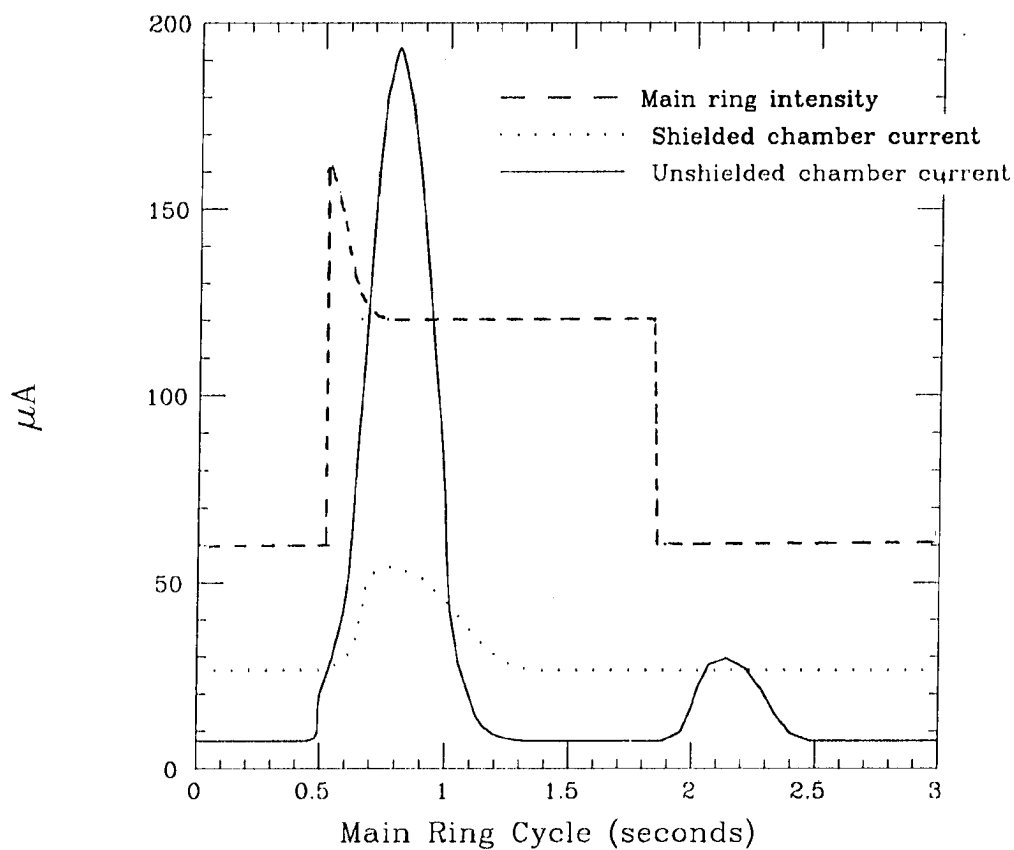


Figure 2.12: Plot of main ring beam intensity and muon chamber anode current. Chamber current soars at beam injection and extraction times due to beam losses and consequent radiation.

the process of digitizing thousands of signals and then writing the numbers to magnetic tape is slow. Events occurring during this deadtime are lost, hence the more selective the data acquisition system, the fewer events are missed. The trigger is the portion of the electronics that selects the choice events, while the sparse scan feature keeps zeroes from being written onto the data tapes.

Table 2.1 shows some rates. Two percent of the collisions produce hits in the muon chambers. Of these hits, less than 1% are due to genuine prompt muons, the rest coming from pion and kaon punch-through or decay. The more discriminating the trigger, the less beam time is lost writing ‘junk’ to tape, and the less computer and physicist time is spent extracting the signal from the data sample. Furthermore, since the muon only traverses one chamber, sparse scan can remove most of the 1152 wires in the central muon chambers from the event record.

The following sections describe the central muon electronics. Figure 2.13 gives an overview of the system. A signal from the chambers goes into the Rabbit front-end amplifiers. After shaping, the signals leave the Rabbit crate via two pathways: ‘fast’ outputs for trigger processing, and digitized outputs to be written onto magnetic tape. Both paths traverse the FastBus network that is the heart of the CDF electronics. If an event satisfies the trigger, then the FastBus trigger section instructs Rabbit, via the MEP FastBus module, not to accept further collision information until all signals have been digitized and read out. Once the digitized data is loaded into the MX buffers, Rabbit resumes collision information processing while the Vax computer reads the MX buffers and writes the data to tape.

2.4.2 Rabbit Electronics System

The muon front end electronics are part of the Rabbit ² system, designed and built at Fermilab and described in detail in reference [21]. Following is a short description. An appendix describes the debugging and calibration of the front-end amplifiers.

A Rabbit card (or module) is 12.5 by 17 inches, and plugs into a crate with 24 slots. All slots are electrically connected to bus lines on the backplane of the crate. Lines include addressing, timing signals, digital data transfer, power supplies, and, as the name implies,

²RABBIT is an acronym for Redundant Analog Bus Based Information Transfer.

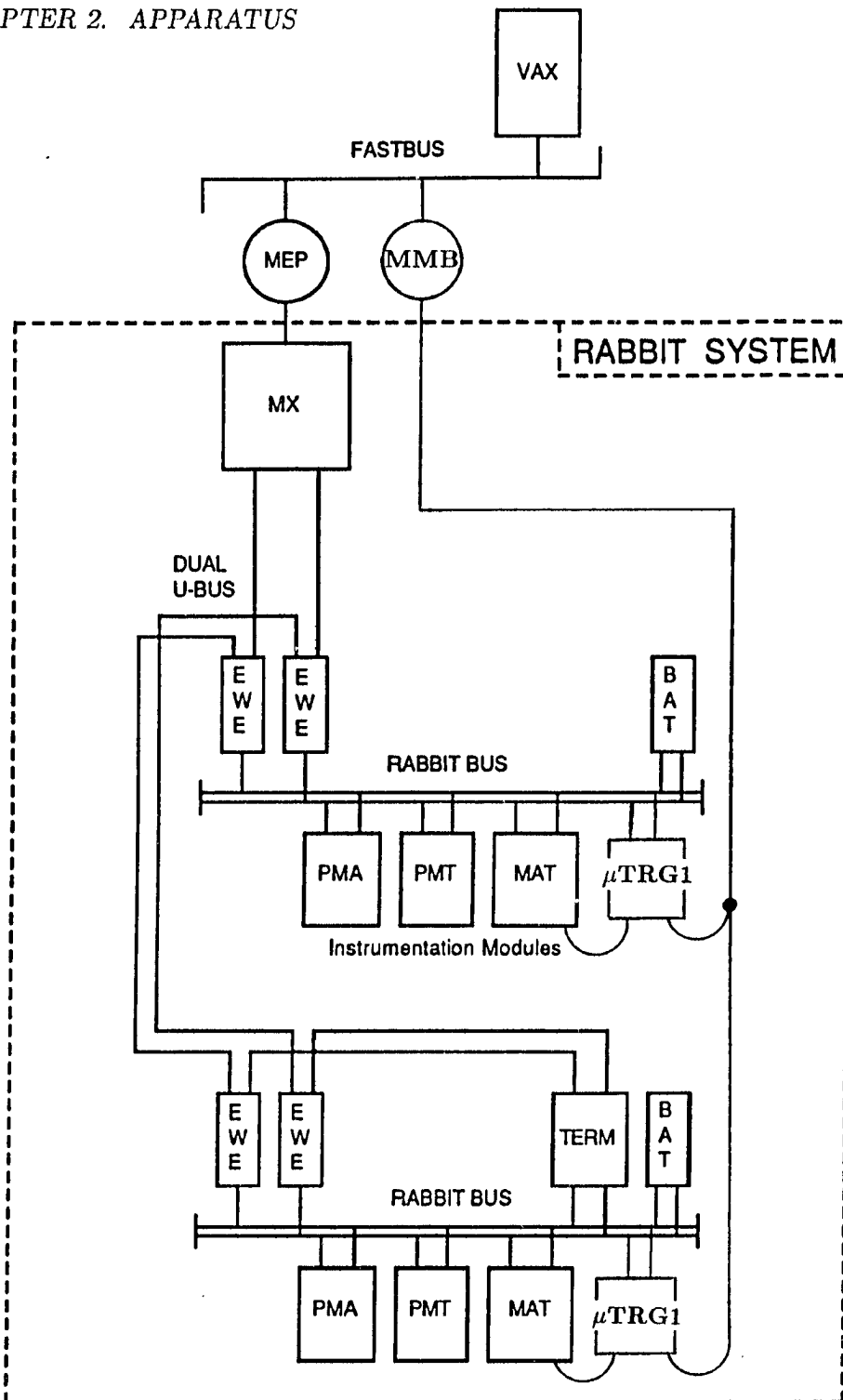


Figure 2.13: Overview of the central muon electronics system, showing both the data and trigger paths from the chambers, through the front-end electronics, and into the FastBus network.

an analog bus. The redundant aspect is that there are two sets of most lines (a top bus and a bottom bus), to provide a backup in case of circuit failure when the detector is inaccessible.

All Rabbit cards are slaves to a crate controller called a EWE. The EWE has a 16-bit Analog-to-Digital Converter (ADC) to digitize the analog signals in the crate, at $17 \mu\text{s}$ per digitization. The EWE also contains Digital-to-Analog Converters (DAC's) for analog pedestal subtraction and for threshold discrimination before digitization. The EWE is a slave to whatever processor is plugged into its front panel. In the CDF data acquisition system, that processor is the MX, described in another section. (In test and calibration stands use other processors, typically small computers.) Hence the EWE, upon instruction from higher up in the acquisition chain, selects an amplifier channel from some card in the crate to be multiplexed onto the analog bus, subtracts voltage offsets (pedestals), tests for threshold discrimination, digitizes, and passes the digital information to the controlling processor. The EWE has many features for flexibility in accessing information from the cards for a given subdetector.

The Rabbit cards use charge-integrating amplifiers (QVC's, or Q(charge)-to-Voltage Converters) and Time-to-Voltage Converters (TVC's). These require timing signals synchronized with the $p\bar{p}$ collisions, generated by the other essential card in a Rabbit crate, the BAT (Before-After Timing). The BAT receives a master clock pulse directly from FastBus, gated with the colliding beams, and generates several other gates needed by the different types of QVC's and TVC's for the different subdetectors serviced by any given Rabbit crate. The timing signals are bussed from the BAT to the other cards in the crate.

2.4.3 The Muon ADC/TDC card

The Muon ADC-TDC card, or MAT, is the Rabbit module which shapes the raw pulses from the central muon chambers. The relative pulse heights from the two wire ends gives the longitudinal coordinate of the track, and the timing of the hit relative to the $p\bar{p}$ collision gives the lateral coordinate. There is one MAT per muon chamber. Hence, each MAT has 16 QVC'S and 8 TVC's. Table 2.5 lists circuit parameters.

Figure 2.14 shows a simplified MAT amplifier circuit. The QVC uses a field-effect transistor to provide a low noise integrating amplifier. The charge is integrated on capacitor C_4 . Capacitors C_1 and C_2 are used to sample-and-hold the output voltage. The BFORE

	QVC	TVC
Circuits per card	16	8
Gain	3.8 fC/count	58 ps/count
Threshold		4 pC
Saturation	250 pC	3.8 μ s
Input impedance	100 Ω	

Table 2.5: Typical Parameters of the ADC/TDC card.

timing gate from the BAT opens the switch S_1 before $p\bar{p}$ beam crossing to measure the reference voltage V_{bef} (see figure 2.15). The AFTER gate opens switch S_2 after the maximum drift time plus the full integration time has elapsed (≈ 1100 ns), leaving voltage V_{aftr} on C_2 . Then the total charge for the hit is $Q = (V_{bef} - V_{aftr})C_4$. The voltages are multiplexed via the analog bus to the ADC in the EWE.

For the TVC, the inputs from each end of the chamber wires are buffered, summed together, and passed to the comparator. If the pulse is above threshold the switch S_3 changes state and the capacitor C_3 charges linearly, supplied by the constant current source I until the STOP gate from the BAT changes the switch to a state where the voltage on C_3 is held. For simplicity, figure 2.14 does not show a second switch whereby RESET forces C_3 to discharge. Also, RUN/STOP enables and disables the switches, with RUN just before beam crossing, and STOP after the maximum drift time has elapsed. The HIT signal is cabled directly to the Trigger Level 1 card where it is used to recognize high momentum tracks. Figure 2.15 outlines the timing.

2.4.4 Vax and MX

The goal of the acquisition chain is to get the data into the Vax host computer and onto the magnetic tape. The MX is the name of the processor designed specifically for this goal. Each MX controls four Rabbit crates (four EWEs). Before a data run, the MX memory is loaded with the addresses of all the amplifier channels, their individual pedestals, thresholds, gains, and polarities, and the sequence of channels to be read. After a valid trigger, FastBus instructs the MX to scan the crates, and the signal for every

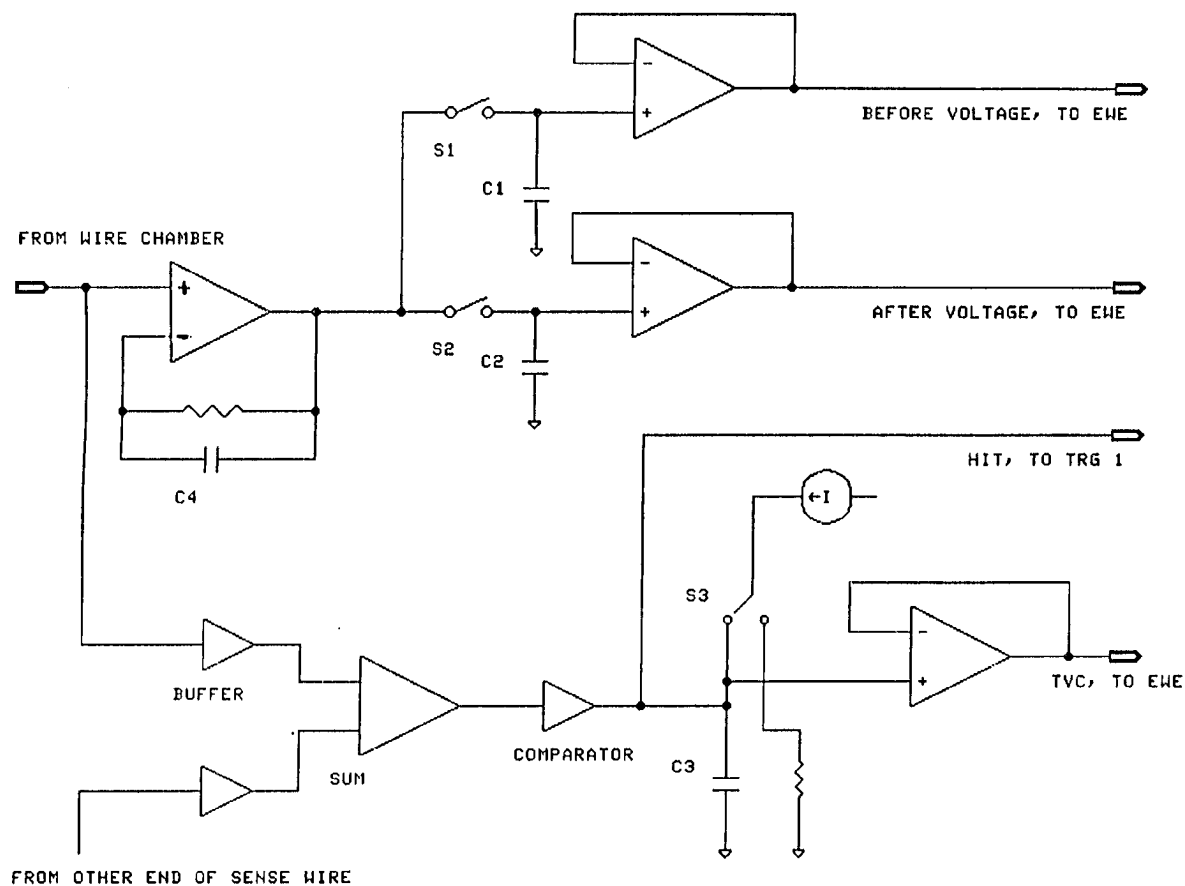
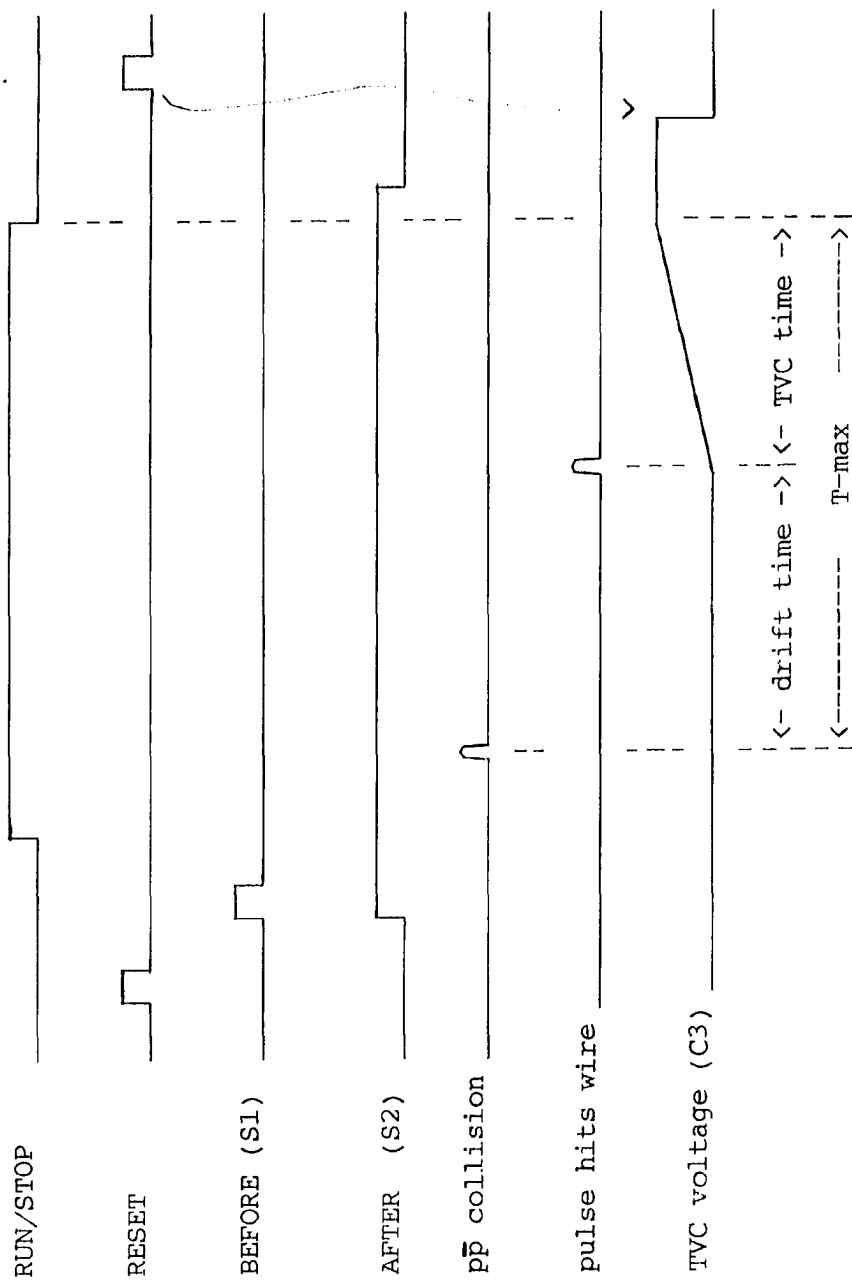


Figure 2.14: Simplified schematic of the muon charge-to-voltage converter and the time-to-voltage converter circuits (QVC and TVC).



(not to scale)

Figure 2.15: Muon ADC/TDC timing.

<i>Description</i>	<i># of constants</i>	<i>Units</i>
QVC pedestals	2304	ADC counts
TVC offsets	1152	ns
QVC gain	2304	fC/count
TVC gain	1152	ps/count
T_{max}	1	ns
^{55}Fe	4608	cm
Wire locations	96	cm
Survey data	144	cm
Total	$\sim 12,000$	

Table 2.6: List of Calibration Constants.

channel above threshold is digitized and loaded into MX memory. When the Vax is free to read a given MX, of which there are about 60, the data passes through the MEP and up the network to the FastBus/Vax interface. With over 150 crates, the CDF FastBus network is the largest in the world (see figure 2.13).

2.4.5 System Calibration

A charged particle passing through the chambers induces a charge pulse on a few wires. The charge pulse is shaped, amplified, digitized and stored on magnetic tape for offline analysis of the track location and direction. In the evolution of the signal from a raw charge pulse to an accurate momentum vector, useful for physics analyses, are many stages of corrections and calibration constants.

An appendix describes the calibration of the MAT TVC circuits. Table 2.6 lists the offsets and corrections that have to be included in the track finding. These 12,000+ constants are stored in a database accessible to the pattern recognition code. The next sections describe how they are measured.

Pedestals and Gains

All pedestal values in the Rabbit system were measured once per shift during the Tevatron run. The pedestals are stored in a database on the Vax cluster at B0. At the beginning of a data run, the pedestal values are downloaded to the MX's. When a Rabbit channel is above threshold and is to be read, the MX writes the pedestal value for that channel to the pedestal DAC register in the EWE. The DAC converts the digital pedestal value to an analog voltage, which is subtracted from the signal voltage using operational amplifiers in the EWE before the signal is digitized. Hence digitized data coming from the Rabbit crate needs no further pedestal subtraction.

Charge Division

Charge division uses the relative amplitudes of the attenuated charge pulses at the two ends of the wire to find the position of the hit along the wire. The parameter

$$R = \frac{Q_L - Q_R}{Q_L + Q_R}$$

has values in the range $R_{min} \leq R \leq R_{max}$, where Q_L, Q_R is the charge collected from the left and right ends of the wire, respectively. In practice, $|R_{min}|, R_{max} < 1$, due to the non-zero input impedance of the charge-integrating amplifiers [1]. To convert R to the coordinate z , in centimeters, we use ^{55}Fe x-ray sources built into the chambers at precisely located positions along the wires. We find the R values of the hits due to the sources, and knowing where the sources are in z , the conversion from R to z is simple. To obtain a data sample of hits due primarily to the ^{55}Fe sources the trigger level 1 card is set to accept single hits.

Drift Distance

To convert TDC counts to a drift distance from the wire, in centimeters, requires three principal constants: the drift velocity v_{drift} , the timing offset t_{max} , and the TVC gain g_t . To understand t_{max} remember that earlier hits give larger TVC outputs (see figure 2.15) and the largest TVC output occurs when the track passes closest to the wire, i.e., when the shortest drift delay produces the earliest hit. Then the drift time is

$$t_{drift} = g_t \times (TDC_{max} - TDC_{measured})$$

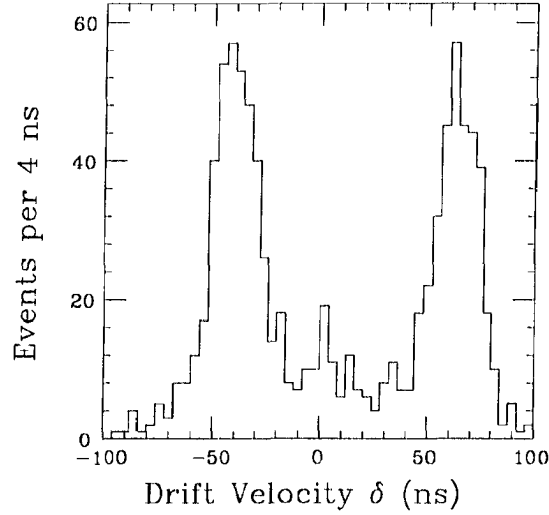


Figure 2.16: Distribution of δ used to measure the drift velocity.

where g_t is in picoseconds per ADC count (table 2.5)³. The drift distance is simply

$$d_{drift} = v_{drift} \times t_{drift}.$$

Drift velocity is measured using the 2mm offset between the radial centerlines that the wire pairs in alternate layers lie on (see section on chamber geometry, under ‘drift distance’)[1]. Ideally we would use real tracks produced in $p\bar{p}$ collisions but in practice there were too few to make useful measurements. Instead we used cosmic rays, at least for the wedges oriented near vertical (the cosmic ray flux along nearly horizontal radial centerlines is low, and we were unable to accumulate adequate statistics). Figure 2.16 shows a typical distribution for

$$\delta = [(t_1 - t_4) - 3(t_2 - t_3)]/4$$

where t_1, t_2, t_3 , and t_4 are the drift times for each of the four wires in a tower. The width of the peaks reflects the spatial resolution in the drift direction. The separation between the peaks is about 95 ns, giving

$$v_{drift} = \frac{2(2\text{ mm})}{95\text{ ns}} = 42\text{ }\mu\text{m/ns}.$$

As it turns out, our muon studies are fairly insensitive to the value of v_{drift} , within 10 or 15%, because the uncertainty from multiple scattering dominates.

³See the appendix on Rabbit Testing for a description of the g_t calibration.

The MAT TVC circuit measures the time between a charge pulse and the STOP signal. STOP is generated in the Rabbit BAT card that sits in every Rabbit crate, triggered by C/S (Clear & Strobe). C/S in turn comes from the FastBus Master Clock, which is synchronized with the $p\bar{p}$ collisions using timing pulses from the accelerator. C/S propagates through the detector through a network of cables and electronic buffers, each of which adds some delay. Therefore, STOP does not necessarily occur at the same absolute time in every Rabbit crate. The variation has to be measured and corrected for in order to use a single t_{max} for every TDC channel.

To this end we injected charge into the muon chamber wires. Pulsing all wires simultaneously gives the channel-to-channel TDC offsets. The offsets were less than 20 ns, consistent with the circuit design and with the Central Hadron TDC's. Corrections were made for variations in the pulser cable lengths, measured from the time delay between a pulse injected on a cable and the reflected signal.

2.5 Trigger

Now, during the 1988 data run, CDF uses a three level trigger system. Each level makes a more refined decision than the preceding level. The lower levels filter out most of the bunch crossings, while the highest level takes a longer look at a small number of events. The aim of the level 1 trigger is to identify potentially interesting events while incurring no deadtime, that is, within the 7 μ s before the next beam-crossing occurs. For the 1987 data run, only level 1 was operational. Levels 2 and 3 are beyond the scope of this report.

The CMU level 1 trigger requires a match between a stiff CTC track and a stub in the muon chambers. While conceptually simple, this trigger requires sophisticated electronics. Figure 2.17 shows the main components in the CMU level 1 trigger. Muon stubs are identified by the Rabbit Muon Level 1 trigger cards [24]. The stubs are called brass muons because of the large background contamination. The Central Fast Track processor finds the CTC tracks [22], and sends the list of CTC tracks to the CTCX. The CTCX is a FastBus module that translates the ϕ and p_t of the tracks into CMU cell numbers, so that coincidences between the CMU stub and the CTC track can be formed. The coincidence is formed in a crate full of MU2T FastBus cards, called the muon matchbox. A match is called a Golden muon, reflecting the high quality of the data that comes from this trigger.

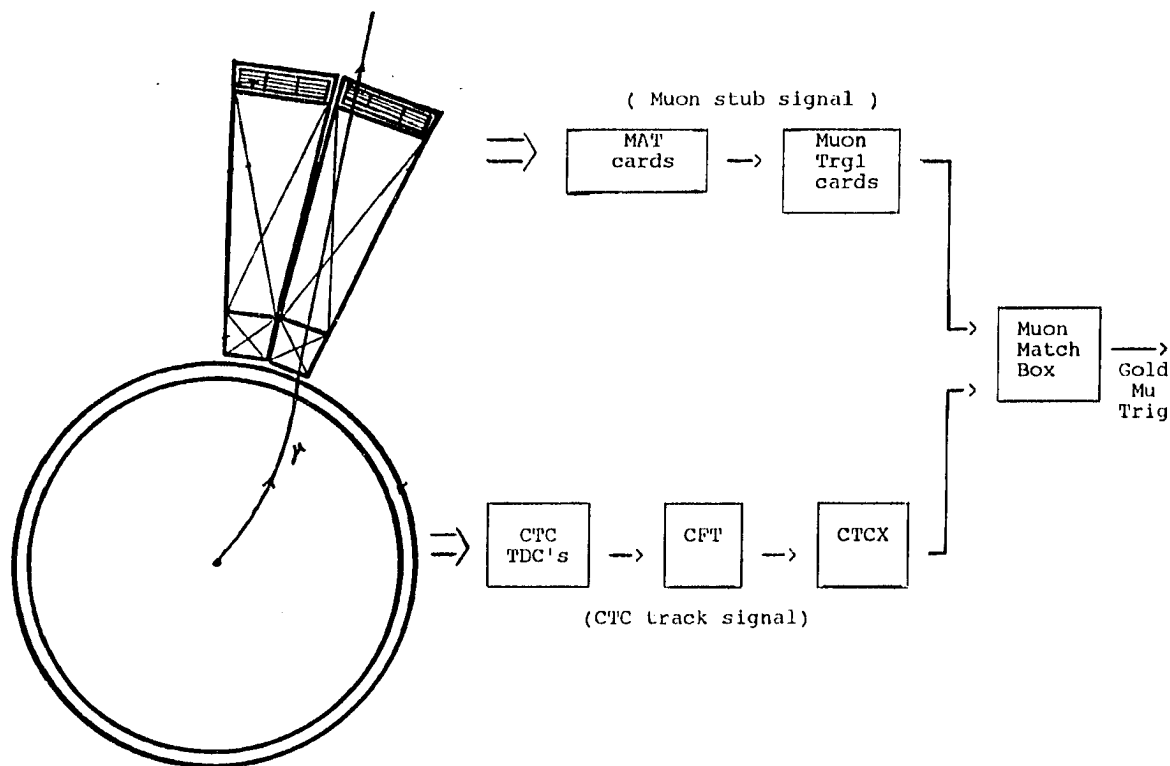


Figure 2.17: Overview of the electronics for the Golden muon trigger. Drift time information from both the central muon chambers and the central tracking chamber is translated into stub and track coordinates, which are matched in the muon matchbox.

The references describe each of the components of the system in detail, but the following sections review the main features.

2.5.1 Brass Muons

Figure 2.8 showed a cross section of a muon chamber ($r\phi$ -view). The wires in the vertical towers lie on radial centerlines from the event vertex. A charged track of transverse momentum p_t is deflected in the central magnetic field by an angle α relative to the radial centerline, and

$$p_t = \frac{0.493 B}{v_d \Delta t} \text{ GeV}/c. \quad (2.9)$$

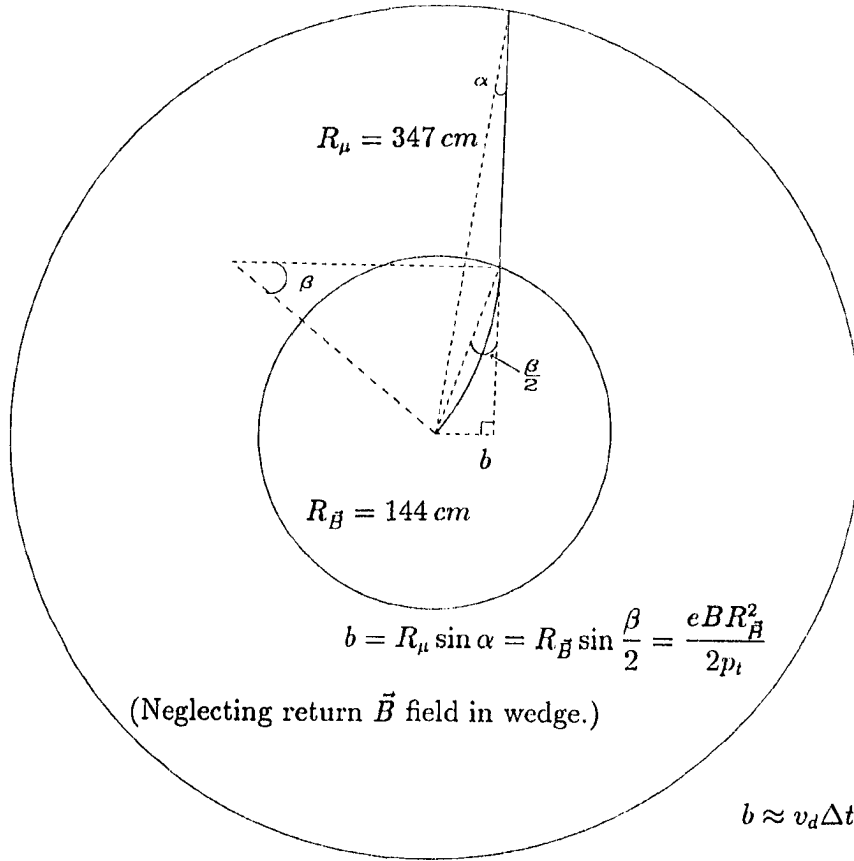


Figure 2.18: Relation between track curvature, transverse momentum, and track angle at the muon chambers.

Δt is the drift time difference for the wires on two alternate wire chamber layers. Figure 2.18 sketches the geometry behind equation (2.9). With magnetic field strength $B = 1.5$ Tesla, drift velocity $v_d = 0.0045 \text{ cm/ns}$, and Δt in nanoseconds,

$$p_t = \frac{164}{\Delta t} \text{ GeV/c.}$$

Hence, requiring that Δt be less than some threshold is the same as requiring that tracks have $p_t > 164/\Delta t$. Figure 2.20 plots transverse momentum threshold as a function of time difference.

A hit on a chamber wire fires a discriminator (A_1 in figure 2.14). The muon Trigger Level 1 card is a Rabbit module that sees when the discriminators for two alternate layers fired, and compares the time difference between the two with a gate of width Δt , adjustable using an addressable DAC. If the time difference is less than the gate width, the trigger is

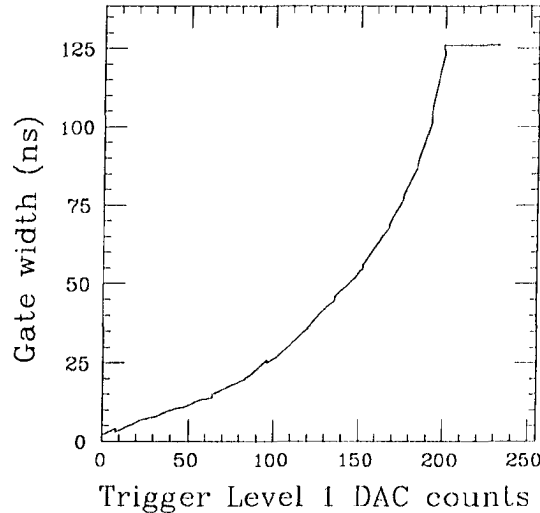


Figure 2.19: Trigger level 1 gate width as a function of gate setting. Useful in conjunction with the following plot.

satisfied. Each of the six ϕ cells in a wedge has a separate trigger bit, these are the Brass muon trigger bits. Cables carry the trigger bits to the counting room where they can be compared with stiff track information from the CTC. Figure 2.19 shows the relation between the DAC setting and the gate width. Combined with figure 2.20, this gives the DAC settings for a given p_t threshold. The individual brass trigger channels were tuned so that the variation in figure 2.19 from channel to channel is slight.

Multiple scattering of charged particles traversing the calorimeter wedges is described by equation (3.2). Multiple scattering changes the angle α of the particle and hence smears the p_t threshold just described. Figure 2.21 shows the calculated p_t dependence of the Brass muon trigger efficiency. Efficiency is only 50% at the nominal threshold described by equation (2.9), hence to assure full efficiency at a given p_t requires setting the DAC to some higher Δt value.

2.5.2 Golden Muons

The muon trigger level 1 card works very well. Unfortunately the rate of stubs in the muon chambers completely swamps the data acquisition capabilities of CDF. The great majority of these stubs are junk, from a muon point of view. They are μ^\pm 's from decay-in-flight of π^\pm 's and K^\pm 's, soft μ^\pm 's and non-interacting π^\pm 's that multiple scatter in the steel and look like stiff tracks, or leakage from hadronic showers that exit the calorimeters

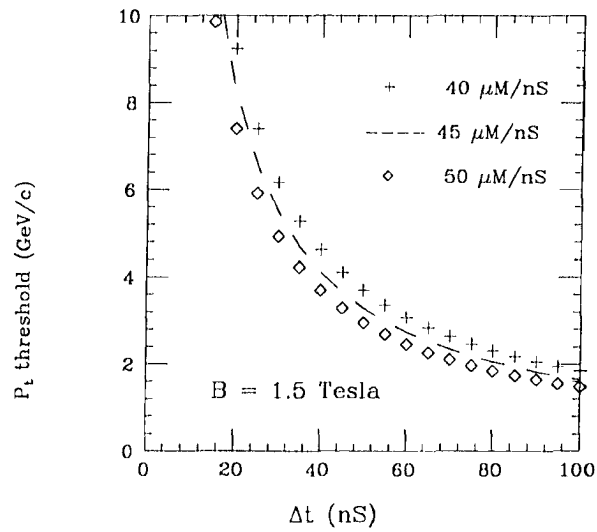


Figure 2.20: p_t threshold vs the cut on the drift time difference for alternate layers, ignoring multiple scattering.

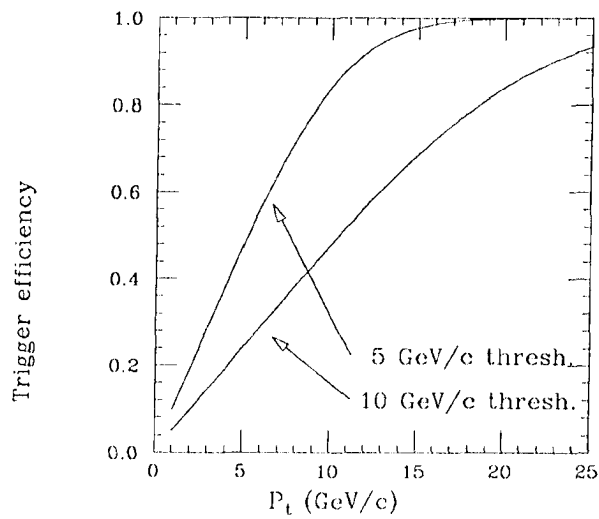


Figure 2.21: Brass trigger efficiency for multiply scattered muons of transverse momentum p_t .

looking like stiff tracks. In addition, cosmic rays and Main Ring loss that are accidentally in-time with the beam crossing also contribute to the raw stub rate. At a luminosity of $10^{29} \text{ cm}^{-2} \text{ sec}^{-1}$ and a p_t threshold of 5 GeV/c the rate for stubs from all 48 trigger level 1 cards is about 9 hz (see table 2.1).

To reduce the rate we simply require a coincidence between the muon stub and a stiff track pointing at the stub. The trick is to reconstruct the CTC tracks and check if any of them have the same ϕ -coordinate as any muon stubs within the 7 μs before the next beam crossing. A special FastBus module called the Central Fast Tracker performs this task [22].

The Central Fast Tracker

The Central Fast Tracker (CFT) is a hardware track-finder which uses fast timing information from the CTC (Central Tracking Chamber) to find high momentum tracks and transmits the p_t and ϕ information for the tracks to the rest of the trigger system. The track finder has 8 programmable thresholds between 2.5 and 15 GeV, and completes a search for all high momentum tracks in an average of 2.5 μs per event. The momentum resolution is $\delta p_t/p_t^2 = 3.5\%$, with a high efficiency that is independent of track density.

Following each beam crossing the trigger processor produces a list of found tracks. The list is transmitted to the CTCX and then to the Muon MatchBox which correlates the tracks with brass muons (stubs), as found by the Trigger Level 1 cards. The CFT finds the tracks so quickly by using lookup tables to compare CTC hit information with possible hit topologies stored in memory.

The CTC Translator (CTCX)

As the CFT forms the list of CTC tracks above the p_t cut, it sends the ϕ -coordinates of the tracks to another FastBus card called the CTCX over a dedicated cable. The CTCX ('CTC Translator') is a single FastBus module with a lot of memory. The memory contains the 'roadmap' to show where a CTC track of given ϕ would be expected to hit the muon chambers, taking into account multiple scattering and the error in the CFT ϕ determination. The bits of the CFT ϕ -word address the CTCX memory, and the contents of that CTCX memory location indicate which wedges could be hit by that track. Cables

from the CTCX to each of the 24 MU2T cards carry the bits that tell whether a given CTC track could be expected to show up in the wedges corresponding to that MU2T card.

Muon Matchbox

The Muon Matchbox is the name of the FastBus crate that houses 24 MU2T cards. The MU2T cards receive the Brass muon bits from the Trigger Level 1 card as well as the list of translated CTC tracks from the CFT, via the CTCX. The MU2T cards preserve the ϕ granularity of the muon chambers, which is six cells per wedge, but the $+\eta$ and $-\eta$ wedges are combined together. The list of p_t and ϕ for any and all muon/track matches is transmitted to the Level 2 processors, where they can be combined with calorimetry information or other triggers for more sophisticated triggers.

2.5.3 Jet Triggers

Chapter 1 explained that the data sample for the $B \rightarrow \mu + \text{jet}$ study comes not from the muon trigger but from the jet trigger. As stated, the jet trigger tests for the total transverse energy $E_t = E \sin \theta$ deposited in the calorimetry (see reference [25]).

The buffered analog outputs of the central calorimeter phototubes reach the counting rooms by cable, where the charge is integrated using operational amplifiers on special FastBus cards. (Similar electronics handles the signals from the gas calorimetry). Electromagnetic and hadronic calorimeter signals are kept apart. A strength of the CDF calorimetry is the fine segmentation, which is exploited at the trigger level: adjacent η towers are summed together as are the left and right phototubes, giving a calorimeter trigger tower size in the central region of

$$\Delta\eta \times \Delta\phi = 0.2 \times 0.26.$$

The sum of the four phototubes is then multiplied by $\sin \theta$, still using operational amplifiers, so that the voltage is proportional to E_t . The E_t voltage for a given tower is compared to a programmable threshold, which was 1 GeV per tower for our data sample. All towers above threshold are summed together, then compared with the $\sum E_t$ threshold.

For the 1987 run the plug and forward hadron calorimeters were not included in the trigger (table 2.3), due to noise problems that made the trigger rates artificially high.

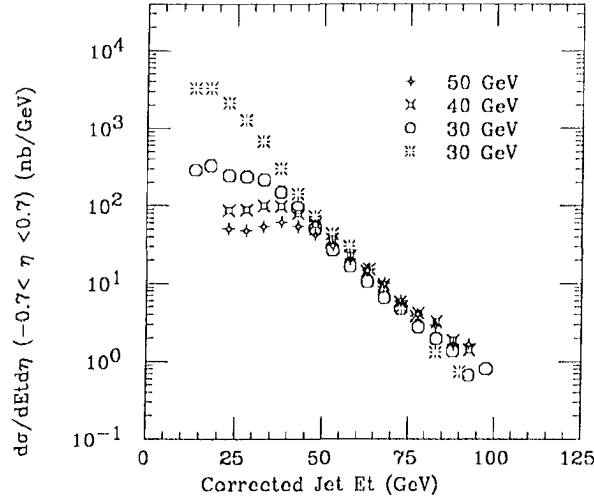


Figure 2.22: Jet differential cross section for different $\sum E_t$ trigger thresholds.

Noise came from electronics problems (cross talk, cable oscillations) and from physics sources (single stray neutrons leaving huge signals in the wire chambers). Since the run the problems have been corrected but they caused bias in the 1987 data.

The goal of the $\sum E_t$ trigger was to study jets. Figure 2.22 gives the number of jets of transverse energy E_t^{jet} that are found using different $\sum E_t$ thresholds. The $\sum E_t = 20 \text{ GeV}$ is fully efficient for $E_t^{jet} > 25 \text{ GeV}$, and the $\sum E_t = 50 \text{ GeV}$ has turned on by $E_t^{jet} > 50 \text{ GeV}$. Remember that jets typically come in pairs: momentum conservation implies that a jet will be balanced by a mate of about the same energy in the opposite direction. Hence one naively expects an event with a 30 GeV jet to have $\sum E_t = 60 \text{ GeV}$, and so the sharp turn-on for E_t^{jet} efficiency at the value of the $\sum E_t$ threshold is partly coincidental.

Table 1.3 showed that the efficiency for B falls rapidly with increasing $\sum E_t$ threshold. The table also shows that 72% of the jet data was taken with the $\sum E_t = 30$ trigger. In the background calculations of the next chapter mainly $\sum E_t = 30$ data is used.

Chapter 3

Muon Identification at CDF

This chapter addresses two questions: first, what will a real muon track look like; second, how many other things will look the same way.

3.1 Muon Signatures

A muon is a penetrating charged particle. It traverses the calorimeter wedges deflected only by small angles and losing only about 1.3 GeV of energy, through multiple coulomb interactions. Muons with $p_t < 1.4$ GeV/c will range out in the steel. Hence the basic signature is a spatial match with a stiff CTC track, and a small calorimeter signal.

3.1.1 Matching Cuts

Figure 2.7 illustrates a muon leaving a track in the CTC and a stub in the muon chambers. The stub and the track point in the same direction, within the deflection by multiple scattering, the detector resolution, and the weak return magnetic field in the hadron calorimeter. The stub direction was described in equation (2.7) as

$$z = \alpha_z r + z_0 \qquad x = \alpha_x r + x_0.$$

To link CTC tracks with muon stubs, we extrapolate the track beyond the CTC, through the calorimeters, and into the chambers. At the muon chambers, the track vector is transformed into the same $\alpha_x, x_0, \alpha_z, z_0$ coordinate system as the muon stub (see appendix A). The differences

$$d\alpha \equiv \alpha_x^\mu - \alpha_x^{CTC}$$

$$dx \equiv x_0^\mu - x_0^{CTC}$$

$$dz \equiv z_0^\mu - z_0^{CTC}$$

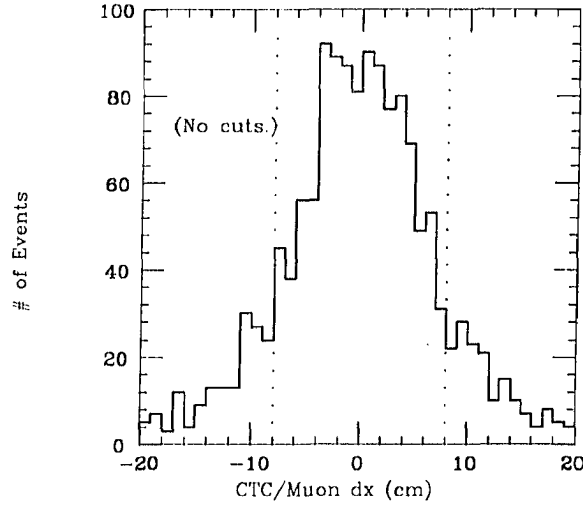


Figure 3.1: Raw dx distribution for muon candidates. Vertical lines show cut.

$ dx < 8 \text{ cm}$
$ dz < 15 \text{ cm}$
$ d\alpha < 60 \text{ mR}$
$0.05 < EM < 0.5 \text{ GeV}$
$0.5 < \text{Hadron} < 3.0 \text{ GeV}$
$p_t > 3 \text{ GeV}/c$

Table 3.1: Muon identification cuts.

define the track match. (The α_z measurement is too poor to use as a cut.) Table 3.1 shows the cut values. The cuts are chosen by studying distributions, to be shown.

The magnitude of the return magnetic field in the steel of the hadron calorimeter has been calculated but not measured. To optimize the track matching we tuned the field strength used in the code to minimize the dependence of dx on track momentum.

Figure 3.1 shows a distribution of all dx for a sample of CTC/muon track matches from minimum bias events, requiring $p_t > 2 \text{ GeV}$ but no other cuts. In figure 3.2, we apply dz , EM, and Hadron cuts (see table 3.1), and again plot the dx distributions for varying minimum p_t values. Superimposed on each histogram is a fit to a gaussian distribution, with the standard deviation σ . Multiple scattering accounts for the change in σ .

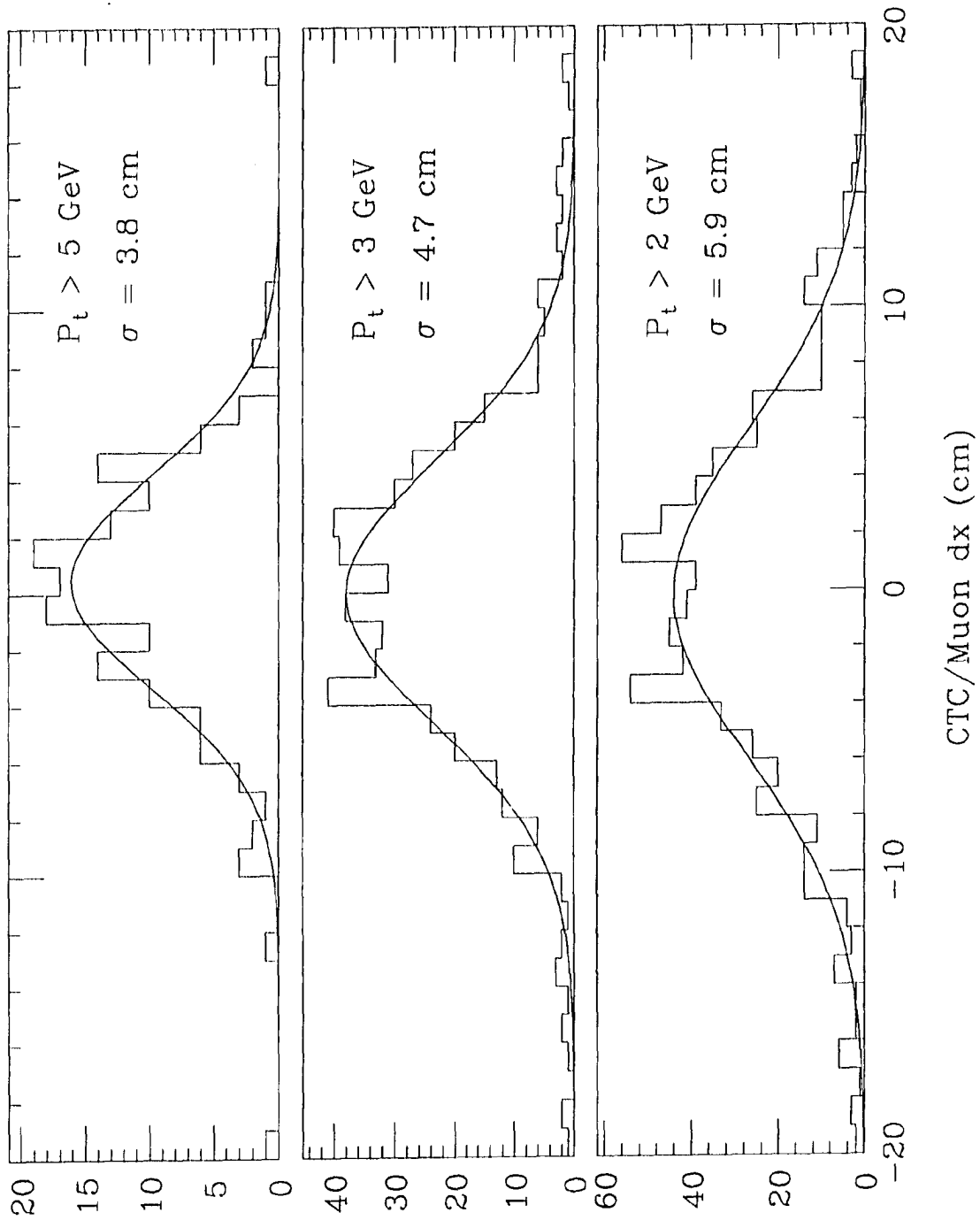


Figure 3.2: dx distributions after dz and minimum ionizing cuts, for different p_t thresholds.

Multiple Scattering

Multiple coulomb scattering of a charged particle passing through matter deflects the particle from its original trajectory. The distribution of deflection angles for a sample of tracks is roughly gaussian, with a projected width in a given plane given by

$$\theta_{m.s.} = \frac{0.0141 \text{ GeV}/c}{\sqrt{3} p} \sqrt{L/L_R} [1 + \frac{1}{9} \log_{10}(L/L_R)] \quad (3.1)$$

for an ultrarelativistic particle of unit charge. Here, p is the momentum in GeV/c and L/L_R is the number of radiation lengths of material traversed by the particle. Table 2.3 shows

$$L/L_R = 19 + 64/\sin \theta.$$

The logarithmic correction factor is 1.2, nearly independent of θ . Using $p = p_t \sin \theta$ and averaging over the θ coverage of the muon chambers (reasonable since all relevant particle distributions are flat in θ in this range),

$$\theta_{m.s.} = \frac{85 \text{ mR}}{p_t}. \quad (3.2)$$

The effective depth of the calorimeter is 181 cm, hence

$$dx_{m.s.} = \frac{15 \text{ cm}}{p_t}. \quad (3.3)$$

This agrees nicely with the $p_t > 3 \text{ GeV}/c$ plot in figure 3.2, but the other two plots differ somewhat. All three plots are consistent with

$$dx_{obs}^2 = \left(\frac{9.86}{p_t}\right)^2 + (3.5)^2$$

suggesting that some effect in addition to multiple scattering affects the distribution width. But to a first approximation the widths are consistent with multiple scattering, and the $dx = 8 \text{ cm}$ cut in table 3.1 corresponds to a 1.6σ cut at $p_t = 3 \text{ GeV}/c$ and becomes looser with increasing p_t .

Equation (3.3) gives a lower bound on the r.m.s. momentum resolution of the muon chambers. Considering the solenoidal magnetic field and the CTC geometry, the impact parameter of a muon at the chambers is (see figure 2.18)

$$b = \frac{50 \text{ cm}}{p_t}$$

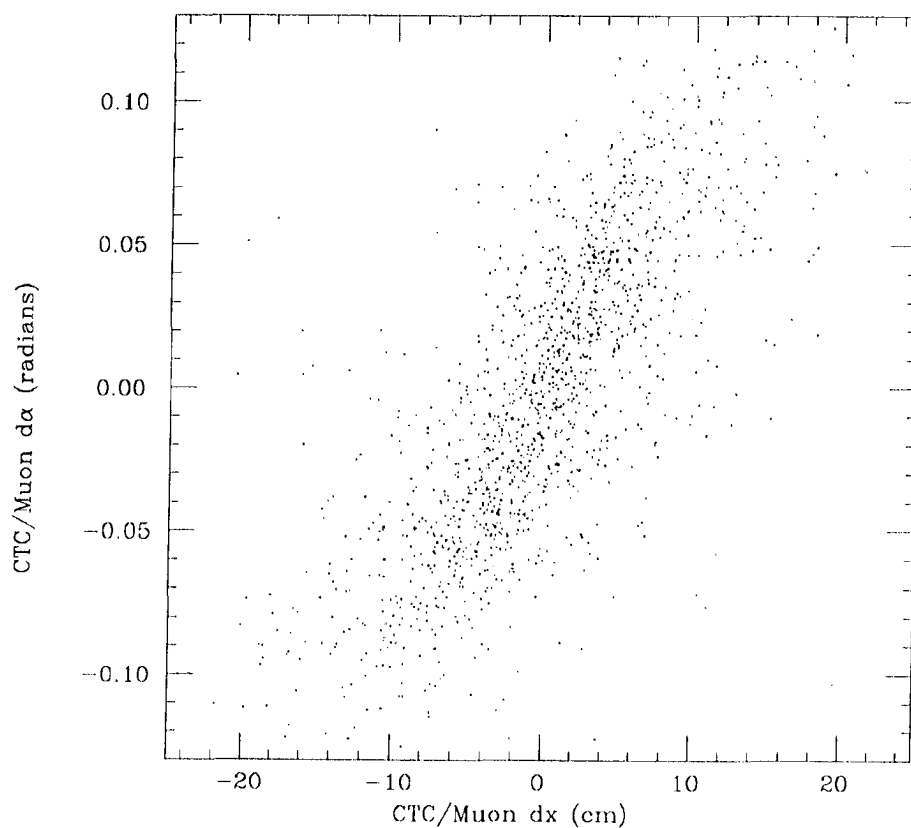


Figure 3.3: Correlation of the matching parameters $d\alpha$ and dx .

so that the angle is

$$\alpha = \frac{b}{R_{\text{cmu}}} = \frac{140 \text{ mR}}{p_t}$$

and

$$\frac{\Delta p}{p} = \frac{\theta_{\text{m.s.}}}{\alpha} > \frac{85/p_t}{140/p_t} = 60\%,$$

independent of the particle momentum. The inequality arises because the muon drift distance accuracy and the short lever arm of the muon chambers degrade the actual resolution (r.m.s.).

Matching cut values.

The other two matching parameters are dz and $d\alpha$. Figure 3.5 shows the dz distribution without any other cuts applied. The dz cut is looser (15 cm) than the dx cut because the z resolution of both the CTC and the muon chambers is less reliable.

Figure 3.3 shows that dx and $d\alpha$ are not independent variables. Figure 3.4 shows the $d\alpha$ distribution before and after the standard dx cut has been applied, for $p_t > 2 \text{ GeV}/c$. The cut looks a bit tight but from equation (3.2) and from studies of distributions $|d\alpha| < 60 \text{ mR}$ is reasonable.

A few words about the choice of the p_t cut: as will be shown, relative background contamination of the muon signal decreases with increasing p_t . Hence, the higher the cut, the better the quality of the data sample. However, the dN/dp_t spectrum is a decreasing power law, and a small increase in the p_t cut causes a large decrease in the total number of tracks. The choice $p_t > 3 \text{ GeV}/c$ is a compromise in order to leave enough of a data sample to work with. In a higher statistics analysis we would choose a higher p_t cut.

3.1.2 Minimum Ionization Cut

Most hadrons interact and deposit all their energy in the wedge. Figure 3.7 is a scatterplot of energy deposition in the hadron calorimeter versus deposition in the EM calorimeter for muon candidates. A clump of minimum ionizing particles is prominent in the lower left hand corner. These plots, as well as similar plots from the testbeam (see the appendix on noninteractive punchthrough) lead to the EM and Hadron cuts listed in table 3.1. These are loose cuts, but in the beauty sample the majority of the muons are within the jet core.

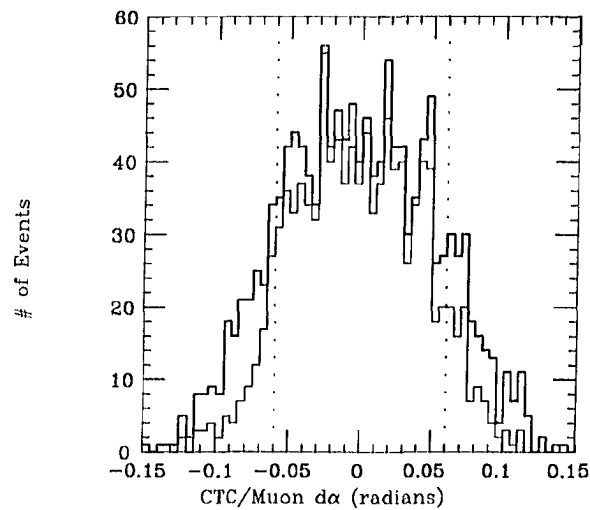


Figure 3.4: Raw $d\alpha$ distribution for muon candidates (bold) and after dx cuts (light). Vertical lines show the $d\alpha$ cuts.

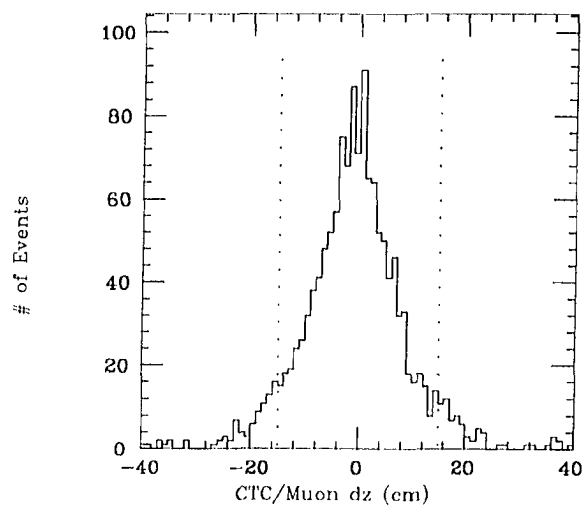


Figure 3.5: Raw dz distribution for muon candidates, showing cuts.

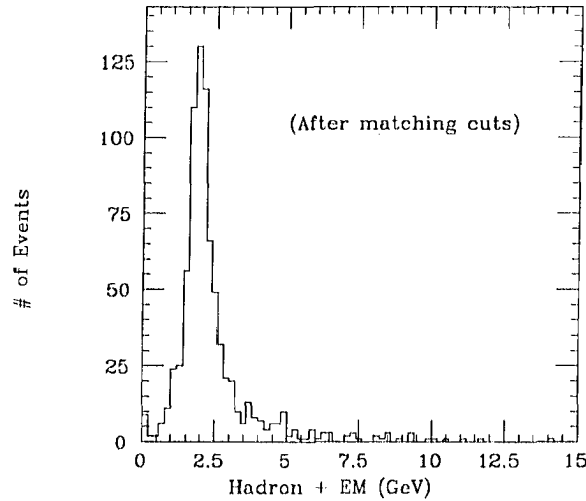


Figure 3.6: Sum of EM and Hadron energies for muons passing the matching cuts.

Hence, the energy from the minimum ionizing muon is usually overlaid by energy from particles in the jet, and the energy cut seriously decreases our acceptance.

3.1.3 Acceptance

The muon chambers inside a wedge subtend $\Delta\phi = 12.5^\circ$ as compared to the $\Delta\phi = 15^\circ$ for the entire wedge. The gap between the two arches at $\theta = 90^\circ$ is 15 cm, out of 480 cm total length of the chambers. Hence considering just the geometry of the muon chambers the acceptance is

$$\epsilon'_{geom.} = \frac{12.5^\circ}{15^\circ} \frac{465}{480} = 0.81$$

in the region $55^\circ < \theta < 125^\circ$.

The Main Ring noise discussed in chapter 2 forced us to reduce the anode voltage for the eight wedges with $60^\circ < \phi < 120^\circ$, decreasing but not annihilating their efficiency. Then $\epsilon'_{geom.}$ is decreased by a ‘Main Ring factor’,

$$1 > f_{MR} > \frac{48 - 8}{48} = 0.83.$$

Figure 3.8 gives a feel for f_{MR} , showing a ϕ distribution for CTC/muon matches from the $(jet \cdot \mu)$ data. The depressed region at $60^\circ < \phi < 120^\circ$ has $(40 \pm 10)\%$ of the occupancy of the rest of the distribution. Hence we estimate

$$f_{MR} = 1 - (0.4 \pm 0.1) \frac{8}{48} = 0.93 \pm 0.1,$$

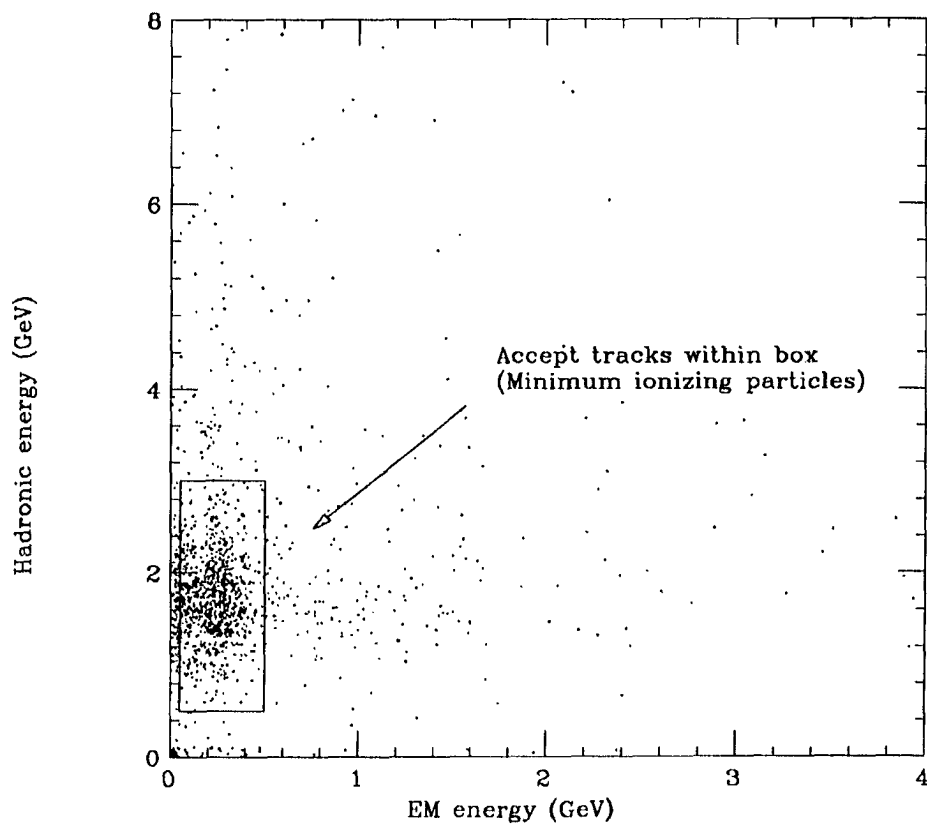


Figure 3.7: Hadron vs. EM energy for CTC/Muon matches after the dx , dz and $d\alpha$ cuts.

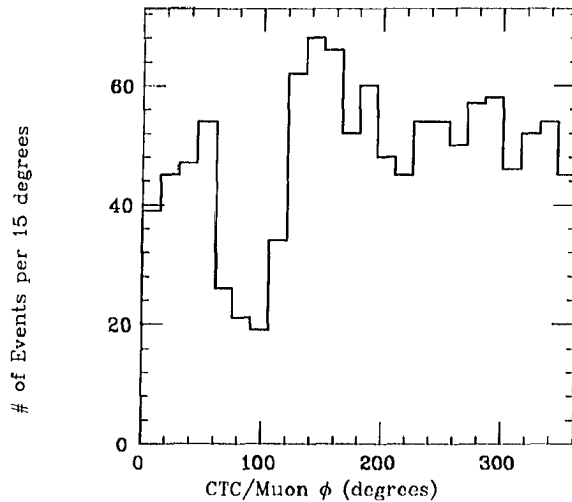


Figure 3.8: Azimuth angle distribution of muon-candidates, showing inefficiency due to Main Ring background.

and therefore

$$\epsilon_{geom} = (f_{MR})(\epsilon'_{geom}) = (0.93 \pm 0.1)(0.81) = 0.76 \pm 0.08 \quad (3.4)$$

3.2 Fake Muons

Leptons from $p\bar{p}$ collisions with $p_t > 3$ GeV/c are rare. Large numbers of charged particles are produced, but these are mainly pions, kaons, and protons. This means that any process whereby a small fraction of the hadrons fakes a muon signal will result in a significant background. The challenge in a muon analysis is to understand and compensate for these background processes.

Section 1.3.3 contains a list of the different background sources. The contribution of each source to the total background is estimated in the following subsections.

3.2.1 Noninteractive Punchthrough and Decay-in-Flight

Detailed calculations of the noninteractive punchthrough and decay-in-flight probabilities are given in the appendices. Given the momentum distribution for all charged tracks in the data, and knowing how many pions, kaons, etc are in the charged track spectrum, the probability curves yield the background rates.

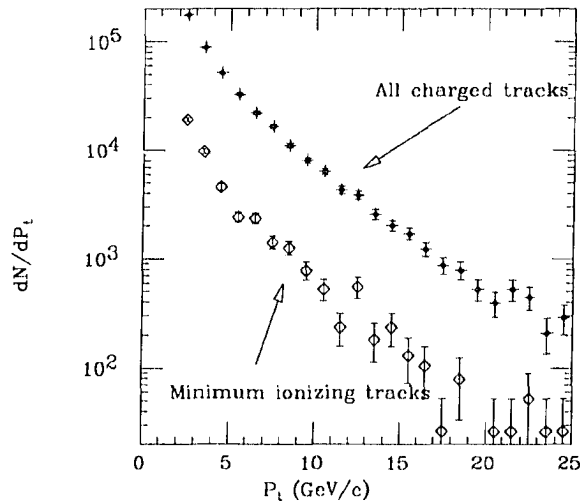


Figure 3.9: p_t distribution for all charged tracks from the jet data, scaled to the geometric acceptance of the muon chambers.

Parent Spectra

The $(jet\cdot\mu)$ data used in the beauty search is a subset of all the jet data acquired by CDF in the 1987 run. (The next chapter describes the jet finding algorithm.) Charged hadrons in events with a jet can produce fake muons, and the p_t distribution for these fake muons depends directly on the distribution for all charged tracks (see equation (C.4)).

To obtain the parent p_t distribution, we reconstruct some of the jet data using the same code as for the muon reconstruction, except that we do not require a muon stub. CTC tracks are extrapolated into the calorimeter exactly as for muon candidates, and the energy deposition along the track path is calculated. Requiring pseudorapidity $|\eta| < 0.65$ gives the same acceptance for the CTC tracks as for muon candidates. The resulting p_t distribution is scaled to the total integrated luminosity of the $(jet\cdot\mu)$ data sample, and corrected for the geometric acceptance ϵ_{geom} (preceding section). Figure 3.9 shows the result for minimum ionizing tracks and for all tracks, where a minimum ionizing track is one that passes the energy cuts in table 2.6. Note that the errors shown are statistical only: the error in the integrated luminosity will distort the difference between background calculation and the muon candidates, discussed in the next chapter.

The shape of the parent dN/dp_t distribution in figure 3.9 determines the shape of the expected background. Figure 3.10 shows that higher E_t jets tend to have higher p_t tracks, reflected in the stiffening of the distributions as the minimum jet E_t of the events is

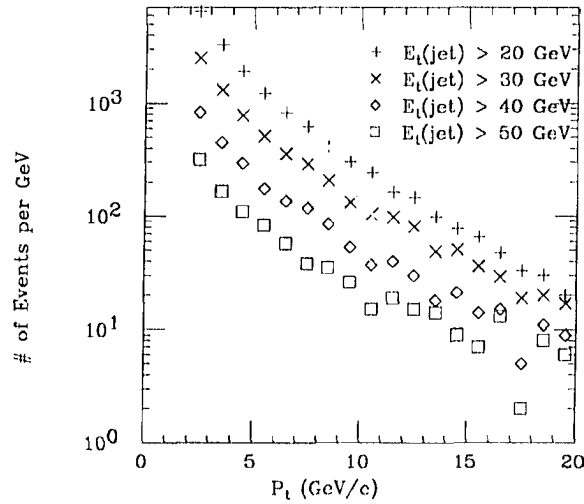


Figure 3.10: Charged track transverse momenta for events with a jet above different transverse energy thresholds.

raised. In the same way, the shape of the parent spectrum is expected to be sensitive to the trigger $\sum E_t$ threshold, since figure 2.22 showed that the efficiency for different jet energies varies with the $\sum E_t$ threshold. The beauty data comes from a mix of four $\sum E_t$ triggers, requiring a 20 GeV jet in the analysis, but the parent dN/dp_t spectrum of figure 3.9 comes solely from $\sum E_t = 30$ GeV trigger. This introduces some error in comparing background calculations based on figure 3.9 with data from the full beauty sample. However, table 1.3 shows that 72% of the data came from the $\sum E_t = 30$ threshold, and since the variation in the curves of figure 3.10 is moderate, the error is smaller than other systematic effects.

K/π Ratios

A major systematic error in calculating the muon background is the kaon content of the parent charged particle spectrum. The appendix on noninteractive punchthrough shows that the small absorption cross section for positive kaons means that more than 1 in 70 K^+ 's with $p_t < 10$ GeV/c will mimic a muon, as compared to less than 1 in 300 for pions.

Three sets of measurements allow us to estimate the ratio of the number of charged kaons in the data sample to the number of pions,

$$\frac{K}{\pi} \equiv \frac{\# \text{ of charged kaons}}{\# \text{ of charged pions}}.$$

Values are listed in table 3.2. The values come from time-of-flight measurements at the

<i>Source</i>	K/π value
Conservative ISR extrapolation	0.10
Reasonable value	0.25
Generous UA5 interpretation	0.35

Table 3.2: Fraction of heavy particles in charged track spectrum.

CERN ISR and UA5 experiments, and from a search for secondary vertices in the CDF CTC [27]. Both methods are unreliable for $p_t > 2\text{--}4$ GeV/c, and table 3.2 shows that the values vary significantly. The UA1 collaboration used the value of $\frac{K}{\pi} = 0.36$ in their muon analyses, but since they have 9 absorption lengths they are less sensitive to noninteractive punchthrough, and with their higher p_t cut the decay-in-flight contamination is less. Hence UA1 is less sensitive to the choice of $\frac{K}{\pi}$.

Protons and antiprotons amongst the charged tracks affect the background rates. The references [27] show that they are as abundant as the kaons,

$$\frac{K}{\pi} \approx \frac{p + \bar{p}}{\pi}.$$

For $p_t > 5$ GeV/c the p and \bar{p} contributions reduce the overall noninteractive punchthrough rate, since their absorption cross sections are larger than for pions. For $p_t < 5$ GeV/c, the proton absorption cross section is smaller than for pions, and is much smaller than for antiprotons. Hence the p 's contribute to the charge asymmetry discussed in the background appendices.

The charge asymmetry suggests a provocative prospect: perhaps the observed charge asymmetry amongst the muon candidates could lead to a measurement of $\frac{K}{\pi}$ at higher p_t , or at least to an extension of the measurement using the secondary vertices. Systematic uncertainties would make the analysis difficult, but since it is a useful measurement that has never been made, it would be worth some trouble.

Background Spectra

Figures 3.11 and 3.12 show the expected rates for fake muons from decay-in-flight and noninteractive punchthrough, using the results of the appendices and the parent charged track spectrum of figure 3.9. The error bars on the noninteractive punchthrough curves

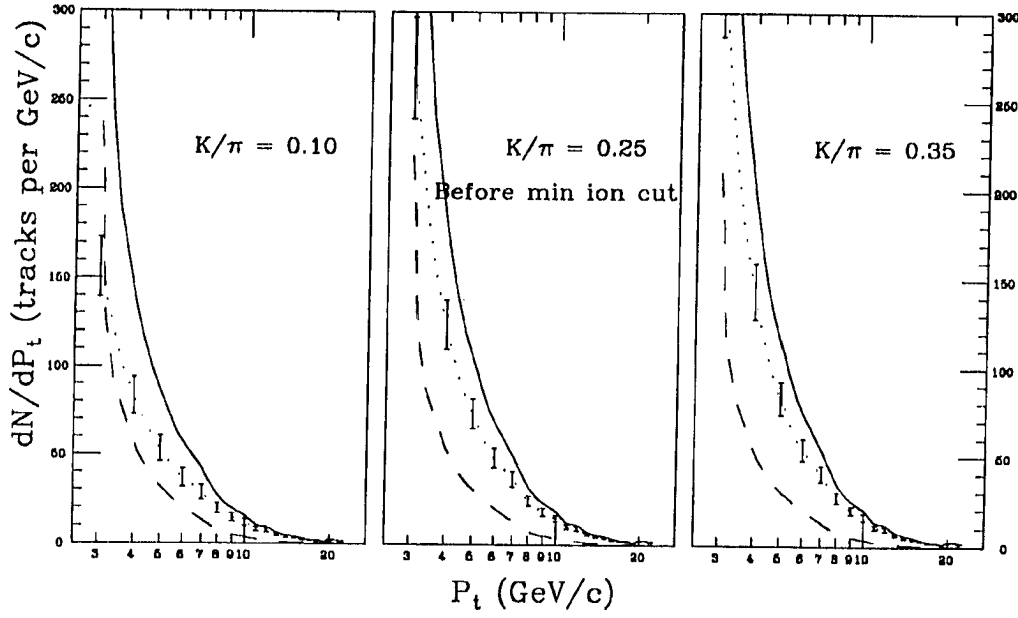


Figure 3.11: Muon background for different K/π ratios. Dashed line is the decay-in-flight contribution, dotted line shows noninteractive punchthrough with typical error bars due to the uncertainty in the absorption cross sections, and solid line is the sum of the two.

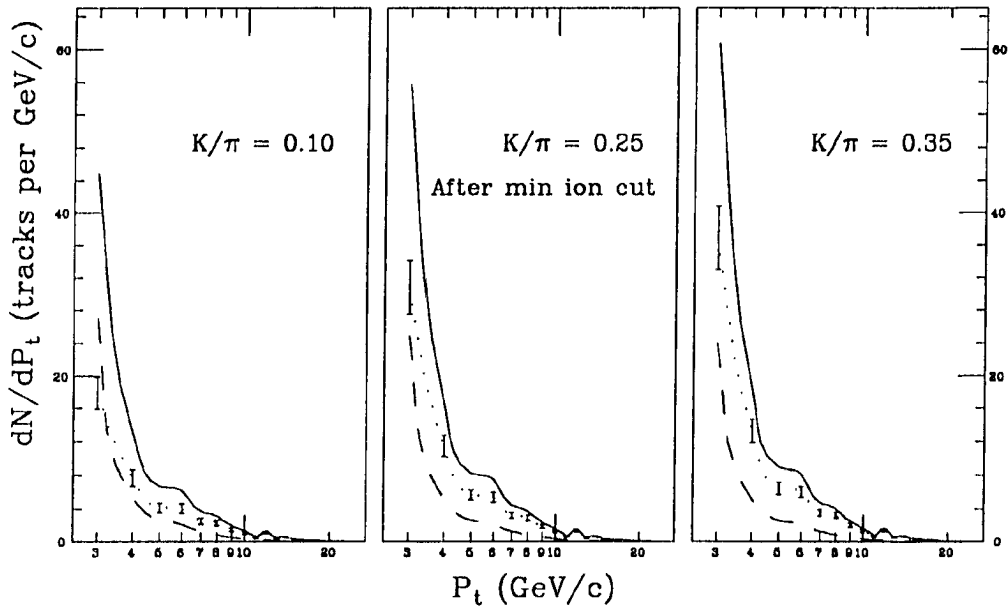


Figure 3.12: Same as preceding figure, except that the minimum ionization cut has been applied to the parent tracks.

correspond to a 4% error in the absorption lengths. The decay-in-flight contribution is approximately independent of the $\frac{K}{\pi}$ mixture, reflecting the fact that the acceptances for muons from K decay and from π decay are about the same. However, the noninteractive component increases with increasing $\frac{K}{\pi}$, raising the overall background rate. This is due to the small absorption cross section for K^+ 's. The next chapter compares the observed muon data with the expected background and expected signal of chapter 1.

Error Estimate

Uncertainties in the background calculation arise from different sources:

1. Statistical fluctuations in the parent charged track spectrum used to calculate the backgrounds;
2. Statistical fluctuations in the number of simulated decays-in-flight;
3. Wrong p_t dependence of the dN/dp_t distribution of figure 3.9, due to the mix of $\sum E_t$ triggers;
4. We assume that the pions, kaons, and protons all have the same dN/dp_t as the total charged track spectrum, which may be false;
5. Faulty decay-in-flight simulation. For example, CTC track reconstruction may handle tracks in busy jet environments differently than the isolated tracks we simulated, or CTC noise simulation could be inadequate;
6. Error in the choice of $\frac{K}{\pi}$;
7. Uncertainty in the absorption lengths.

The first two give errors of less than a few percent, since we had large statistics for both studies. Similarly, figure 3.10 and table 1.3 indicate that point (3) is not a big problem. The next point is intractable: considering that we don't know how many kaons there are, we certainly don't know their momenta. But to the extent that the individual momentum distributions are similar to the total distribution, the contribution to the error is small. 'Small' is in comparison to the last two items on the list, which we turn to now.

In figure 3.13, the sum

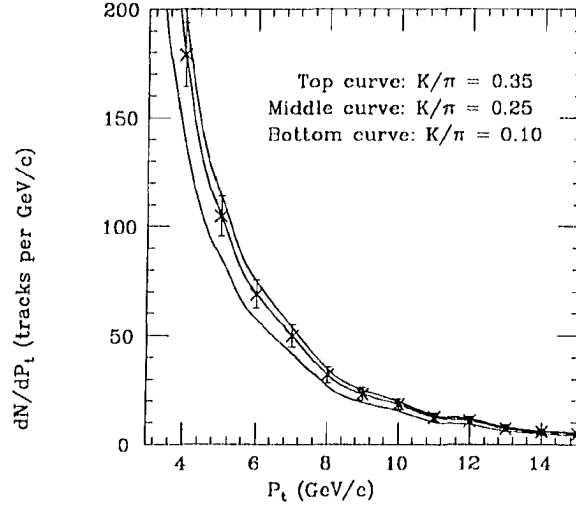


Figure 3.13: Total background (decay + noninteractive) for different K/π , comparing magnitude of uncertainty due to K/π error with uncertainty from absorption length error.

$$\text{sum} = (\text{decay-in-flight}) + (\text{noninteractive punchthrough})$$

from each of the three plots in figure 3.11 (solid curves) is superimposed onto a single plot. This shows the spread in the background estimate that comes from varying $\frac{K}{\pi}$. The error bars on the middle curve are based on a 4% error in the number of absorption lengths, $\delta\Lambda$, traversed by a muon candidate and are about 20%. The errors from $\frac{K}{\pi}$ and $\delta\Lambda$ are about the same magnitude. The errors are uncorrelated and therefore can be added in quadrature, which in this case is the same as multiplying the error from $\delta\Lambda$ by $\sqrt{2}$. Considering the lengthy list above, this is probably an underestimate of the error: instead we will use

$$\delta N_{bgd} = 2\delta\Lambda N_{bgd}$$

where N_{bgd} is the number of entries in a given bin of the background momentum distribution. We use $\delta\Lambda = 0.04\Lambda$ where Λ is calculated according to the appendix on noninteractive punchthrough.

θ Dependence of Noninteractive Punchthrough

The number of absorption lengths traversed by a muon candidate is $\Lambda = \Lambda_0 / \sin \theta$, where Λ_0 is for a track 90° from the beam axis. Therefore we expect fewer noninteractive punchthroughs at small θ . A sample of muon candidates will be a mixture of punchthrough and of muons, which have no θ dependence (for either decay muons or prompt muons).

The observed θ variation gives an independent measure of the fraction of noninteractive punchthrough in the data sample. A preliminary search for this effect in the data showed agreement with calculations, and we expect to use this handle in the future.

3.2.2 Other Sources

Interactive Punchthrough

Hadrons interact in the steel of the wedges and generate a shower of particles. Usually all the secondary particles are absorbed, but sometimes one or a few will leak to the muon chambers. An accidental match between a resultant stub and a track in the CTC produces a muon candidate, hence shower leakage is a background source that must be considered.

The interactive punchthrough probability for the wedges was measured in a pion test beam [1]. The probability \mathcal{P} increases linearly with pion energy E_π ,

$$\mathcal{P} \approx (0.011)E_\pi - (0.04) \quad (10 < E_\pi < 40\text{GeV}). \quad (3.5)$$

Below 10 GeV, a power law gives a better approximation,

$$\mathcal{P} \approx (0.13)E_\pi^{1.62}e^{-l/\lambda} \quad (3 < E_\pi < 10\text{GeV}),$$

with $l = 100$ cm as the equivalent depth of steel in a calorimeter wedge and $\lambda = 23$ cm [26]. Testbeam ‘punchthrough’ means that at least 2 hits were recorded in the muon chambers. How does this relate to the probability of detecting a fake muon from shower leakage? In $p\bar{p}$ data, muon candidates must have more than 2 hits, and must match with a CTC track, decreasing the number of leakage particles contributing to the muon background. Also, equation (3.5) is for pions, whereas collision data includes kaons which may have different punchthrough probability. Neutral hadrons may also contribute to the leakage rate, and their p_t spectrum is unmeasured. Since a jet is a cluster of particles of different momenta and species, calculating the interactive punchthrough contribution to the muon-candidate rate in jet events is very delicate, and a monte carlo would have to include detailed modeling of hadronic showers. The rate is not calculated in this thesis.

Rather, we rely on the minimum ionizing cut to reject fake muons from shower leakage. When data is compared with the calculated backgrounds in the next chapter, events without a minimum ionizing cut show an excess of muon candidates above the background

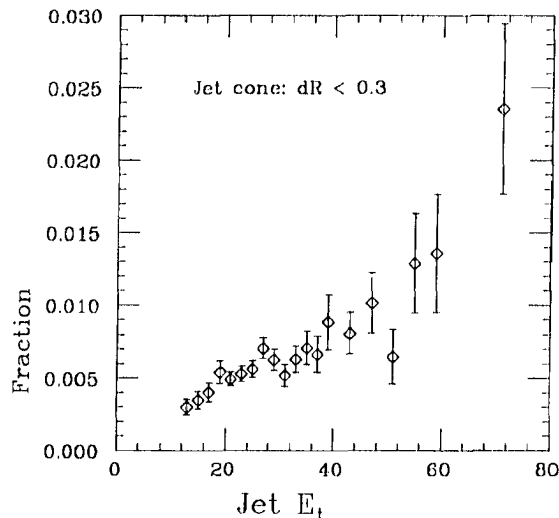


Figure 3.14: Fraction of jets with an associated CTC/stub match.

from non-interactive punchthrough and decay-in-flight. After the energy cut, the large excess vanishes.

While the minimum ionization cut is effective at rejecting shower leakage, it also rejects prompt muons that overlap a jet: this is the bulk of the beauty signal. Work is in progress to develop ways to identify prompt muons in jets.

Having explained the difficulties in calculating the interactive punchthrough probability, it is interesting nonetheless to see what we can learn from looking at the data. In the p_t^{rel} analysis of the next chapter, muon-candidates are ‘matched’ with the nearest jet. Histogramming the E_t ’s of the matched jets, and normalizing to the dN/dE_t distribution for all jets gives figure 3.14, which therefore shows the probability of finding a muon-candidate in a jet of transverse energy E_t . No minimum ionizing cut has been applied to the muon candidates, the only criterion for candidacy being a ‘tight’ match between the muon stub and the CTC track. Also, the muons are required to fall inside a cone of $dR = \sqrt{\Delta\eta^2 + \Delta\phi^2} < 0.3$. ($\Delta\eta, \Delta\phi$ are the differences between the jet axis and the muon track.) Expanding the cone size to 0.7 increases the probability by about the size of an error bar in figure 3.14. About 1% of 50 GeV jets will contain a muon-candidate, before making a minimum ionizing cut.

Cosmic Rays

Cosmic rays incident on CDF make stubs in the muon chambers at a rate of about 1000 per second. For a cosmic ray to accidentally overlap a $p\bar{p}$ bunch crossing, it must fall within the RUN/STOP window of 700 nS described in chapter 2. Hence the fraction of events containing an accidental muon stub is

$$\text{cosmic accidents} < (700 \text{ nS})(1 \text{ kHz}) = 7 \times 10^{-4}.$$

This low probability is an upper bound on the contamination of the muon data: the CTC timing window is shorter than 700 nS, and a muon candidate requires that a CTC track passed within 0.5 cm of the event vertex. Also, the beauty sample requires at least one 20 GeV E_t jet, further reducing the overlap probability. Hence, contamination of the muon data by cosmic rays occurs at a very low rate.

Cosmic ray events are easily distinguishable from $p\bar{p}$ collisions. An air shower depositing more than a few GeV will fire TDC's in the hadron calorimeter. The pattern reconstruction software rejects events where some fraction of the hadron energy is outside of a 60 nS timing window ¹. Also, tracks traversing the entire detector are discernible by eye, and can be rejected in hand-scanning. We neglect cosmic rays in the data analysis.

¹The module making the cut is called HATFLT

Chapter 4

Data Analysis

4.1 Event Selection

4.1.1 Data Samples

Of the 33 nb^{-1} of data recorded by the CDF detector in 1987, 24.7 nb^{-1} was taken with the triggers listed in table 1.3. The raw data is stored on about 400 magnetic tapes. Requiring the beauty event topology reduced the number to about a half-dozen tapes. The beauty signature is a muon associated with a jet, hence the steps to skim the events of interest from the full data set were

1. Keep every event with a muon candidate with $p_t > 2 \text{ GeV}/c$;
2. Keep only events with a 20 GeV central jet;
3. Keep only events that satisfied the $\sum E_t$ trigger.

With hindsight, the reverse order of steps seems more efficient. But with a new detector our first step had to be to explore all of the muon data, and only after that could we confine ourselves to a specific signature.

Background calculations require a sample of jet events unbiased by muon selection. Hence, beginning with raw data we made a second data set using only steps (2) and (3). This set is called the ‘generic jet’ data, the other set being the $jet \cdot \mu$ sample.

4.1.2 Jet Algorithm

A jet is a collimated group of particles emanating from the collision vertex. Jets are understood to be produced by hard-scattered partons that create mesons from the vacuum.

Empirically, the average number of tracks with $p_t > 0.4$ GeV/c within a cone of radius

$$\Delta R \equiv \sqrt{\Delta\eta^2 + \Delta\phi^2} = 0.7$$

increases logarithmically, and is about 7 for $E_t^{jet} = 30$ GeV, or

$$\langle N \rangle = 4.5 \log(0.15 E_t^{jet}).$$

In the detector, a jet appears as narrow spray of tracks in the CTC, and as a cluster of calorimeter towers with large energy depositions. Jets discussed in this thesis are all calorimeter jets, and the algorithm used to recognize the energy clusters is crucial. In particular, an algorithm must

- Efficiently recognize all clusters. Some jets are less collimated than others, so distinguishing a single broad jet from two smaller jets can be difficult;
- Measure the jet energy correctly: calorimeter towers on the edge of a cluster can contribute uncertainties, and corrections for detector gaps, etc, must be made;
- Measure the jet size: in the expression for ΔR (above) the parameters $\Delta\eta$ and $\Delta\phi$ have finer resolution than the tower size if one uses tracking information and the relative pulse heights of the two phototubes in each tower;
- Measure the jet direction: a weighted sum of the energies in the cluster towers is used. Accurate direction measurement is important for the p_t^{rel} studies.

The algorithm used by CDF is a cone-based algorithm called JETCLU. It searches for the tower with the greatest pulse height, calculates a cone of fixed size about the tower, sums towers above some threshold, and then refines the resulting measurements in an iterative process. The reliability of JETCLU and competing algorithms has been studied in detail [29].

4.2 Prompt Muons

After reconstructing the muons and the jets and applying all the cuts, we are left with a sample of muon candidates. Figure 4.1 compares the $\frac{dN}{dp_t}$ of the muon candidates with the decay-in-flight and noninteractive punchthrough backgrounds calculated in the last

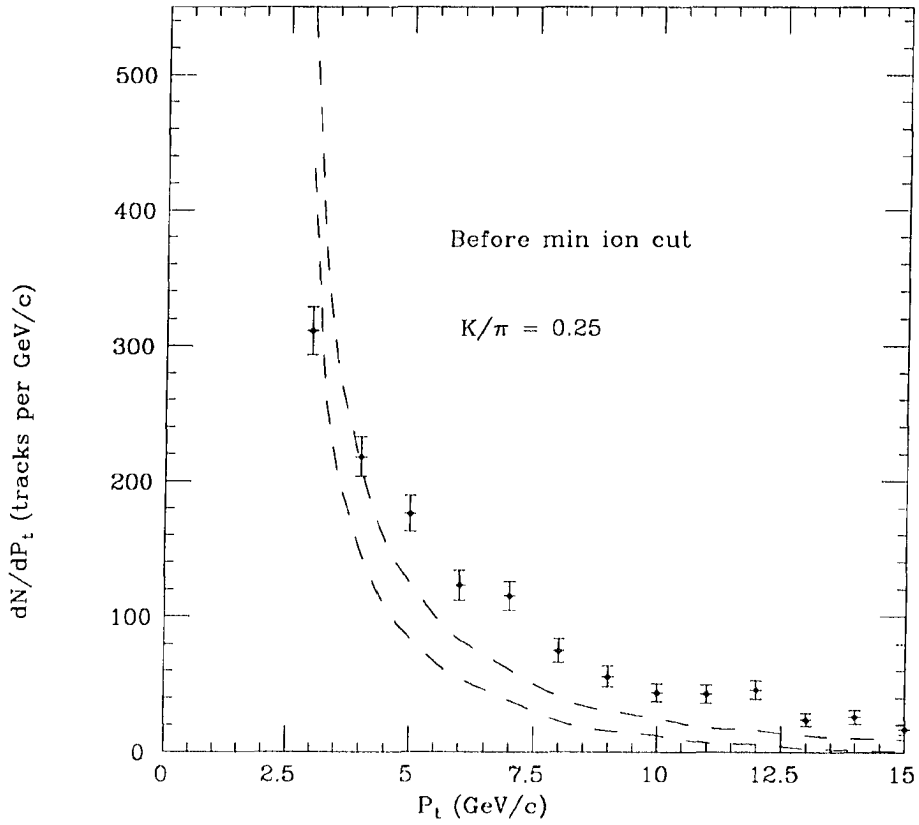


Figure 4.1: Momentum distribution of muon candidates from the $jet \cdot \mu$ data, before the minimum ionizing cut. Region within the dashed lines is the expected background from decay-in-flight and noninteractive punchthrough.

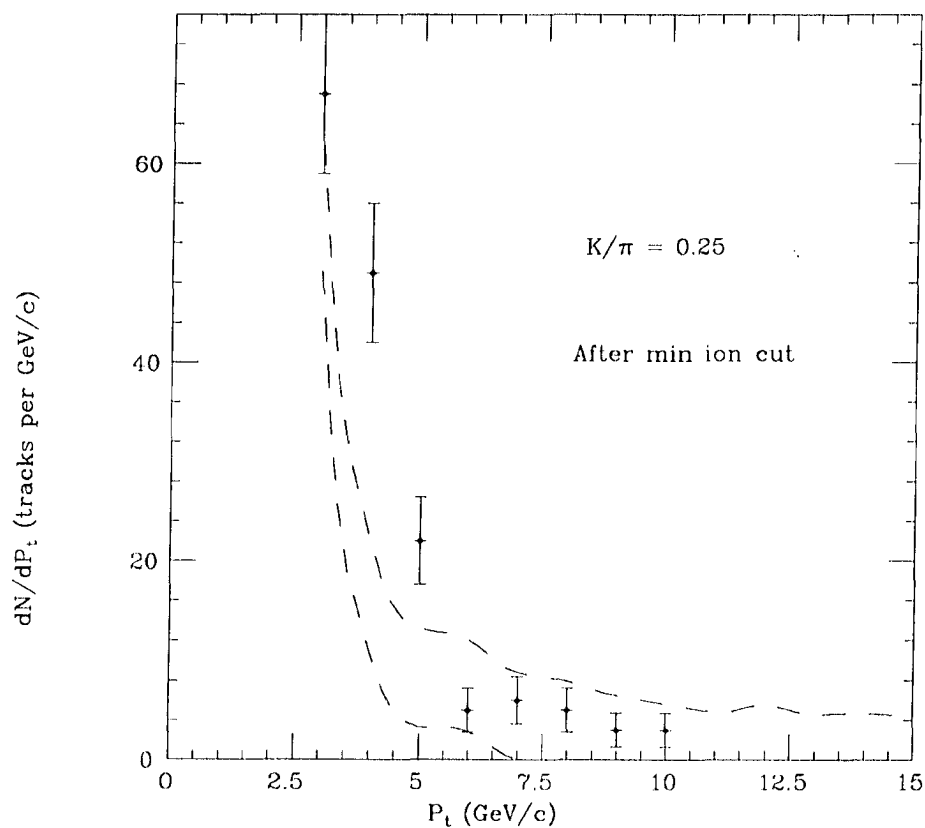


Figure 4.2: Momentum distribution of muon candidates from the $jet \cdot \mu$ data, after the minimum ionizing cut. Region within the dashed lines is the expected background from decay-in-flight and noninteractive punchthrough.

$p_t(\text{GeV}/c)$	Candidates	Background	Difference
3-4	67 ± 8.0	55.6 ± 8.9	11.4 ± 12.0
4-5	49 ± 7.0	16.6 ± 7.0	32.4 ± 9.9
5-6	22 ± 4.4	8.3 ± 5.8	13.7 ± 7.3
> 6			0
<i>Total</i>	138 ± 11.5	80.5 ± 12.7	57.5 ± 17.1

Table 4.1: Muon candidates and background subtraction.

chapter. The dashed curves correspond to one standard deviation above and below the curves obtained using $\frac{K}{\pi} = 0.25$. For $p_t > 5 \text{ GeV}/c$ the number of muon candidates exceeds the expected background, but hand-scans of individual events show that these events are consistent with interactive punchthrough (shower leakage). The excess disappears after applying the minimum ionizing requirement on the muon candidates, as shown in figure 4.2. Here, the number of muon candidates with $p_t > 5 \text{ GeV}/c$ is completely consistent with the expected background, suggesting that most of the B signature has been lost with the various cuts. However, there is a small excess of muon candidates in the three lowest p_t bins. Table 4.1 gives the number of prompt muons obtained by background subtraction. Equation (1.5) predicted 425 muons from this analysis, before the minimum ionizing cut. It is difficult to compare this figure with the total in table 4.1, but

$$57.5 \pm 17.1 < 425$$

is consistent with having lost most of the muons with the minimum ionizing cut, since the muons are expected to overlap with the jet.

4.3 Momentum Transverse to the Jet Axis, p_t^{rel}

In equation (1.6) and figure 1.5 the component of track momentum perpendicular to the jet axis was described as

$$p_t^{rel} = p \sqrt{\tanh^2(\Delta\eta) + \sin^2(\Delta\phi)}$$

where p is the total track momentum, and $\Delta\eta$ and $\Delta\phi$ are the differences in the pseudo-rapidity and azimuth angle, respectively, between the track and the jet axis. Due to the

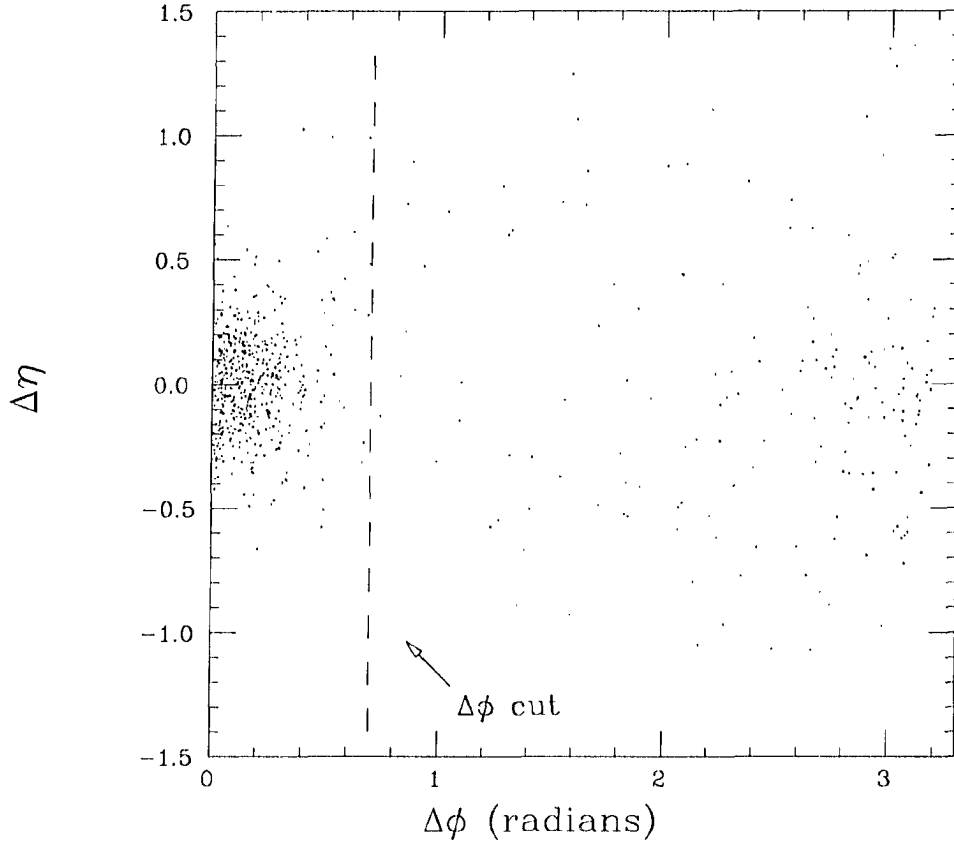


Figure 4.3: Differences in pseudorapidity and azimuth angle between matched jets and muons, showing the $\Delta\phi$ cut.

harder fragmentation of the more massive B meson (compared to mesons made of lighter quarks), we expect muons from B decay to have higher values of p_t^{rel} .

To observe this effect, we reconstruct jets in the $jet \cdot \mu$ data sample, and then find the jet closest to each muon candidate. Figure 4.3 is a scatter plot of the $\Delta\eta$ and $\Delta\phi$ of the jet-muon matches. For the most part, the points at large $\Delta\phi$ correspond to mismatches: jets must have $E_t > 12$ GeV and $|\eta_{jet}| < 0.9$, so that if a muon is near a softer jet, it will be misassociated with a jet farther away. A requirement that

$$|\Delta\phi| < 0.7 \text{ radians}$$

for jet-muon matches rejects most mismatches.

The p_t^{rel} distributions for the muon candidates are shown in figures 4.4 and 4.5, with and without the requirement of energy deposition along the track path consistent with

minimum ionization. Superimposed are the distributions for all charged tracks from the generic jet data sample. Without the energy cut, the muon curve tracks the background curve fairly faithfully. An apparent excess in the calculated background is consistent with the p_t distribution in figure 4.1, where we expected more muon candidates in the lowest bin. The muon candidates in figure 4.4 are dominated by background.

The picture changes in figure 4.5. Consider the muon distribution in two pieces: $p_t^{rel} < 1.7$ GeV/c and $p_t^{rel} > 1.7$ GeV/c. The $p_t^{rel} < 1.7$ GeV/c section agrees qualitatively with the predictions of chapter 1. That is, the muon curve peaks at about 0.9 GeV/c, and is stiffer than the background curve. Combined with the muon excess of figure 4.2 and table 4.1, we conclude that there are muons from B decay in our data sample.

For $p_t^{rel} > 1.7$ GeV/c, the muon excess seems excessive. A hand-scan of these events reveals different contributors to the large tail. About a third could be removed by tightening the $\Delta\eta, \Delta\phi$ cuts in figure 4.3. Another third could be either kinked tracks where the CTC track reconstruction assigned too high of a p_t value, or tracks which were very close to an energy cluster and may have erroneously passed the minimum ionization cut. But at least a third of the high- p_t^{rel} events look good: a clean, isolated muon well separated from the nearest jet, occurring at a larger rate than can be accounted for by the technical backgrounds.

An example is event 7438/281. Here, the nearest calorimeter cluster to the 4 GeV/c μ^+ appears to be a clean 14 GeV/c electron, back-to-back with a broad 16 GeV jet and negligible missing energy. This event suggests the process

$$p\bar{p} \rightarrow B\bar{B}, \quad \bar{B} \rightarrow \mu^+ D \nu_\mu, \quad D \rightarrow e^- K \bar{\nu}_e.$$

When higher statistics are available, distributions made with these sorts of events will yield exciting new physics measurements.

Background

A p_t^{rel} distribution for muons from beauty decay should peak at higher values than the corresponding curve for charm decay. In turn, both should be stiffer than a plot for ‘generic’ pions and kaons within the jets. Figures 4.4 and 4.5 compare the distributions for muon candidates with those for all charged tracks.

But one has to be careful: since p_t^{rel} is a product of the track momentum and

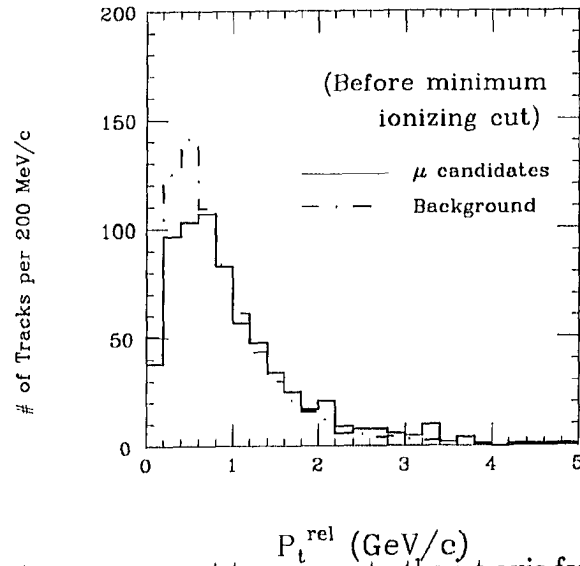


Figure 4.4: Momentum component transverse to the jet axis for muon candidates and for background tracks, before the minimum ionization cut.

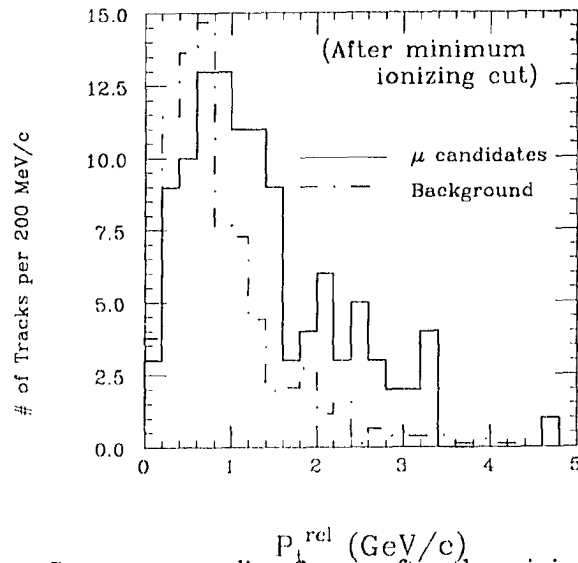


Figure 4.5: Same as preceding figure, after the minimum ionizing cut.

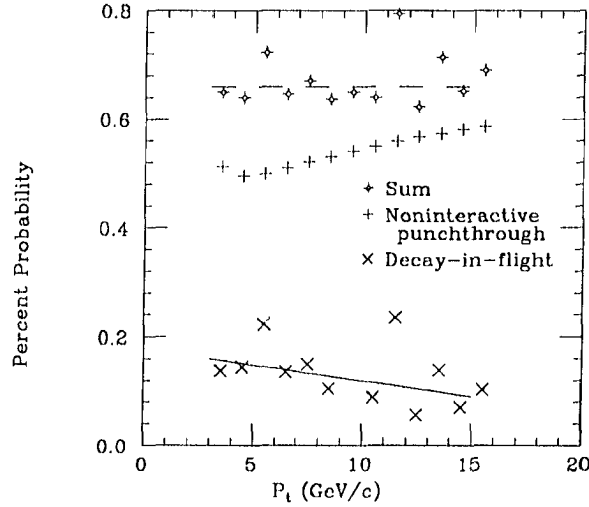


Figure 4.6: Probability, in percent, for a charged track to appear as a muon candidate. Lines are to guide the eye.

the distance in (η, ϕ) space from the jet axis, then generic tracks having the same spatial distribution (relative to the jet axis) as muon-candidates would have a different p_t^{rel} distribution, so long as the momentum spectra were different. That is, one could argue that a difference in shapes between ‘signal’ and background in figures 4.4 and 4.5 arises simply because decay-in-flight tends to soften the momentum spectrum of muon candidates relative to their parent mesons. It turns out that this is not the case.

Figure 4.6 shows the probability per track for a charged hadron to create a muon-candidate, as a function of transverse momentum. In the range $3 < p_t < 15$ GeV/c, the noninteractive punchthrough probability for all hadrons rises steadily, dominated by the falling pion absorption cross section (see the appendix). A particle mix of $\frac{K}{\pi} = 0.25$ is used. Conversely, the meson decay probability decreases. The two effects happen to cancel, and the total probability for generating a fake muon is momentum independent. This means that we expect dN/dp_t for fake muons and all charged tracks to have the same shape, and any difference in the shapes of the p_t^{rel} distributions has to come from differences in the spatial distributions, presumably due to the harder fragmentation of heavy flavor decay.

Chapter 5

Conclusion

5.1 The Past

We have built a working muon detector and have developed the associated pattern recognition code. By studying beauty production in $p\bar{p}$ collisions at $\sqrt{s} = 1.8$ TeV and subsequent decay of the beauty mesons to muons we have learned how to distinguish muons from the large backgrounds present in these complex events. The number of muons observed in events having at least one central jet is consistent with QCD calculations for beauty and charm production. Muon backgrounds are largest in jet events, hence satisfactory treatment of this data sample promises more accurate muon measurement in other processes.

We have studied the relation between muon tracks and jets in the same event. Due to the large mass of the parent B meson, the decay muon is further from the jet than background tracks. Even with the low statistics, p_t^{rel} gives a powerful signature for heavy flavor production.

We have also looked for evidence of heavy flavors in a sample of dimuon events. In spite of trigger inefficiencies during the debugging of this new detector, we see a resonance in the invariant mass distribution for unlike-charge dimuon events at the J/Ψ mass. Events with dimuon pairs from J/Ψ decay have little associated energy deposition in the calorimeters. On the other hand, including events with more energy, we compare the number of unlike charge dimuon candidates with the number of like charge events and find an excess consistent with the semileptonic decay of pairs of charm or beauty mesons. Hence we confirm that we are sensitive to medium p_t muons in complex event topologies.

5.2 The Future

At the time of this writing, the CDF detector is collecting $p\bar{p}$ collision data hundreds of times faster than in the 1987 run. The 30 nb^{-1} 1987 data sample is being matched every 1-2 days, with far superior trigger efficiencies, and with greatly improved noise suppression. Two feet of steel installed between the Main Ring and the detector allow the top muon chambers to operate at nominal voltages. A dimuon trigger installed during the past year provides sensitivity to J/Ψ and Υ production. The Tevatron is performing twice as well as the most optimistic pre-run forecasts predicted. Current projections are that we will accumulate between 1000 and 5000 nb^{-1} before the end of the run, or at least 300 times more data than was available for this dissertation, and of higher quality.

The two theses using the 1987 muon data represent completion of the biggest chores on the path to studying new muon physics at CDF [2]. Hardware installation, code development, and the main background calculations are done. Our tools are in place and new data is pouring in.

The most obvious next goal is discovery of the Top quark in the muon channel. Of the different decay modes (jets; jets and leptons; leptons) the muon channel has marked advantages: the backgrounds are large, but those for jets and electrons are probably worse. The muon system will refine measurements of established physics, such as the cross sections for beauty and charm production, Drell-Yan processes, beauty oscillations, and so forth. Perhaps an extension of the $\frac{K}{\pi}$ ratio in the charged track spectrum to higher p_t is possible. But most exciting in a new energy domain is to discover new, unexpected phenomena. If Nature holds heavy W^{**} 's and Z^{**} 's for CDF, or if the Higgs particle is within reach, or if some completely new twist awaits, then the muon system will find it. Or, muons in conjunction with jets or electrons will reveal it. A universe of possibilities awaits.

Appendix A

Coordinate Systems

A.1 CDF Global Coordinates

Figure A.1 shows the CDF detector and the CDF coordinate system. It is a standard right-handed spherical coordinate system, where protons travel towards larger z (east), the positive x -axis points to the exterior of the ring (north), and the positive y -axis points straight up. Hence the wedges and arches of the central calorimeters form segments in azimuth angle ϕ , and pseudorapidity η depends only on θ ,

$$\eta = \ln(\cot \frac{\theta}{2}).$$

A.2 Local Wedge Coordinates

Figure 2.8 shows a cross section of a muon chamber. Each wedge contains three such chambers, side-by-side. Both sides of the middle chamber are flat, like the right-hand side of the chamber in figure 2.8. The third chamber is a mirror image of the one shown.

In reconstructing the muon stubs it is natural to pick a set of rectangular axes (x, y) as shown in figure 2.8. The z -axis is the same as in global CDF coordinates (i.e., into the page in the figure). The origin is as follows:

- $x = 0$ is in the middle of the middle chamber (not shown in figure 2.8). Increasing x is in the positive ϕ direction;
- $y = 0$ is at the bottom plane (noted in figure). At $x = 0$ the y -axis and the radial direction are the same;
- $z = 0$ is at the $\theta = 90^\circ$ crack between the east and west wedges of figure A.1.

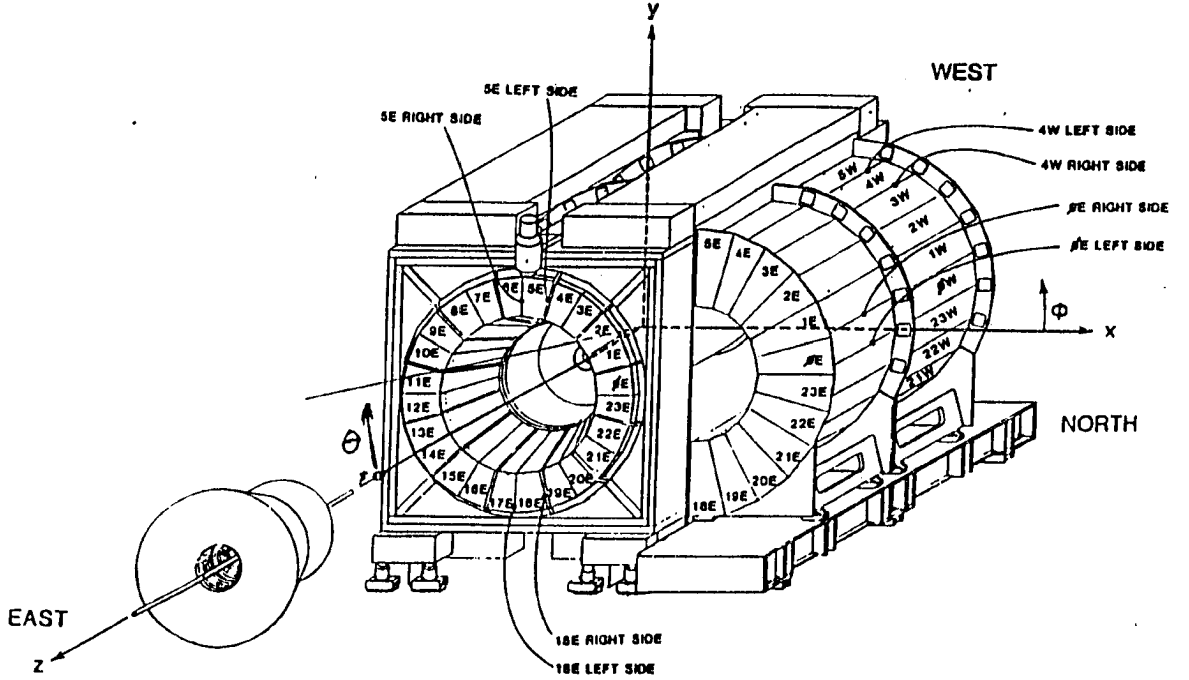


Figure A.1: The CDF coordinate system.

Each east-west wedge pair has its own local rectangular coordinates, rotated by $\phi = 15^\circ$ compared to adjacent wedges. To compare CTC tracks with muon stubs we transform the CTC tracks to the local wedge coordinate system as in equation 2.7 and calculate the track matching parameters as at the beginning of chapter 3.

Note that since wire pairs lie on radial centerlines from the $p\bar{p}$ vertex, they are at angles relative to the y -axis in local wedge coordinates.

Appendix B

Noninteractive Punchthrough Probability

The number of absorption lengths traversed by pions, kaons, protons, and antiprotons in a central wedge is calculated as a function of the incident hadron momentum. The momentum dependence is strong, resulting in 3 times as many non-interacting pions at low momentum as compared to high momentum. Fits and a fortran function are provided to ease calculations of backgrounds to muon signals. Corrections are made for the energy loss of the particle in the wedge. An overall punchthrough probability using the UA5 charged particle mix is shown. The fact that K^+ 's have a smaller absorption cross section than K^- 's leads us to the prediction of a charge asymmetry in the non-interactive hadron punchthrough background to the inclusive central muon spectrum ¹.

B.1 Motivation

Two principal backgrounds confuse a study of prompt muons in the CDF central region. These are muons from pion and kaon decay, and hadrons that don't shower in the calorimeter. This appendix concerns the latter category. A charged hadron leaves a minimum-ionizing trail in the calorimeter until it showers. If it never showers, it is indistinguishable from a muon. The probability \mathcal{P} for an incident hadron not to interact after traversing a distance x of material is

$$\mathcal{P} = e^{-\Lambda} = e^{-x/\lambda_{abs}} \quad (\text{B.1})$$

or 1/165 for $\Lambda = 5.10$. The absorption length λ_{abs} depends on the absorption cross section,

$$\lambda_{abs} = \frac{A}{N\rho\sigma_{abs}}, \quad (\text{B.2})$$

¹The contents of this appendix have appeared as a CDF internal memo [36].

Hadron	σ_0	α
K^+	20.37 ± 0.80	$0.791 \pm .01$
K^-	22.56 ± 0.90	$0.779 \pm .01$
π^+	25.64 ± 1.00	$0.764 \pm .01$
π^-	25.86 ± 1.00	$0.762 \pm .01$
p	37.99 ± 1.48	$0.719 \pm .01$
\bar{p}	43.50 ± 1.73	$0.698 \pm .01$

Table B.1: Parameters for the power-law fit to the A -dependence of the absorption cross-section for 60 GeV/c particles.

where A is the atomic number of the material, N is Avogadro's number, ρ is the density of the material, and σ_{abs} is the absorption cross section. Hence one need only know the depths and cross sections for the different materials in the calorimeter, and Λ comes from simple arithmetic.

The difficulty is in knowing the cross sections accurately. The Particle Data Booklet (PDB) only tabulates values for proton interactions in different materials at high energy, $E > 50$ GeV, and the PDB cross section curves are only for hadrons incident on proton targets. The cross section for hadrons on heavier targets obeys a power law,

$$\sigma_{abs} = \sigma_0 A^\alpha \quad (\text{B.3})$$

and simple scaling from the proton values to the pion values is complicated by the fact that α varies significantly amongst hadron species. Hence, the literature has to be probed beyond a cursory reference to the data booklet. Table B.1 shows how the power law for the inelastic cross section varies for different mesons [30].

One last motivating remark: a rough, 10% estimation of Λ based on naive scaling will result in a 50% error in the rate for non-interacting punch through's. That is, the error in the rate is

$$\frac{\delta \mathcal{P}}{\mathcal{P}} = \left(\frac{\delta \Lambda}{\Lambda}\right) \Lambda$$

and $0.1 \times 5.1 = 51\%$. A survey of the literature indicates that about 3% accuracy in Λ is obtainable, lowering the error in the rate to 15%. Hence a small improvement in the Λ calculation yields a big gain in the rate estimate, and it is worth going into detail.

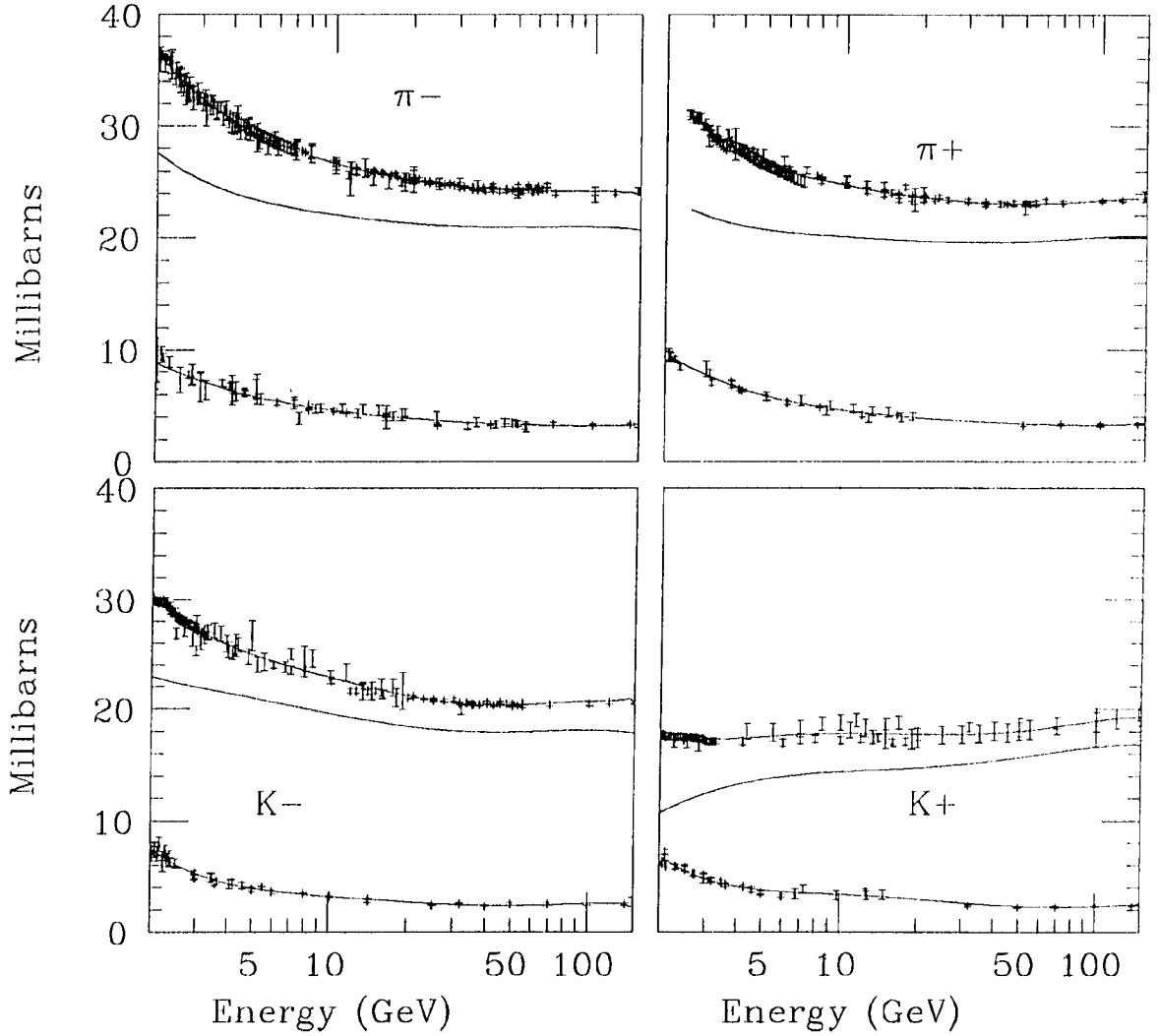


Figure B.1: Meson-proton cross sections as a function of meson energy, taken from the Particle Data Group. In each plot, the top curve is σ_{total} , the bottom curve is $\sigma_{elastic}$, and the third curve comes from subtracting the fits to the first two, $\sigma_{inelastic} = \sigma_{total} - \sigma_{elastic}$.

B.2 Sources

To get our numbers we have compared different sources:

- Published A-dependence of absorption cross sections, found in the PDB references and references therein [30,31,32];
- π -iron absorption lengths measured during detector calibrations in other experiments [35,34];
- Particle Data Booklet cross section plots (see figures B.1 and B.2) ²;
- CDF central wedge testbeam data. This only provides limits on the final values, for reasons discussed below.

Figure B.3 shows a compilation of the various cross section measurements for pions in iron. Some explanations are in order:

- The values listed in the PDB Table of Nuclear Properties are weighted averages from Carroll and Roberts. Since Roberts only studies incident neutrons, and Carroll only descends to 60 GeV, Denisov is included to learn how to scale to lower energies.
- The solid curve is the average of the π^+ and the π^- inelastic cross sections on protons taken from the fits in figure B.1, scaled to match Denisov at $p_\pi = 30$ GeV/c. We use the average since the material in the wedge contains roughly equal proportions of protons and neutrons, and the data booklet curves (or, alternatively, isospin symmetry) show that $\sigma_{\pi^+p} \simeq \sigma_{\pi^-n}$ and $\sigma_{\pi^-p} \simeq \sigma_{\pi^+n}$.
- CDHS [35] measures an effective absorption length for their iron/scintillator combination, which is then corrected to obtain a value for pure iron. Their result is somewhat lower than the other values.
- CITF [34] measures the non-interaction probability \mathcal{P} , which is then converted to a cross section for comparison.

The main point of figure B.3 is that thin-target measurements of the absorption cross section yield the same results as measurements of interaction probabilities made using

²Thanks to Bill Carithers for obtaining Vax files of the cross section data from the Particle Data Group.

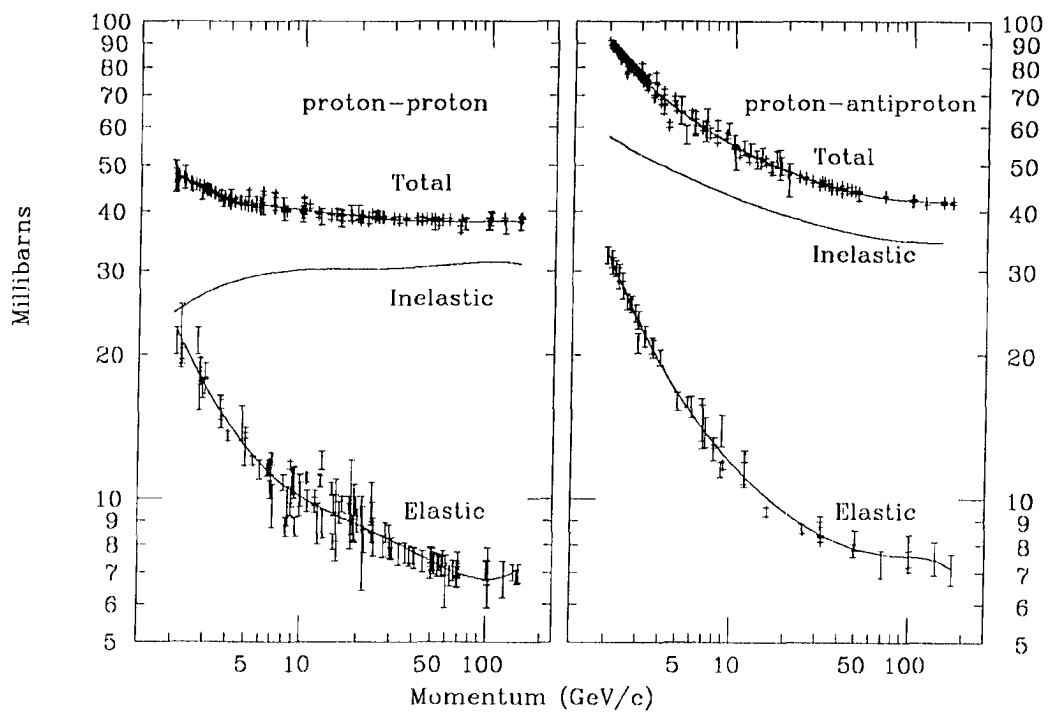


Figure B.2: Particle Data Group Proton-proton (left) and antiproton-proton (right) cross sections as a function of energy. Curves are as in preceding figure.

thick, complex calorimeters. That is, the data in figure B.3, obtained by a variety of different methods, yield consistent results (see refs [30]-[35]). Hence we can use the published values of the absorption cross sections covering a broad range of target materials, particle types and energies to calculate the number of absorption lengths in a wedge.

Carroll et al [30] provide the most recent, comprehensive set of absorption cross sections. Our method, then, is to use Carroll's values at 60 GeV/c to calculate high energy values of the number of absorption lengths in a wedge, and then scale the curves from the Particle Data Group (the $\sigma_{inelastic}$ curves of figures B.1 and B.2) to extrapolate to lower energies. Table B.2 lists Carroll's cross sections for the different target materials present in the central wedges and for the different particle types, at 60 GeV/c, as well as the absorption lengths calculated from equation (B.2) [30]. The absorption lengths are calculated using the cross section values and equation (B.2) ³.

The method just described introduces a small systematic error into our calculation. The absorption cross section,

$$\sigma_{abs} = \sigma_{total} - \sigma_{elas} - \sigma_{quasi}, \quad (B.4)$$

is different from the inelastic cross section,

$$\sigma_{inelas} = \sigma_{total} - \sigma_{elas}, \quad (B.5)$$

by σ_{quasi} , the quasi-elastic scattering cross section ⁴. The difference is less than 3% over the energy range covered by Denisov et al [32]. We use σ_{abs} to calculate the number of absorption lengths in wedge at high energy, but σ_{inelas} to extend to low energy. A systematic error arises to the extent that the energy dependence of σ_{abs} is different from that for σ_{inelas} . We consider this error to be negligible.

Central wedges contain two types of scintillator. The hadron calorimeter uses plexiglas (also called Lucite or acrylic) while the shower counter has polystyrene. (CDHS [35] uses plexipop, which is doped plexiglas and has the same absorption length.) Since both plastics are predominantly carbon, we scale from the data booklet values for the absorption length according to

$$\lambda = \lambda^{PDB} \times \frac{\sigma_{carbon}^{PDB}}{\sigma_{carbon}^{Carroll}}.$$

³The central hadron calorimeter uses plexiglas and central EM uses polystyrene.

⁴This is Carroll's nomenclature. Unfortunately, the data booklet defines σ_{inelas} to be exactly what we have called σ_{abs} .

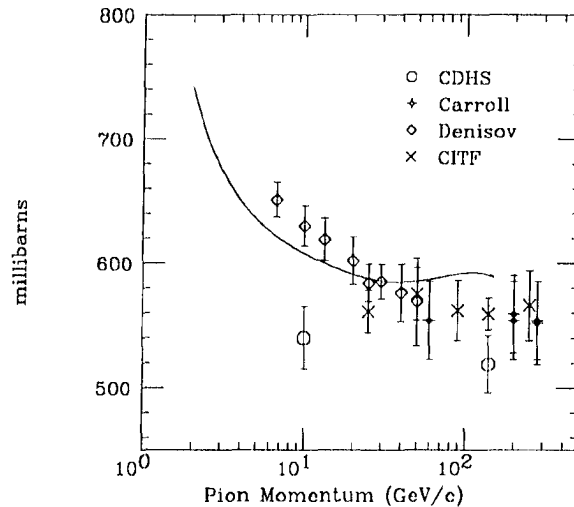


Figure B.3: Pi-iron inelastic cross sections from the various authors. Absorption lengths (CDHS) or interaction probabilities (CITF) have been converted to cross sections. The solid curve is $(\sigma_{\pi^+p} + \sigma_{\pi^-p})/2$ from figure 1, to allow for the equal proton and neutron mix in iron, scaled to match Denisov at 30 GeV.

B.3 Central Calorimeter Test Beam Data

B.3.1 Data Sample

Test beam data taken in M-Test on February 12, 1988 has been used for an analysis of the non-interactive pion punchthrough probability. A 57.1 GeV π^+ beam was directed at the center of tower 2 of wedge #30⁵. The data consists of 18482 events (run 10516). A 10 inch by 10 inch scintillator counter placed behind an additional 9 feet of steel behind the wedge served as a muon tag. The counter efficiency (for charged particles) was measured with 190 GeV pions to be 54897/56869 or 96.53% \pm 0.08% (statistical error only). The efficiency of the muon tag must be less than or equal to this number (multiple scattering and interactions in wedge and additional steel will reduce the efficiency):

$$\text{Muon tag efficiency} \leq 96.53\% \pm 0.08\%$$

3436 events are tagged as muons. Their pulse height distribution (EM + HAD) is shown in figures B.4 and B.5. The energy scale has been determined using the assumption that

⁵Thanks to Barry Wicklund and Fumi Ukegawa for making a short, special format disk file of this data.

	K^+	K^-	π^\pm	p	\bar{p}
Target	<i>Absorption Cross Sections (mb)</i>				
Lead	1360 ± 42	1414 ± 45	1479 ± 44	1730 ± 52	1805 ± 56
Iron	491 ± 28	518 ± 29	554 ± 34	685 ± 38	721 ± 41
Alu	280 ± 9	299 ± 9	324 ± 10	409 ± 12	439 ± 13
Carbon	144 ± 4	153 ± 5	169 ± 5	222 ± 7	242 ± 7
	<i>Absorption Lengths (cm)</i>				
Lead	22.3 ± 0.7	21.4 ± 0.7	20.5 ± 0.6	17.5 ± 0.5	16.8 ± 0.5
Iron	24.0 ± 1.4	22.7 ± 1.3	21.3 ± 1.3	17.2 ± 1.0	16.3 ± 0.9
Alu	59.3 ± 1.9	55.5 ± 1.7	51.2 ± 1.6	40.6 ± 1.2	37.8 ± 1.1
Plexi	114 ± 3	107 ± 3	97 ± 3	74 ± 2	67 ± 2
Poly	128 ± 4	120 ± 4	109 ± 3	83 ± 3	76 ± 2

Table B.2: Absorption cross sections (mb) and lengths (cm) for 60 GeV/c hadrons incident on different targets.

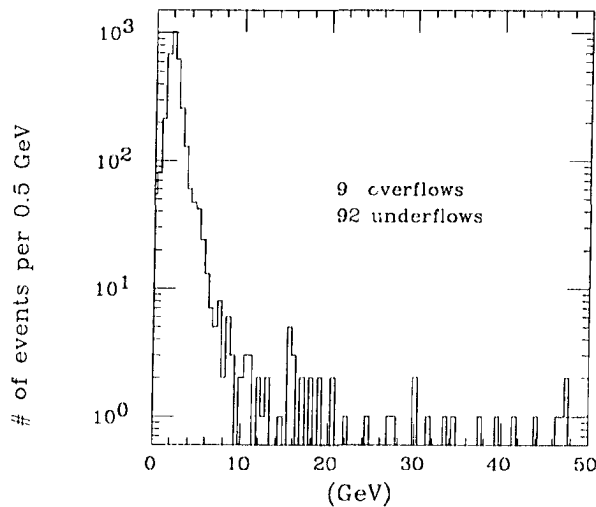


Figure B.4: Total (EM + Hadron) pulse height distribution of 57.1 GeV μ^+ 's at tower 2 center (coarse binning). Note the 92 underflow entries.

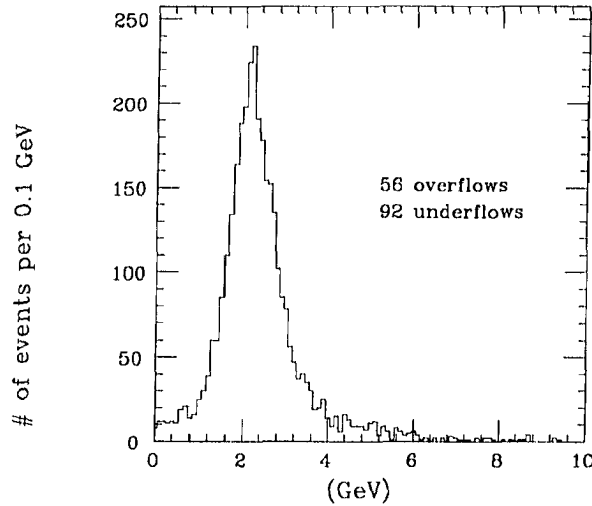


Figure B.5: Total (EM + Hadron) pulse height distribution of 57.1 GeV μ^+ 's at tower 2 center, with finer binning than figure 4.

the beam energy of 57.1 GeV is correct, and then following the standard CDF calibration procedure. The muon pulse height distribution looks Landau-like with an average of about 2.45 GeV. There is a long tail towards large pulse heights. 56 events (1.6%) for instance, have $(EM + HAD) > 10$ GeV. It is conceivable that some of these events are overlaps of two beam particles, a muon and a pion for instance. The muon efficiency with a cut of $(EM + HAD) < 5$ GeV is then at least (figure B.4):

$$\frac{(3178+92 \text{ (underflows)})}{3436} = 95.2\%$$

(57.1 GeV μ^+ 's at tower 2 center)

We are interested in measuring the non-interactive pion punchthrough probability. We will now define this to be the probability that the (57.1 GeV) π^+ gives a pulse height (EM + HAD) of less than 5 GeV. To obtain a “clean” pion sample, we begin with a total of 18482 events, followed by the following cuts:

1. Remove 3436 events tagged as muons
2. Remove 278 events tagged as having late particle hits
3. Remove 27 events for which the total pulse height exceeds 85 GeV.
4. Remove 70 events tagged as electrons by the beam Cerenkov counter

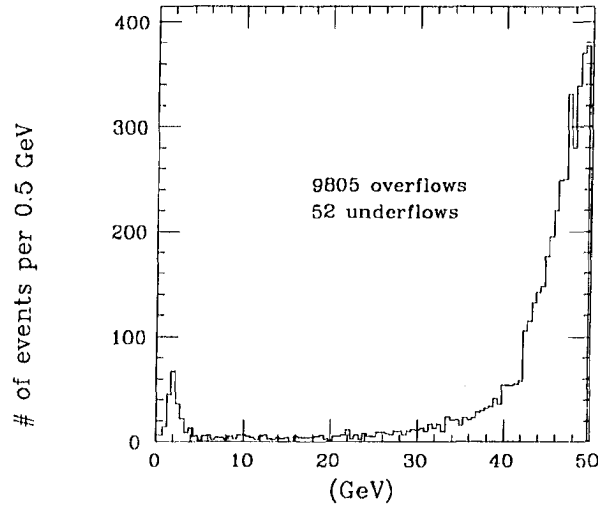


Figure B.6: (EM + Hadron) pulse height distribution of 57.1 GeV π^+ 's at tower 2 center, showing a small peak corresponding to minimum ionizing particles (non-interactive punchthrough and untagged muons). Note the 52 underflow entries.

5. Remove 189 events, untagged by the (inefficient) Cerenkov tag, but electron-like in that they have EM > 50 GeV and HAD < 3.3 GeV.

This leaves 14482 “pion” events. Note that cuts 3-5 don't remove non-interactive punch-through candidates.

B.3.2 Analysis for (EM + Hadron)

The pulse height histogram (EM + HAD) for these pions is shown in figure B.6. There are 223 events with $0 < \text{EM} + \text{HAD} < 5$ GeV and 52 underflows. The muon pulse height histogram with the same binning is shown in figure B.5. The ratio between the two is plotted bin-by-bin in figure B.7 (left). Apart from the underflow bin, the ratio looks fairly constant in the range 0 - 5 GeV at a value of $(223 \text{ pion events} / 3178 \text{ muon events}) = 0.070$. It seems reasonable then to count only $0.070 \times 92 = 6$ of the pion underflow events as real, and disregard the remaining $52 - 6 = 46$ events in the pion data (maybe there was no real beam particle in these events?). In summary then, there are $223 + 6 = 229 \pm 15$ events or 1.6% of the pion events which have $(\text{EM} + \text{HAD}) < 5$ GeV:

$$\text{Fraction of muon-like events} = 1.6\%$$

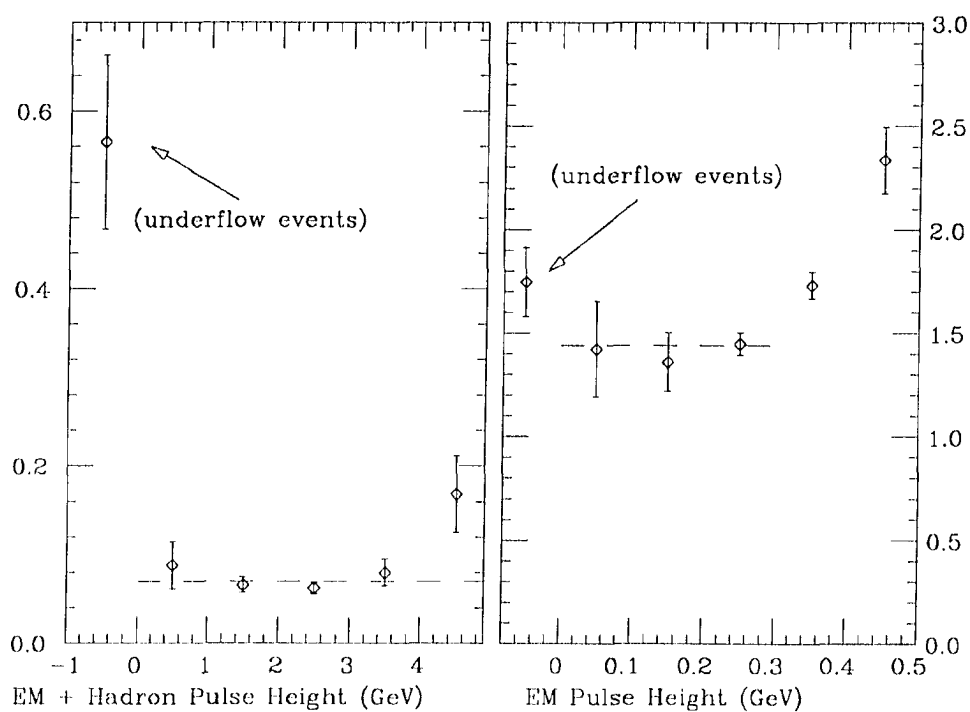


Figure B.7: Ratio $\frac{\pi}{\mu}$ of number of entries per bin in the pulse height distributions for pions and muons. Left-hand plot is for the total pulse height (EM + Hadron), right-hand plot is for the EM pulse height.

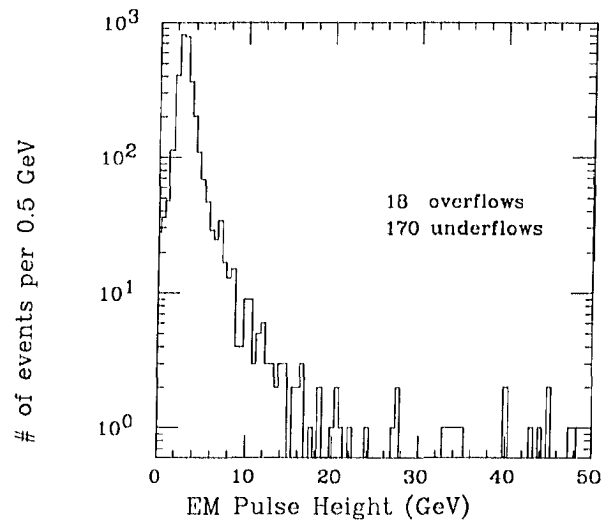


Figure B.8: EM pulse height distribution of $57.1 \text{ GeV } \mu^+$'s at tower 2 center.

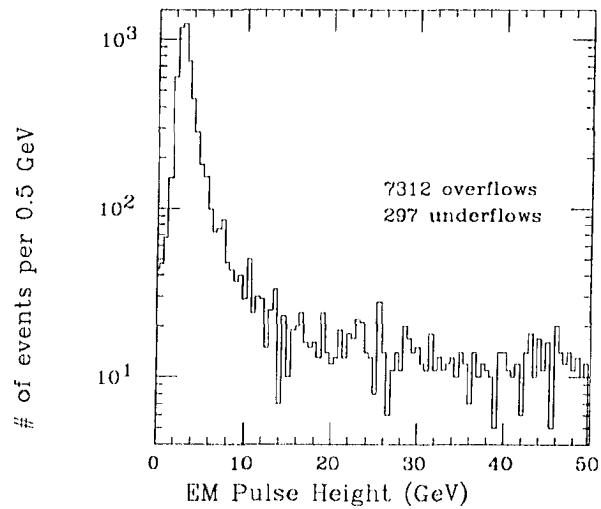


Figure B.9: EM pulse height distribution of $57.1 \text{ GeV } \pi^+$'s.

Some of these events must be muons which were untagged because of the muon tag inefficiency. There should be at least

$$3436 \times \frac{(1.0 - 0.9653)}{0.9653} = 124 \pm 4$$

such untagged muon events, leaving at most $(229 \pm 15) - (124 \pm 4) = 105 \pm 15$ non-interacting pions. The non-interactive pion punchthrough probability is therefore at most

$$\frac{105 \pm 15}{14482 - 124} = 0.73\% \pm 0.1\%$$

for 57.1 GeV π^+ 's at the center of tower 2 (corresponding to $\Lambda_{\text{wedge}} \geq 4.92 \pm 0.14$).

B.3.3 Analysis for the EM Shower Counter

A similar analysis can be performed to determine the pion interaction probability in the EM calorimeter alone. Figure B.8 shows the pulse height distribution in tower 2 (EM only) for muons, while figure B.9 shows the same distribution for pions. The bin-by-bin ratios are shown in figure B.7 (right). The ratio is approximately constant in the pulse height interval 0 - 0.3 GeV with an average value of $2092/1455 = 1.44$. The total number of pions with a muon-like pulse height is therefore $3436 \times 2092/1455 = 4940$. Correcting for the muon tag inefficiency, we therefore find that the probability that a pion is muon-like in the EM calorimeter is

$$\frac{4940 - 124}{14482 - 124} = 33.5\% \pm 0.5\% \quad (\text{statistical only})$$

This number is surprisingly small. It would correspond to the EM calorimeter being 1.09 absorption lengths for these pions ($e^{-1.09} = 0.336$), which is more than calculated from the materials (see below).

B.4 Λ_{wedge} Calculations

Given the absorption lengths in table B.2, we can add up the different materials to obtain a value for Λ for a central wedge, for 60 GeV/c particles. This section demonstrates the method for the pion case.

Material	# layers	layer thickness	total thickness	π abs lengths
Coil sim ¹⁾			6.4 cm	0.125
Front plate			0.9525	0.019
Pb	30	$2.54/8 = 0.3175$	9.525	0.465
Al cladding	30	$2 \times 0.15 \times 2.54$	2.286	0.045
Str. chmbr.				$0.022\Lambda_p^2)$
Polystyrene	31	0.5	15.5	
Mylar	1	0.4×2.54	1.016	
All plastic ³⁾			18.034	0.165
Total				0.841 ⁴⁾

Table B.3: Material thicknesses and numbers of absorption lengths for the components of the central electromagnetic shower counter. Notes are given in the text.

B.4.1 Central Hadron

Fe: $(32 \text{ layers}) \times (2.54 \text{ cm/layer}) \div (21.3 \text{ cm}) = 3.82 \pm 0.23$ abs lengths

Scin: $(32 \text{ layers}) \times (1.0 \text{ cm/layer}) \div (97 \text{ cm}) = 0.33 \pm 0.01$ abs lengths

Spring retainers: $0.7 \text{ cm Fe} \rightarrow 0.03$ absorption lengths

$$\Lambda_{CHA} = (4.18 \pm 0.2) / \sin \theta \text{ absorption lengths for } 60 \text{ GeV/c pions.}$$

B.4.2 Central EM

The shower counter contains a wider variety of material than the central hadron calorimeter: aluminum cladding on the lead, strip chambers, etc. Table B.3 summarizes the contributions from the different materials to the total absorption length. The total is

$$\Lambda_{CEM} = (0.84 \pm 0.3) / \sin \theta \text{ absorption lengths for } 60 \text{ GeV/c pions.}$$

We can now compare our result with the test beam value for tower 2,

$$\begin{aligned} \Lambda_{CEM}(\text{tower2}) &= 0.84 / \sin(72.2^\circ) \\ &= 0.88 < 1.09 \quad (\text{test beam result}). \end{aligned}$$

<i>Absorption Lengths per Wedge</i>				
K^+	K^-	π^\pm	p	\bar{p}
4.35 ± 0.20	4.60 ± 0.21	5.02 ± 0.23	6.09 ± 0.28	6.45 ± 0.29

Table B.4: Total number of absorption lengths per wedge, Λ_0 , such that $\Lambda = \Lambda_0 / \sin(\theta)$, for 60 GeV/c hadrons.

Notes for table B.3:

1. The coil simulator has roughly the same number of absorption lengths as the outer tracking and coil;
2. The strip chamber thickness is given in proton absorption lengths, taken from reference [38]. The correction for pion lengths is negligible;
3. Summing all listed layers gives 1.52 cm less than the actual stack height. This ‘leftover’ material is treated as plastic;
4. The lead stack thickness varies from tower to tower, to maintain a constant number of radiation lengths, but to a good approximation the actual number of absorption lengths traversed by a track with angle θ relative to the beam axis is obtained from $0.841/\sin\theta$. (The totals for each tower, in proton absorption lengths taken from the data booklet, are tabulated in the CEM NIM paper [38].)

B.4.3 Entire Wedge

To compare with the testbeam result we use $\theta = 72.2^\circ$ for tower 2, and find

$$\Lambda(\text{tower 2}) = 4.18/\sin(72.2^\circ) + 0.86 = 5.25 \pm 0.24,$$

compared to the lower limit, 4.92 ± 0.14 , obtained in the test beam.

Then for 60 GeV/c pions incident on a central wedge, there are $(4.18 + .84) = 5.02 \pm 0.23$ absorption lengths in front of the muon chambers. Similar analyses for the other hadrons yield the results listed in table B.4.

B.5 Low Energy Extrapolation

With the high energy values in hand (see table B.4), we scale the PDB curves for σ_{inelas} from figures B.1 and B.2, in order to extrapolate to lower energy.

The PDB curves are for proton targets, whereas the wedges consist of roughly equal numbers of protons and neutrons. Hence some care is needed. As stated earlier, for pions we use the average inelastic cross section

$$\sigma_{\pi} = (\sigma_{\pi+p} + \sigma_{\pi-p})/2 \quad (\text{B.6})$$

since $\sigma_{\pi+p} \simeq \sigma_{\pi-n}$ and $\sigma_{\pi-p} \simeq \sigma_{\pi+n}$ (see data booklet curves). However, kaons require a separate curve for $K^+ (u\bar{s})$ and for $K^- (\bar{u}s)$, since the anti-up quark can annihilate with up quarks in the nucleon N so that $\sigma_{K-N} > \sigma_{K+N}$. Now since neutrons have fewer up quarks it is also true that $\sigma_{K-p} > \sigma_{K-n}$ and hence for a composite target we should use some sort of average of the K^+N or the K^-N cross sections. Unfortunately, those measurements are unavailable in our energy domain so we content ourselves with using the shapes of the σ_{K+p} and σ_{K-p} curves, and scale them to match the high energy values from the previous section. This compromise contributes to our final systematic error.

Figure B.10 (dashed lines) shows the extrapolations of the high energy values of the number of absorption lengths for particles at normal incidence on a wedge down to 2.5 GeV. Fits to the curves from the particle data book (figures B.1 and B.2) are scaled to match the values in table B.4 at 60 GeV/c. The curves are six parameter polynomial fits in $\log(E)$. That is,

$$\Lambda(E) = \sum_{n=0,5} P_n (\log E)^n \quad (\text{B.7})$$

where the values of the parameters P_i are listed in table B.5.⁶

A correction can be applied to the curves in figure B.10. Since a minimum ionizing particle traversing a wedge loses about 1.3 GeV,⁷ the inelastic cross section will vary as E changes. That is, one can calculate

$$\Lambda_{effective} = \frac{\int \Lambda(E) dE}{\int dE}. \quad (\text{B.8})$$

⁶Thanks to John Filaseta and Jim Wiss of E687 for providing the fitting routine.

⁷1.3 GeV is an average over the η range of the muon chambers. The most probable value varies from 1.2 GeV in tower 0 to 1.6 GeV in tower 6.

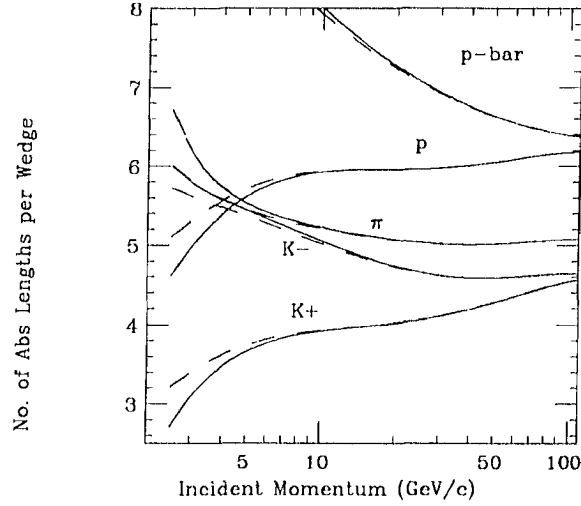


Figure B.10: Number of absorption lengths at normal incidence on a central wedge for different hadrons.

Particle	P0	P1	P2	P3	P4	P5
π	8.492	-4.713	2.968	-0.9973	0.1679	-0.0110
K^+	1.718	2.161	-0.533	-0.0925	0.0555	-0.0057
K^-	6.676	-1.832	1.326	-0.6193	0.1337	-0.0103
p	3.814	1.442	0.2904	-0.4478	0.1200	-0.0100
\bar{p}	12.440	-3.137	0.7221	-0.1178	0.0121	-0.0004

Table B.5: Fit parameters for the momentum dependence of Λ_0 .

In figure B.10 the solid curves are corrected for $\frac{dE}{dx}$ losses, dashed curves are uncorrected. Error bars on the curves are about 3%. The correction is included in figures B.10, B.11, and B.12. The effect in figure B.11 is as much as 20% for 4.5 GeV π^- 's.

The fortran function C\$MUO:CMWINT in the development area of the CDF offline analysis package uses the polynomial fits and applies the $\frac{dE}{dx}$ correction to provide the user with Λ , given the particle species and energy.

Since the η distribution of mesons from 'generic' events is flat in the region covered by the central muon chambers, it is convenient to calculate the average value of Λ for that region,

$$\Lambda_{avg} = \frac{\int \Lambda(\eta) d\eta}{\int d\eta}. \quad (\text{B.9})$$

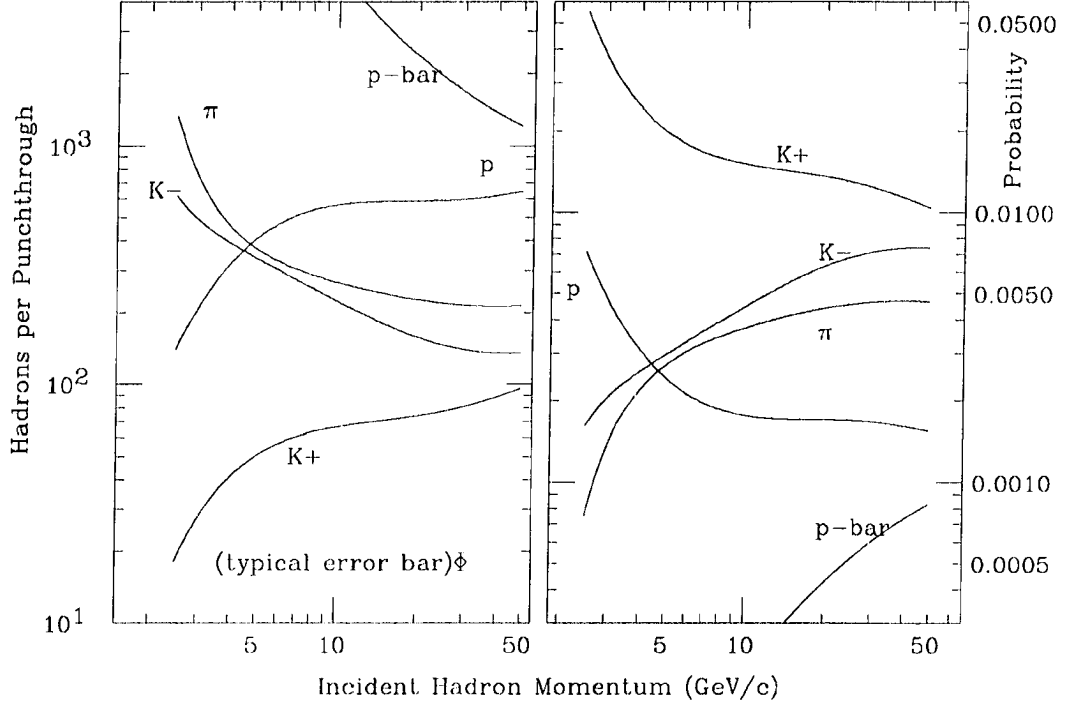


Figure B.11: Noninteractive punchthrough probability (right) and inverse probability (left) for hadrons incident on a central wedge, averaged over the η coverage of the central muon chambers. Includes $\frac{dE}{dx}$ correction.

Here, $\Lambda(\eta)$ comes from $\Lambda(\theta) = \Lambda_0/\sin\theta$, where θ is the track angle relative to the beam axis, and $\eta = \cot(\log \frac{\theta}{2})$ is the pseudorapidity. Figure 11 shows $e^{\Lambda_{avg}}$ and $e^{-\Lambda_{avg}}$ as a function of momentum. It shows that 1 out of 25 positive 3 GeV K^+ 's will not even notice the calorimeter as they sail through, as compared to 1 in 700 for π 's.

B.6 Muon Background Charge Asymmetry

There are two backgrounds to the inclusive direct muon spectrum in the central region (CMU): Pion and kaon decay, and non-interactive hadron punchthrough. There is no difference between the signature in the detector for direct muons at a given p_t and non-interactive charged hadrons of the same p_t . Decays, on the other hand, can sometimes be

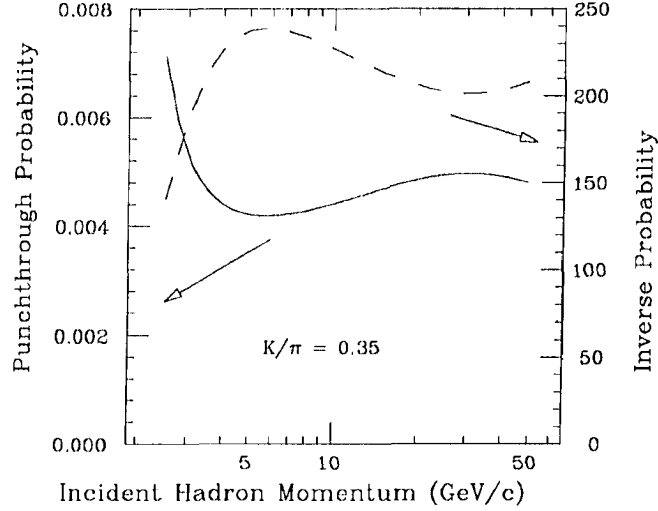


Figure B.12: Overall noninteractive punchthrough probability and inverse probability assuming $\frac{K}{\pi} = \frac{v+\bar{v}}{\pi} = 0.35$ (solid curve). Number of hadrons per noninteractive punchthrough is also shown (dashed curve).

rejected because the decay muons have, on the average, lower momentum than the parent hadrons. The reconstructed p_t in the CTC is therefore on the average lower for the decay muons, the decay muons will suffer more multiple scattering in the calorimeter (leading to a less accurate track matching), and some of them will range out before reaching the muon chambers. This effectively reduces the decay background (due to the steeply falling p_t spectrum). Some kaon decays can also be rejected due to observable kinks in the CTC. Kinks that effectively straighten the CTC tracks without being rejected, can, on the other hand, significantly increase the decay background (again due to the steeply falling p_t spectrum). We will assume in the following that this effect is not dominant.

Let us define the background charge ratio $R(p_t)$ as the ratio of positives to negatives at a given p_t :

$$R_{backgr}(p_t) = \frac{\text{Positives}(p_t)}{\text{Negatives}(p_t)} = \frac{1 + \frac{N_K}{N_\pi} \frac{P_{K+} + \epsilon_K D_K}{P_\pi + \epsilon_\pi D_\pi} + \frac{N_p}{N_\pi} \frac{P_p}{P_\pi + \epsilon_\pi D_\pi}}{1 + \frac{N_K}{N_\pi} \frac{P_{K-} + \epsilon_K D_K}{P_\pi + \epsilon_\pi D_\pi} + \frac{N_{\bar{p}}}{N_\pi} \frac{P_{\bar{p}}}{P_\pi + \epsilon_\pi D_\pi}} \quad (\text{B.10})$$

where P_π , P_{K+} , P_{K-} , P_p , and $P_{\bar{p}}$ are the pion (charge independent), kaon (charge dependent), proton and antiproton non-interactive punchthrough probabilities, $\epsilon_\pi D_\pi$ and $\epsilon_K D_K$ the (charge independent) decay probabilities to $\mu\nu$ multiplied by the probabilities for non-rejection, and N_π , N_K , $N_p = N_{\bar{p}}$ the (charge independent) numbers of particles at

the given p_t .

The charge ratio for punchthrough alone (i.e. ignoring decays) represents an upper limit for the (punchthrough + decay) charge ratio. A lower limit for the charge ratio can be obtained by overestimating the number of retained decay events, for instance by completely ignoring the fact that some decay events can be rejected. This allows us to write

$$\frac{1 + \frac{N_K}{N_\pi} \frac{P_{K^+} + D_K}{P_\pi + D_\pi} + \frac{N_p}{N_\pi} \frac{P_p}{P_\pi + D_\pi}}{1 + \frac{N_K}{N_\pi} \frac{P_{K^-} + D_K}{P_\pi + D_\pi} + \frac{N_p}{N_\pi} \frac{P_p}{P_\pi + D_\pi}} < R_{backgr}(p_t) < \frac{1 + \frac{N_K}{N_\pi} \frac{P_{K^+}}{P_\pi} + \frac{N_p}{N_\pi} \frac{P_p}{P_\pi}}{1 + \frac{N_K}{N_\pi} \frac{P_{K^-}}{P_\pi} + \frac{N_p}{N_\pi} \frac{P_p}{P_\pi}} \quad (\text{B.11})$$

where again the limits correspond to $\epsilon = 1$ and $\epsilon = 0$, respectively. These limits are illustrated in figures B.13 a and b for two different assumptions about the particle ratios (representing reasonable limits on the heavy particle fractions):

- a) $N_K/N_\pi = N_{(p+\bar{p})}/N_\pi = 0.10$ independent of p_t
- b) $N_K/N_\pi = N_{(p+\bar{p})}/N_\pi = 0.36$ independent of p_t (the UA5 mix).

The upper curves are calculated assuming no contribution from decay-in-flight, while the lower curves come from the assumption that all secondary muons would pass the muon identification cuts.

The decay probabilities times branching ratios have been calculated using a radius of 215 cm (the interface between the EM and hadron calorimeters), pion and kaon masses of 0.13957 and 0.49367 GeV/c² and $c\tau$ for pions and kaons of 780.4 and 370.9 cm:

$$D_\pi = 1 - e^{-0.03845/p_t} \text{ for pions}$$

$$D_K = 0.635(1 - e^{-0.2862/p_t}) \text{ for kaons}$$

where 0.635 is the branching ratio for $K \rightarrow \mu\nu$.

A significant deviation from 1.0 is observed in all cases at low p_t . The inclusive CMU charge ratio for B0 data should therefore provide a useful handle on the punchthrough background (we expect a charge ratio of 1.0 both for the direct muon signal and for the decay background). Once observed, this charge ratio deserves a more careful calculation.

What about dimuons? Whereas it is generally believed that the inclusive (single) CMU rate at low p_t is dominated by background (so that the charge asymmetry calculated above should be observable), the dimuon rate may be dominated by signal (for which the $\frac{++}{--}$ ratio is 1.0). The $\frac{++}{--}$ ratio for the background should instead be the square of R calculated above. The $\frac{++}{--}$ ratio in B0 data, compared to the $\frac{\pm}{\pm}$ ratio for single muon candidates, should therefore be a good indicator of background in the dimuon sample.

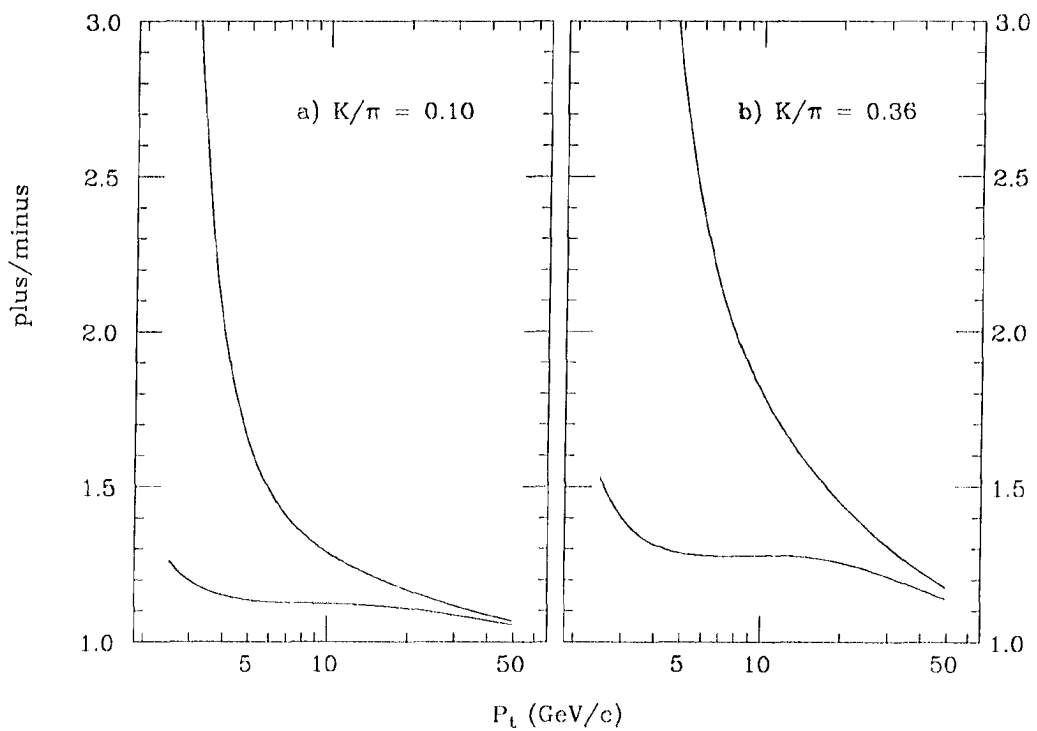


Figure B.13: Limits on predicted charge asymmetry for tracks in the muon chambers. a) $\frac{K}{\pi} = \frac{(p+\bar{p})}{\pi} = 0.10$, b) $\frac{K}{\pi} = \frac{(p+\bar{p})}{\pi} = 0.36$.

B.7 Conclusion

The rate for non-interacting hadron punch-through's in the central muon chambers is sensitive to both the energy dependence of the inelastic cross section and the derivative of the dependence. Protons turn out to make a non-negligible contribution to the rate, and the varying amounts of material traversed by particles with different pseudorapidity η also changes the rate. Hence the calculation is fairly complex and there are a number of systematic uncertainties that can fudge the final answer.

Even so, we have presented a method for calculating the rates and the error on the rate, and first indications are that agreement with the data is reasonable. One consequence of our results is that we expect to see a charge asymmetry amongst the tracks reaching the central muon chambers. This excess of positively charged tracks arises from the small absorption cross section for K^+ 's.

Appendix C

Decay-in-Flight Acceptance

The decay of pions and kaons into muons is simulated using CDFSIM, and then the full, standard event reconstruction is applied in order to calculate the acceptance of the central muon chambers for secondary muons ¹.

C.1 Why Use the Monte Carlo?

The probability for a pion or a kaon to decay to a muon, via the processes

$$\pi \rightarrow \mu\nu, \quad K \rightarrow \mu\nu$$

is simply

$$\mathcal{P}(p_t) = 1 - e^{-Mr/c\tau p_t} \approx \frac{Mr}{c\tau p_t} \quad (\text{C.1})$$

where $c\tau$ is the decay length, r is the distance from the beam axis traveled by the meson, M is the meson mass, and p_t is the transverse momentum of the meson ². Values are listed in table C.1. (The approximation is valid for $r = R_{\text{cmu}}$ and the momentum acceptance of the central muon chambers, and improves with increasing p_t .)

Furthermore, the energy distribution of the decay muons is flat over the range of kinematically allowed energies E_μ , which is

$$f_i E_{\text{meson}} \leq E_\mu \leq E_{\text{meson}},$$

where $f_\pi = 0.57$ for pions and $f_K = 0.05$ for kaons,

and where E_{meson} is the energy of the primary pion or kaon. Hence, given the geometry of the central muon coverage and the branching ratios for K or $\pi \rightarrow \mu\nu$, one should be

¹The contents of this appendix have appeared as a CDF internal memo, [37].

²'Transverse momentum', p_t , means transverse relative to the beam axis.

	M (MeV)	$c\tau$ (cm)	$mR_{cmu}/c\tau$ (MeV)	$B.R.$
π^\pm	139.6	780.4	62.1	100 %
K^\pm	493.7	370.9	461.9	63.5 %

Table C.1: Some properities of kaons and pions. $R_{cmu} = 347$ cm is the radius of the central muon chambers. $B.R.$ is the branching ratio to $\mu\nu$.

able to calculate the probability that muons above some momentum threshold reach the muon chambers, without resorting to complicated monte carlo's.

But the above gives only a rough estimate of the decay muon acceptance. Three principal effects muddy the picture (see figure 2.7):

1. **Low Secondary Momentum** The decay muons have lower momenta than the parent mesons, so some of the secondary muons will fail the muon identification cuts because

- the track may fail the p_t cut;
- increased multiple scattering for the soft secondary could cause it to fail the CTC/CMU track matching cuts;
- $\frac{dE}{dx}$ losses in the calorimeter cause some muons to range out before reaching the muon chambers. Range-out energy of a muon traversing an entire wedge is 1.4 GeV/sin θ .

2. **Kinks** The decaying meson gives the muon a 'kick' in the direction transverse to the parent momentum, which can produce a 'kink' in the track, with different consequences:

- The central tracking pattern recognition code may not recognize two distinct tracks, and will instead fit the parent and secondary tracks to a single track with some 'compromise' momentum value. Figure C.2 shows momentum distributions for tracks reconstructed from mesons that were forced to decay in the simulation. Note that some tracks have higher momenta than their parents!

- The transverse kick can send the muon astray, so that it fails the CTC/CMU track matching cuts. Coupled with the increased multiple scattering of the soft secondaries, this is a non-negligible effect.
 - The reconstructed track will have an impact parameter or residuals values that cause the track to fail quality cuts.
3. $\frac{dE}{dx}$ **losses** slow the meson down and thereby increase its decay probability. This is a small correction to the total rate, but for low momentum mesons it decreases the magnitude of the expected charge asymmetry, discussed later in this note and in reference [36].

CDFSIM, the CDF detector simulation, includes these effects and allows for a more realistic calculation of the decay acceptance.

Earlier work by Skarha showed negligible stiffening of the minimum bias dN/dp_t distribution due to misreconstruction of kinked tracks [28]. Muon data, however, contains more decay contamination and the effect is larger.

C.2 The Method

The shape of the observed momentum distribution for decay muons,

$$\left(\frac{dN_\mu}{dp_t}\right)_{obs}, \quad (\text{C.2})$$

depends on the shape of the parent meson distribution, $\frac{dN}{dp_t}$, which will be different for different physics studies (i.e., min bias, jets, vector bosons, etc). Rather than choosing a specific parametrization for $\frac{dN}{dp_t}$, we have adopted a more general approach.

C.2.1 Event Generation

FAKEV generates 3000 mesons at each of 24 transverse momentum. The transverse momenta are

$$p_t^{meson} = (2, 3, 4, \dots, 19, 20, 22, 24, \dots 30) \text{ GeV}/c. \quad (\text{C.3})$$

The meson distributions in azimuth angle ϕ and in pseudorapidity $|\eta| < 1.1$ are flat. The η interval is larger than the range covered by the central muon chambers, $|\eta| < 0.65$, to allow for secondary muons scattered to wide angles in the rz -plane of the detector.

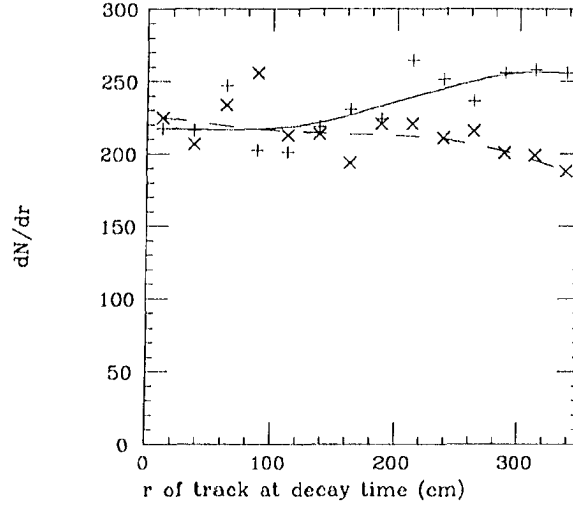


Figure C.1: Distribution of radii at which a parent meson decays into a muon. The solid curve (+’s) includes the dE/dx losses that slow down the parent mesons, thereby increasing the decay probability in the calorimeter. The dashed curve (X’s) is uncorrected. The two curves are the same until the beginning of the calorimeter ($r \simeq 150$ cm). The curves are only intended to guide the eye.

FAKEV also selects the decay radius for the meson according to the distribution shown in figure C.1 (solid curve). The decay radius r_{dk} is the distance traveled by the meson before the simulation forces the particle to decay,

$$0 < r_{dk} < R_{cmu}, \quad R_{cmu} = 347\text{cm},$$

where R_{cmu} is the innermost radius of the central muon chambers. As CDFSIM steps a particle through the layers of the detector, it compares the current radial position r of the particle with r_{dk} , and if $r \geq r_{dk}$ then the program forces the decay of the particle. However, if the meson has already showered then decay will not occur. In this way we correctly find the fraction of mesons that decay before reaching the muon chambers.

Figure C.1 shows the distribution of decay radii for simulated 7 GeV/c kaons. The dashed curve is the distribution that comes from equation (C.1), for fixed p_t . The solid curve includes a correction for the dE/dx losses of the meson. As a meson traversing the calorimeter slows down due to multiple coulomb interactions, its decay probability per unit distance increases. The r -dependence of p_t in equation (C.1) is included in the calculation. The solid and dashed curves are the same until the beginning of the calorimeter ($r \simeq 150$

CTC Track Cuts			CTC/CMU Match Cuts			
D_0	Δz_{vtx}	p_t		dx	dz	$d\alpha$
0.5 cm	5.0 cm	2.0 GeV/c	<i>loose</i>	20. cm	20. cm	0.2 rad
			<i>tight</i>	8. cm	15. cm	0.06 rad

Table C.2: Values of the cuts made on the CTC tracks, and on the match between the CTC track and the CMU stub. The parameters are described in the text.

cm) and differ by about 20% at the muon chambers.

C.2.2 Track Reconstruction

After simulating the propagation of the mesons and their daughters through the detector, the results are analysed with the same programs used for events from $p\bar{p}$ collisions. That is, we reconstruct the ‘stubs’ in the muon chambers, reconstruct the CTC tracks using the vertex-constrained fit, extrapolate the CTC track through the calorimeter (including effects of the return magnetic field in the steel), and then match the closest track/stub pair at the muon chambers. Even these very simple events produce multiple CTC tracks and muon stubs: multiple tracks arise if the decay kink is so large that the reconstruction algorithm resolves two tracks, and multiple stubs can come from knock-on electrons produced in the chamber walls. The resulting track/stub matches are considered muon-candidates, and figure C.2 shows the distributions of observed transverse momenta for each of the parent meson momenta.

Cuts are made on both the CTC track quality and on the CTC/CMU match. Table C.2 lists the cut values. D_0 is the distance of closest approach of the track to the collision vertex in the $r\phi$ -plane of the detector (impact parameter). In the rz -plane, $\Delta z_{vtx} = |z_{p\bar{p}} - z_{trk}|$ is the distance between the collision vertex and the z -coordinate of the track at $r = 0$. The transverse momentum p_t is the observed value as measured by the CTC track reconstruction code. The CTC/CMU matching parameters dx , dz are the differences, in centimeters, between the CMU stub and the extrapolated CTC track at the muon chambers, in the ϕ -direction and along the beam axis, respectively. $d\alpha$ is the slope difference in the $r\phi$ -plane between the CMU stub and the CTC track.

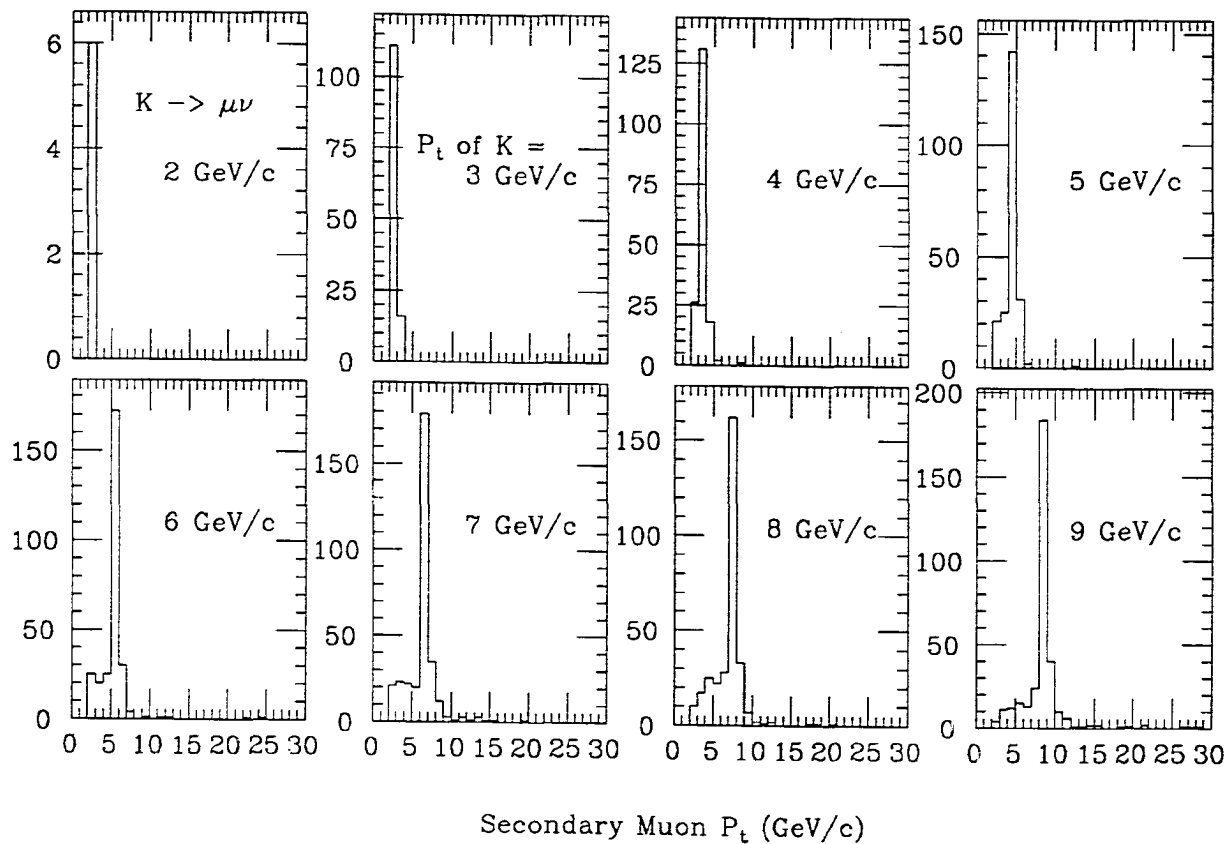


Figure C.2: Transverse momentum distributions for muons from the decay of simulated kaons that pass the 'loose' matching cuts. Primary kaon p_t is shown in each plot.

Given the plots in figure C.2, one can calculate the observed muon momentum distribution (equation C.2) for an arbitrary parent distribution, using the recipe

$$N(p_t^\mu) = \frac{1}{3000} \sum_j d_j n_j(p_t^\mu) m(p_j^K) \quad (\text{C.4})$$

where $N(p_t^\mu)$ is the observed number of muons with transverse momentum p_t^μ ;

3000 is the number of generated parent mesons;

j is an index running over the meson momenta of equation (C.3);

p_j^K is the parent meson transverse momentum for the j^{th} plot in figure C.2;

d_j is the probability for the meson to decay before the muon chambers;

$n_j(p_t^\mu)$ is the number of entries in the p_t^μ bin of the j^{th} plot in figure C.2;

$m(p_j^K)$ is the number of parent mesons with momentum p_j^K .

Restated, the factor $d_j n_j(p_t^\mu)/3000$ is the probability of a parent meson of momentum p_j^K producing a muon with momentum p_t^μ .

For the dashed curve in figure C.1, $d_j = (1 - e^{-MR_{\text{cmu}}/crp_j^K})$, using the constants listed in table C.1. But in the dE/dx corrected simulation, d_j is a constant calculated in the simulation, and is typically 10% larger than d_j for no dE/dx .

C.3 Sample Calculations

We illustrate equation (C.4) with two examples, namely, a flat momentum distribution for the parent mesons, and a distribution like the one for the charged tracks in the 1987 jet data.

C.3.1 Flat Input Spectrum

In this case, $m(p_j^K) = 1$ for all j in equation (C.4). Figure C.3 shows $N(p_t^\mu)$ for kaons, for two different sets of track/stub matching cuts. The cuts are listed in table C.2.

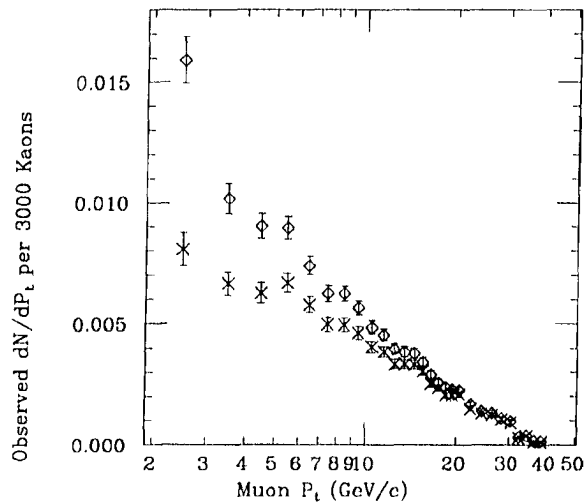


Figure C.3: Acceptance for muons from kaon decay-in-flight assuming a flat distribution of parent momenta. In the top curve, loose cuts for the match between the CTC track and the CMU stub have been applied, while the lower curve had tight cuts.

C.3.2 Jet $\frac{dN}{dp_t}$ Distribution

In this case, $m(p_j^K)$ in equation (C.4) comes from a rapidly falling distribution, typical of the charged tracks in 1987 jet data. Figure C.4 shows the resulting secondary muon spectrum, for two extreme choices of the $\frac{K}{\pi}$ ratio [27]. The muons have passed the tight cuts of table C.2. The total rate is fairly insensitive to the particle mix, which is simply a reflection of the fact that the acceptances for kaons and pions separately are comparable.

C.3.3 Do-It-Yourself

The interested reader will have a parent $\frac{dN}{dp_t}$ distribution of his own, for which he will want to calculate the observed secondary muon spectrum. A standalone Fortran program that reads the contents of the plots in figure C.2 and then calculates equation (C.4) is available, and is thoroughly described in the Vax file

FNAL::USR\$ROOT:[DSMITH.DIF]CMDIF.DOC .

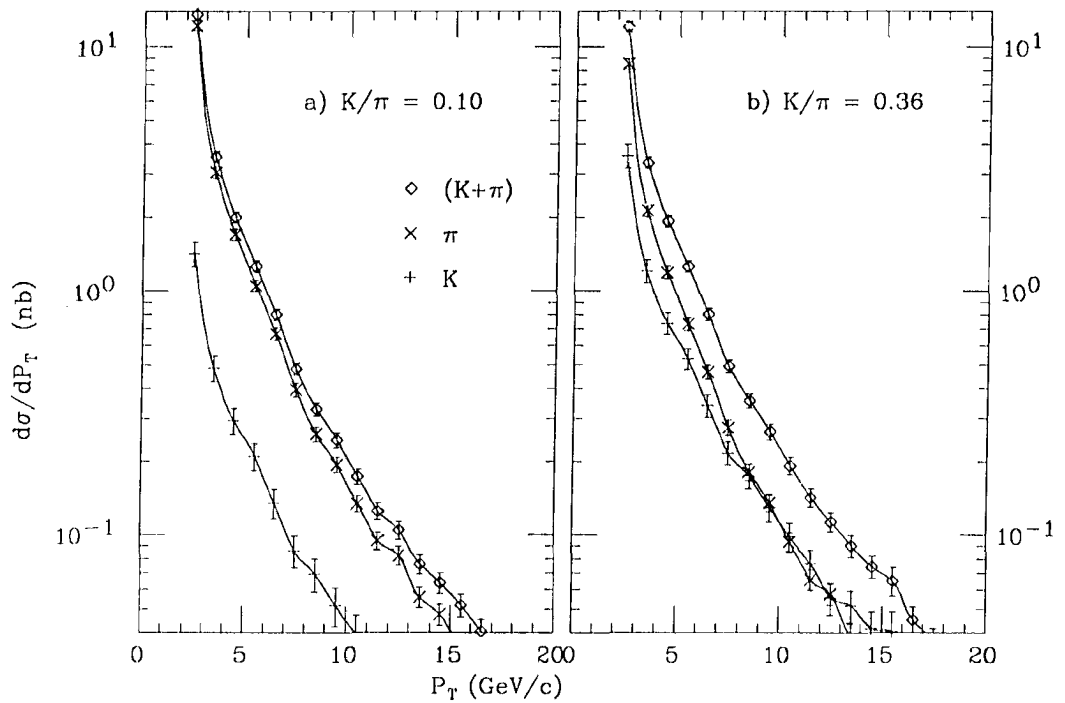


Figure C.4: Transverse momentum distribution of observed decay muons, $(\frac{d\sigma_\mu}{dp_t})_{obs}$, based on a parent meson distribution similar to that of charged tracks in jet events. The contributions from pions and kaons are shown, together with the sum of the two, for two different particle mixtures.

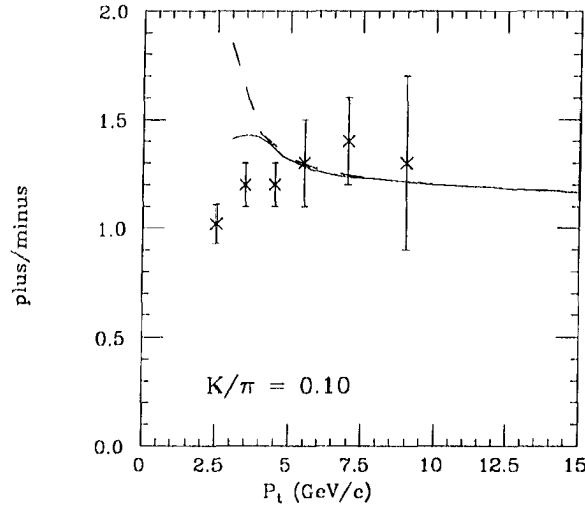


Figure C.5: Charge asymmetry in the central muon chambers. The curves combine non-interactive punchthrough with meson decay-in-flight. The solid curve includes the meson dE/dx losses in the calorimeter, while the dashed curve is uncorrected. The points come from 1987 muon data.

C.4 Charge Asymmetry

The small absorption cross section for positive kaons leads to an excess of positive tracks in the central muon chambers. Charge symmetric contributions to the central muon rate, such as decay-in-flight or prompt muons, will decrease the observed asymmetry. An earlier CDF note [36] (see appendix on noninteractive punchthrough) set limits on the magnitude of the asymmetry by making broad assumptions about the contribution from decay-in-flight. Now we are in a position to refine the prediction.

Figure C.5 shows the ratio

$$R(p_t) = \frac{N_+(p_t)}{N_-(p_t)}$$

where $N_+(p_t)$ and $N_-(p_t)$ are the numbers of positive and negative tracks observed in the central muon chambers, as a function of transverse momentum. The solid curve uses the results of the monte carlo simulation to calculate the number of tracks coming from muon decay. The dashed curve does not include the dE/dx correction. Only non-interactive punchthrough, taken from reference [36], and decay-in-flight are considered. R is an overestimate of the observe The fraction of kaons and protons in the charged track spectrum in the CTC is taken to be $\frac{K}{\pi} = \frac{(p+\bar{p})}{\pi} = 0.10$.

Also shown in figure C.5 are points from 1987 muon data, using the tight cuts of table C.2. The agreement is close but not perfect. At the lowest p_t , a technical hurdle causes an overestimate of the asymmetry. Correcting this point requires considerable additional work and did not seem worthwhile. At higher p_t , other effects may contribute:

- We have considered only non-interactive punchthrough and decay-in-flight. A minimum ionizing cut on the data removed most shower leakage (interactive punchthrough), but the remaining contribution will diminish the observed asymmetry;
- The $\frac{K}{\pi}$ mixture of the parent spectrum is poorly understood but is probably greater than 0.10. Increasing $\frac{K}{\pi}$ increases the predicted asymmetry;
- Cosmic rays and prompt muons make small contributions to the data sample we used, but both diminish the observed asymmetry and they are not included in the prediction. Track misassociation, where a muon stub is matched with the wrong central track, is another possible background.

In spite of these shortcomings, the data and the prediction agree qualitatively and we conclude that the asymmetry is a useful tool for understanding the single muon data.

C.5 Conclusions

A general method for calculating decay-in-flight rates in the central muon chambers shows that the contribution from π decay falls off more quickly (as a function of p_t) than the contribution from K decay, so that for reasonable input spectra and hadron mixes, the two rates become comparable in the $p_t = 5\text{-}10$ GeV/c range. By 15 GeV/c, decay-in-flight is a small background for central muon studies. Combining the decay-in-flight study with earlier non-interactive punchthrough results leads to a prediction of the charge asymmetry that compares favorably with 1987 muon data.

Appendix D

Dimuons

D.1 Generalities

Events containing two prompt muons provide an extremely powerful tool for studying the physics of high energy collisions. In the first place, the backgrounds are much smaller because the probability of seeing two decay-in-flights or punchthroughs is roughly the square of the single track probability. In the second place, certain signatures are definitive and unambiguous, most notably the presence of peaks in the invariant mass distribution. A dimuon sample not only gives a clean signal, but helps clarify the single muon signature as well. Almost all the muon candidates in an invariant mass peak are true muons and studying the characteristics of those tracks (matching distributions, calorimeter signals, etc) is a sure way to refine the single muon identification cuts and optimize the signal-to-noise. Future analyses will certainly center on dimuons.

In this thesis, however, dimuons give only qualitative results because no trigger in the 1987 run was efficient for dimuons. With the exception of $Z^0 \rightarrow \mu^+ \mu^-$, the different dimuon production mechanisms generate mainly low p_t muons, whereas the Golden muon trigger required $p_t > \sim 10$ GeV/c (intended for W^\pm detection, see [2]). The rate for dimuons in other triggers is a factor of ten less than for single muons, due to the muon branching ratio for heavy mesons (table 1.2). Chapter 4 shows that the number of single muons in the jet triggers is quite small, and the order of magnitude reduction for dimuons kills any hope of quantitative conclusions. Nevertheless, most of the 1987 trigger thresholds were soft (i.e., non-zero trigger efficiency below the nominal threshold), and dimuon production is copious, so some dimuon events were recorded.

We have gone through the entire 1987 data set for all triggers and extracted the events with multiple muon candidates, using the loose matching cuts of table 3.1, no energy cut,

and no p_t cut. (The 1.4 GeV range-out energy of the calorimeter makes an effective p_t cut.) This yields 259 dimuon events. The resultant distributions show evidence of heavy flavor production, and hint at the potential of dimuons in future analyses. Before looking at the plots, a few words on the underlying physics.

Production Mechanics

Four main processes are of interest:

1. $p\bar{p} \rightarrow (J/\psi, \Upsilon) \rightarrow \mu^+\mu^-$
(Calorimeter isolation, resonances in invariant mass distribution.)
2. $p\bar{p} \rightarrow B\bar{B}$, $\bar{B} \rightarrow \mu^+\nu$ jet, $B \rightarrow \mu^-\bar{\nu}$ jet
(Back-to-back muons may overlap the jets.)
3. $p\bar{p} \rightarrow B\bar{B}$, $B \rightarrow \text{jet}$, $\bar{B} \rightarrow \mu^+\nu\bar{D}$, $\bar{D} \rightarrow \mu^-\nu K$
(Unlike-sign dimuon, not back-to-back, jet activity.)
4. $p\bar{p} \rightarrow B\bar{B}$, $B \rightarrow \mu^-\nu$ jet, $\bar{B} \rightarrow \bar{D} \rightarrow \mu^-\nu$ jet
(Like-sign dimuon, back-to-back, cascade μ^- is softer, jet activity.)
5. $p\bar{p} \rightarrow \mu^+\mu^-$ (Drell-Yan)
(Calorimeter isolation, invariant mass continuum.)
6. $B^0\bar{B}^0$ oscillations will contribute like-sign dimuons at a low rate.

Each process has its own topology, briefly described in parentheses in the list. The distinguishing features are the amount of calorimeter activity around the muons, and the relative signs of the muon charges. In the following we use these handles to explore the dimuon sample.

D.2 Invariant Mass Distribution

Figure D.1 shows the invariant mass distributions for like-sign and unlike-sign muon pairs. The unlike-sign plot shows a peak at $M_{\mu\mu} = 3 \text{ GeV}/c^2$, which is the mass of the J/ψ

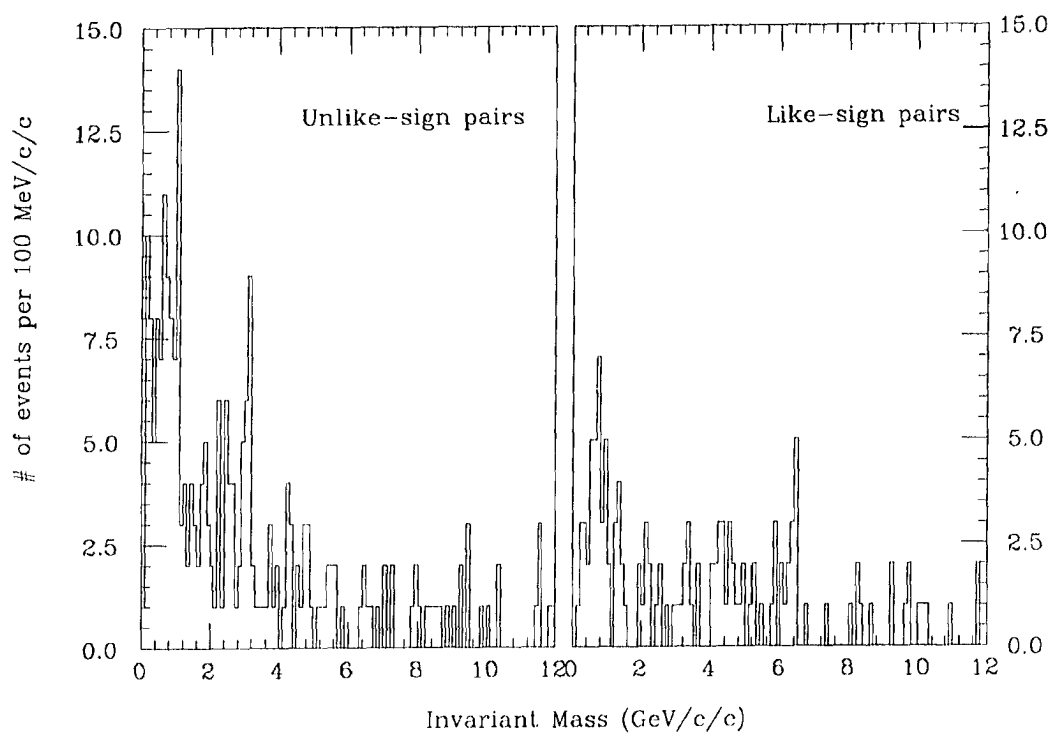


Figure D.1: Invariant mass of unlike- and like-charge muon pairs.

particle. The peak is spread over three 100 MeV bins, for an rms of 100-150 MeV. The momentum resolution of the CTC is

$$\delta p_t/p_t = 0.002p_t + 0.003$$

so that the invariant mass resolution is

$$\delta M_{\mu\mu}/M_{\mu\mu} > \sqrt{0.002(p_{t1}^2 + p_{t2}^2) + 0.006}.$$

The inequality arises because we take $\delta\theta = \delta\phi = 0$. For the simple case of $M_{\mu\mu} = 3$ GeV and $p_{t1} = p_{t2} = 3$ GeV/c, we expect $\delta M_{\mu\mu} = 40$ MeV. The errors from $(\delta\theta, \delta\phi)$ are comparable to the error from δp_t , so the width of the J/ψ peak is consistent with the detector resolution.

In the unlike-sign mass plot, there is also a spike in the bin corresponding to 1 GeV, which is the mass of the ϕ meson. There is no peak at the Υ mass, because the production cross section for the beauty meson is an order of magnitude less than for the charm meson [13].

Both plots peak at low $M_{\mu\mu}$. The ρ and ω particles would appear in these bins for the unlike-sign plot, but the large intrinsic width of the ρ ($\Gamma_\rho = 153$ MeV) convoluted with the detector resolution, the ρ peak is not sharp, and the small branching ratio for $\omega \rightarrow \mu^+\mu^-$ causes the ω to get lost in the noise. A more likely explanation for the dimuons with $M_{\mu\mu} < 1$ GeV is that they are an artifact of the p_t cut on the muon-candidates, which in this case is the range-out energy of 1.4 GeV for muons traversing the calorimeter, combined with the minimum acceptable opening angle of the dimuons in this analysis, which is a single calorimeter tower (see table 2.3). Pairs of fake muons with $1.4 < p_t < 2$ GeV and small $\Delta\phi$ (azimuth angle between the two fake muons) give $M_{\mu\mu} < 1$ GeV/c² for most fake dimuons. But the existence of even such a small J/ψ peak supports the claim that we are seeing real muons and not just junk.

D.3 Like and Unlike Charge Ratios

We call a fake dimuon a pair of muon candidates where one or both tracks is a fake muon. The track spectrum in the CTC is observed to have equal numbers of positively and negatively charged tracks[39]. Simple combinatorics requires equal numbers of like-sign

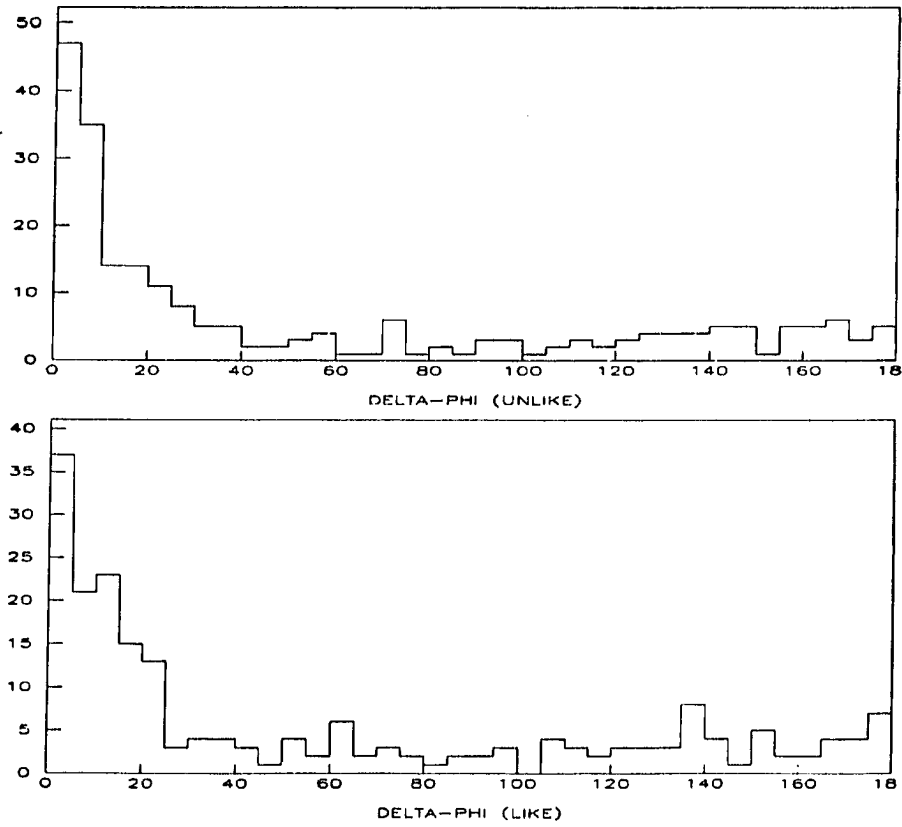


Figure D.2: Azimuth angle between the muons for unlike- and like-charge pairs.

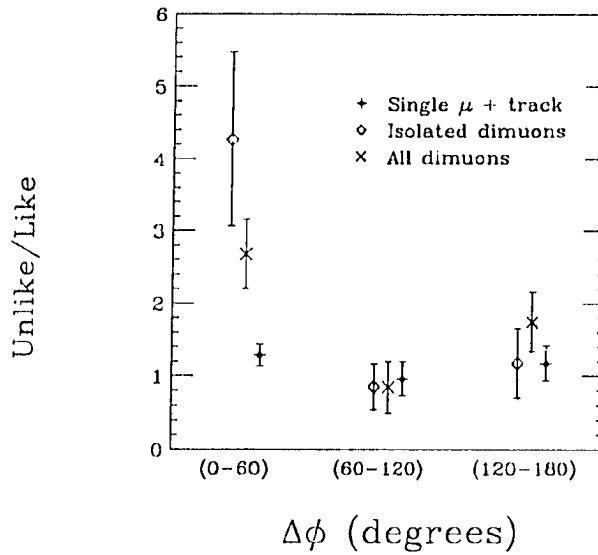


Figure D.3: Ratio of unlike-sign dimuons to like-sign pairs, for three ranges of the difference in azimuth angle between the two tracks. Single μ data provides a background estimate.

and unlike-sign fake dimuons. If we define

$$R \equiv \frac{N_{+-}}{N_{++} + N_{--}}$$

then for the background to a dimuon signal we expect $R_{bgrd} = 1$.

On the other hand, of the four dimuon production processes listed above, most generate unlike-sign muon pairs. The others processes are less frequent. Hence, for true dimuons one expects

$$R_{\mu\mu} > 1.$$

Figure D.2 shows the distribution of azimuth angles between the two muons. There are 175 entries in the unlike-sign plot and 84 entries in the unlike-sign plot, giving

$$R_{\mu\mu} = \frac{175}{84} = 2.1 \pm 0.3,$$

an apparent excess of unlike-sign pairs, consistent with the dimuon production via heavy flavor processes.

One can imagine mechanisms whereby the background would exhibit such an asymmetry. If both muon candidates were from shower leakage in the same jet, local charge conservation might create the observed excess. Or, some other effect could fake the signal. The best recourse is to empirically estimate R_{bgrd} from the data. Our method¹ is to take single muon data and loop over all tracks within the η coverage of the muon chambers, and with $p_t > 1.4$ GeV/c. Each track is paired with the muon, giving a sample of fake dimuons. We compare the calorimeter isolation and $\Delta\phi$ distributions of the fake muons with the dimuon-candidates. Figure D.3 shows some results. The $\Delta\phi$ distribution of figure D.2 is gathered into 3 bins of 60° each, and is compared with the same distribution for the fake dimuon sample and for dimuons with $\sum E_t < 5$ GeV within a cone of $dR = 0.6$ around each muon. For $\Delta\phi < 60^\circ$, $R_{\mu\mu} > 1$, consistent with heavy flavor semileptonic cascading (process 3 in the list, above.). But it is suspicious that no excess appears for $\Delta\phi > 120^\circ$, as we expect from process 2. The enhancement in $R_{\mu\mu}$ for isolated muons means that the dimuons do not come from shower leakage. Better statistics from the 1988 run will help us understand this effect.

¹This was Hans Grassman's idea. Thanks to Marco Incagli for the plots.

Appendix E

Rabbit Testing

Muons induce charge pulses on the wires of the central muon chambers, which are shaped and amplified by the Rabbit Muon ADC/TDC cards (“MAT”). The Rabbit system is described in reference [21]. There is one MAT per chamber (three per wedge), so 160 cards were made for the CMU system, including spares. Each card has a charge-to-voltage converter (QVC) for each end of a wire, and a time-to-voltage converter (TVC) for each wire, or 16 QVC’s and 8 TVC’s per board (see figure 2.14).

The Muon ADC/TDC circuit was designed and prototyped by Professor Holloway and the Fermilab Physics Instrumentation Group. A lowest-bid contractor made the boards, and the quality was lamentable: components were misplaced, missing, or damaged; solder overflowed creating shorts or was absent producing open circuits; the printed circuit had flaws creating shorts or open circuits. The boards required repair before they could be calibrated and used.

To this end, we built a test stand consisting of a Rabbit crate, a microcomputer, and timing circuitry. Referring to figure 2.13, cards in a Rabbit crate are controlled by a host processor (microcomputer or MX) via the EWE. The test stand used a simple version of the EWE called a EWESIM. The BAT card distributes timing gates to the other Rabbit cards, triggered by an external gate. In the test stand this external gate comes from the timing circuitry, assembled using computer controllable BBX electronics ¹. Figure E.1 shows the timing circuit. Extensive menu-driven computer programs facilitate use of the test stand for debugging and calibration [20].

Charge injection into the amplifier channels simulates chamber operation. A Rabbit card called a MUQMUX (for MUon charge(Q) MULTipleXing) injects a calibrated charge

¹BBX is the University of Illinois Black Box electronics, a modular computer-controlled system that is functionally similar to the more widely known CAMAC system.

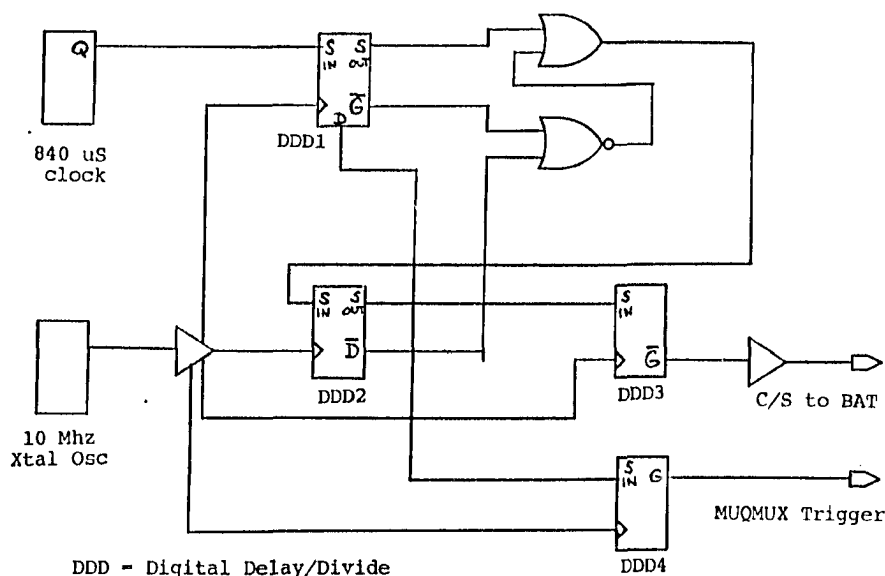


Figure E.1: Illinois BlackBox (BBX) electronics used for reference timing in calibration and debugging of the Muon ADC/TDC cards.

pulse into a selected amplifier channel in response to a front panel pulse from the BBX circuitry. The card uses the voltage from an addressable DAC to charge a precision capacitor. (The DAC is on a Rabbit card called, predictably, a Rabdac.) A front-panel pulse closes a solid-state switch to inject the charge through a multiplexer to the input of the selected MAT amplifier. The timing of the trigger pulse is computer variable, in 100 nanosecond steps.

The MAT cards have many features, each of which needs to be checked. Following is a brief outline of how each function is exercised. Table E.1 shows the checklist used during debugging and calibration.

Voltage

To protect the test stand from short circuits, we measured all supply voltages on a separate jig as a first step.

TCAL

This is a variable timing gate from the BAT that allows a crude test of the TVC circuits without an external charge pulse. We verify that TCAL triggers each TVC circuit.

Top and bottom multiplexers

A redundant feature of Rabbit is that amplifier outputs can be routed to the EWE via two separate paths. We measure the amplifier linearity both ways to detect weak links in the circuits.

Hit bits

The muon trigger level-1 card uses drift time information from the TVC circuits to reject muon candidates below a programmable transverse momentum threshold ('brass muons') [24]. When a charge pulse is above threshold, a digital level is asserted on a connector on the front panel of the MAT. We test the bits using a trigger level-1 card.

TVC threshold

A Rabbit crate is an electrically noisy environment. To make sure that a TVC is not started by a voltage transient, each TVC has a discriminator with a hardwired threshold. We test the thresholds by recording the size of the smallest charge pulses that produce a TVC output.

SKIP

For suppression of empty channels during data read out (sparse scan), a bit from each TVC is multiplexed to the Rabbit bus indicating the presence of a valid hit. To test the bit we built a special Rabbit card that latches the bits and routes them to the Rabbit digital data bus, whence they can be read by the microcomputer ².

Fast Analog Outs

The analog QVC output voltages for a ϕ -cell (that is, four wires lying on a radial centerline) are buffered, summed and passed to a front-panel connector. This pulse height information could provide a fast z -measurement by charge division, to refine the CTC/muon match of the golden trigger. To test the circuit, the voltages were cabled from the front connector to the SLAFMUX (see SKIP comments, and footnote), and then digitized and checked in the software.

²The board is called the SLAFMUX, for Skip Latch and Fast MultipleXer.

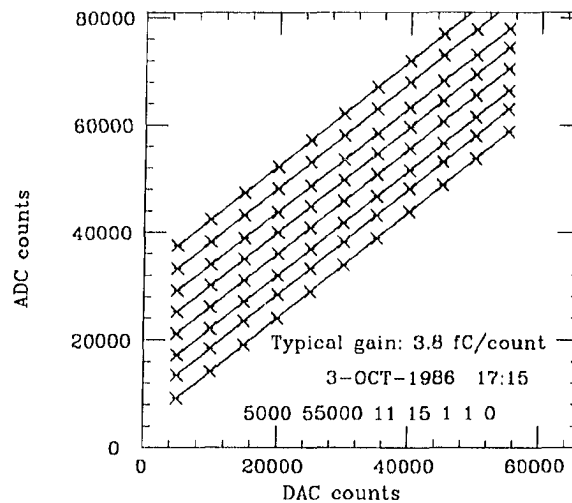


Figure E.2: Digitized QVC output voltage versus input charge, for eight QVC channels (artificial offsets for clarity).

PROM

Each MAT has a unique serial number, inscribed on the front panel and stored in a Programmable Read Only Memory chip. This is vital to make sure that the correct charge calibration constants are used in track reconstruction. The serial number is read from the card and stored along with the gains.

OTHER test

A properly functioning Rabbit card can prevent other cards in the crate from working, for example if it always controls the analog bus or address lines. The test crate is full of other cards, and we run a quick check of the other cards while the MAT under scrutiny is installed.

For a working board, the gains of the QVC's and TVC's had to be calibrated. Figure 2.14 shows that for the TVC, this is effectively measuring the output for the current source I and the capacitance C_3 , and that for the QVC it amounts to measuring the feedback capacitor C_4 . The approach was simple: we would inject a known charge at a known time into the amplifier input, and record the digitized output signals. Varying the amount of charge and the times gave enough points to fit a straight line to the data and obtain the gains in units of picoseconds per count or femtocoulombs per count. Figures E.2 and E.3

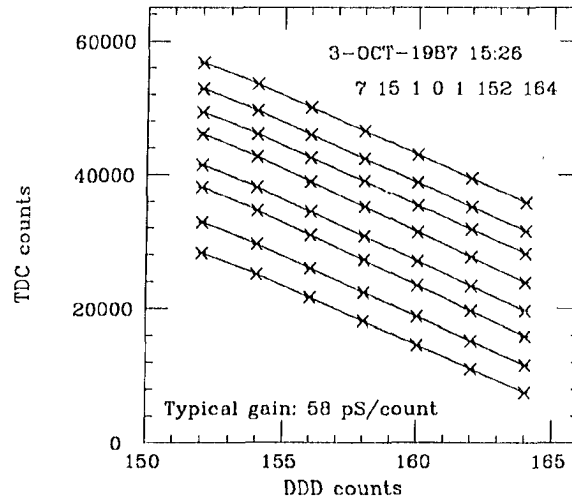


Figure E.3: Digitized TVC output voltage versus time of charge injection, for eight TVC channels (artificial offsets for clarity).

show typical charge calibration curves for a MAT card. The amount of charge injected into a QVC is

$$Q \text{ (pC)} = N_Q \times (38.13 \text{ } \mu\text{V/DAC}) \times (100 \text{ pF})$$

where N_Q is the value written to the Rabdac (“DAC counts”), 38.13 is the measured conversion between volts and DAC counts, and 100 pF is the value of the charge injection capacitor. (The Rabdac and Muqmux were designed so that 1 DAC count yields 1 ADC count from the MAT card after the injected charge has been digitized.) The time T of charge injection is varied using a BBX digital delay module (DDD4 in figure E.1),

$$T \text{ (nS)} = t_0 + N_T(100)$$

where N_T is the value written to the delay module (100 nS per count) and t_0 is some constant offset time. As the calibration plots show, the amplifiers are quite linear, and the channel-to-channel variation of the slopes is small, $< 1\%$ for the QVC’s and $< 5\%$ for the TVC’s. (Slopes and linearity are calculated and must be within tolerance before a card passes.) The gains are recorded in a database accessible to the muon pattern recognition code.

Muon QVC/TVC Rabbit Card Check List

Serial Number: _____

PROM contents: _____

1. Amplifier Tests who _____ when _____

TCAL TSCAN Results OK? _____

ASCAN Results OK? _____

MUQMUX TSCAN Result OK? _____

2. Feature Tests who _____ when _____

HIT/threshold Test OK? _____

Channel	Evens	Odds
1	_____	_____

SKIP Test OK? _____

FAO Test OK? _____

3. Calibrations

top bus QVC who _____ when _____ file name _____

4. Analysis who _____ when _____

\$QT run? _____

	.CAL files OK?	Plots OK?
top bus QVC	_____	_____

5. Pedestal Test who _____ when _____ (Attach results)

Table E.1: Abbreviated checklist for testing the Muon ADC/TDC Rabbit cards.

Bibliography

- [1] "The CDF Central Muon Detector", Ascoli et al, *Nucl Instr and Meth* **A268** (1988) 33.
- [2] T.K.Westhusing, Ph.D. thesis, University of Illinois at Urbana-Champaign (1988).
- [3] "A Measurement of Intermediate Vector Boson Production in 1.8 TeV $p\bar{p}$ Collisions", The CDF Collaboration (to be published in *Phys. Rev. Lett.*, 1989)
- [4] "Bottom-quark Production at Hadron Colliders", E. Berger, J. Collins, and D. Soper, *Phys Rev* **35D** (1987) 2272.
 "Heavy Quark Production in Hadron Collisions", E. Berger, ANL-HEP-PR-87-53 (1987).
- [5] "Physics at $\sqrt{s} = 2$ TeV: An Experimentalist's Perspective", R. Raja, FERMILAB-Pub-87/125-E, April 1987.
- [6] "Topics in Perturbative QCD at Collider Energies", R.K.Ellis, Proceedings of the UCLA Workshop on Observable Standard Model Physics (1986).
 "Heavy Particle Content in QCD Jets", A.H. Mueller and P. Nason, *Phys Lett* **157B** 226.
- [7] Professor T.M. Liss, University of Illinois at Urbana-Champaign Department of Physics, private communication.
- [8] R.D. Field and R.P.Feynmann, *Nucl Phys* **B136** (1978) 1.
- [9] G. Arnison et al (UA1 collaboration) *Phys Lett* **B276** (1986) 253.
- [10] "Observation of a Dimuon Resonance at 9.5 GeV in 400-GeV Proton-Nucleus Collisions", S.W. Herb et al, *Phys Rev Lett* **39** (1977) 252.
 "Direct Observation of the Decay of Beauty Particles into Charm Particles", J.P.Albanese et al, *Phys Lett* **158B** (1985) 186.

- [11] D.H.Perkins, Introduction to High Energy Physics, second edition (Addison-Wesley, Reading, Massachusetts 1982).
- [12] I.J.R. Aitchison and A.J.G.Hey, Gauge Theories in Particle Physics (Adam Hilger, Bristol, 1982).
- [13] “Dimuon Production at the CERN $p\bar{p}$ Collider”, Hans-Günther Moser, Ph.D. thesis, Technische Hochschule Aachen (1987).
- [14] “Strong and Weak Production of Beauty and Charm at the CERN $p\bar{p}$ Collider”, J.T.Ransdell, Ph.D. thesis, University of California at Riverside (1987).
- [15] “Study of Heavy Flavor Production in Events with a Muon Accompanied by Jet(s) at the CERN $p\bar{p}$ Collider”, C. Albajar et al (UA1 Collaboration) CERN-EP/87-189, 6 October 1987.
- [16] “Measurement of the Decay $B^0 \rightarrow D^* \ell^+ \nu$ ”, H. Albrecht et al (ARGUS collaboration), *Phys Lett* **197B** (1987) 452.
- [17] F.Paige and S.Protopopescu, ISAJET Monte Carlo, BNL-38034 (1986).
- [18] E.Eichten, I.Hinchliff, K.Lane, and C.Quigg, *Rev Mod Phys* **56** (1984) 579
- [19] “Principles of Operation of Multiwire Proportional and Drift Chambers”, F. Sauli, CERN 77-09, 3 May 1977
- [20] “Device Diagnostic Language Users Manual”, David D. Lesny, University of Illinois at Urbana-Champaign, Department of Physics, Publication C00-1195-478 (1987)
- [21] “CDF Front End Electronics: the RABBIT System”, G. Drake et al, *Nucl. Instr. and Meth.* **A269** (1988) pp. 68-81
- [22] “A Fast Hardware Track Finder for the CDF Central Tracking Chamber”, G.W. Foster et al, *Nucl. Instr. and Meth.* **A269** (1988) pp. 93-100
- [23] “An Alignment System for the CDF Central Muon Chambers”, G. Ascoli et al. *Nucl. Instr. and Meth.* **A268** (1988) pp. 41-45

- [24] "CDF Central Muon System Level 1 Trigger", G. Ascoli et al. *Nucl. Instr. and Meth.* **A269** (1988) pp. 63-67
- [25] "A Two Level FastBus Based Trigger System for CDF", D. Amidei et al, *Nucl. Instr. and Meth.* **A269** (1988) pp. 51-62
- [26] R. Leuchs, Ph.D. thesis, Technische Hochschule Aachen (1982).
- [27] " Inclusive Charged Particle Production at the CERN $p\bar{p}$ Collider ", M. Banner et al (UA2 collaboration) *Phys Lett* **122B** (1983) 322.
 "Kaon Production in $p\bar{p}$ Collisions at a Centre-of-Mass Energy of 540 GeV", G.J. Alner et al (UA5 collaboration), *Nucl Phys* **B258** (1985) 505.
 CDF results on K^0 cross sections and $\frac{K}{\pi}$ fractions appear in the following two references:
 PhD Thesis by Martin H. Schub, Purdue University, (1989) (In preparation).
 Proceedings of the XIXth International Symposium on Multiparticle Dynamics, Arles, France. (presentation by Franco Bedeschi) CDF-745 (1988).
- [28] "Pion and Kaon Decay in the CTC Volume Faking a High p_t Track", John Skarha, CDF-587 (1987).
- [29] "Measurement of the Inclusive Jet Cross Section at the Tevatron $p\bar{p}$ Collider", The CDF Collaboration (to be published in *Phys. Rev. Lett.*, 1989)
- [30] "Absorbtion Cross Sections of π^\pm , K^\pm , p , and \bar{p} on Nuclei Between 60 and 280 GeV/c", Carroll et al, *Phys Lett* **80B** (1979) 319.
- [31] "Neutron-Nucleus Inelastic Cross Sections from 160 to 375 GeV/c", Roberts et al, *Nucl Phys* **B159** (1979) 56.
- [32] "Absorbtion Cross Sections for Pions, Kaons, Protons, and Antiprotons on Complex Nuclei in the 6 to 60 GeV/c Moimentum Range", Denisov et al, *Nucl Phys* **B61** (1973) 62.
- [33] "Proton-Nuclei Cross Sections at 20 GeV", Belletini et al, *Nucl Phys* **79** (1966) 609.
- [34] "A Study of the Effects of Leakage in the CDF Calorimetry Using E616 (CIFT) Hadron Test Data", John Yoh, CDF-110 (1981).

- [35] "Measurement of Hadronic and Electromagnetic Shower Development Between 10 GeV and 140 GeV by an Iron-Scintillator Calorimeter", CDHS Internal Report, Emylyn Hughes.
- [36] "Pion Punchthrough Probability in the Central Calorimeter", D.A. Smith and H.B. Jensen, CDF-707 (1988)
- [37] "Decay-in-Flight Acceptance of the Central Muon Chambers", D.A. Smith and T.K. Westhusing, CDF-726 (1988)
- [38] "The CDF Central Electromagnetic Calorimeter", Balka et al, *Nucl Instr and Meth* **A267** (1988) 272.
- [39] "Transverse Momentum Distributions of Charged Particles Produced in $p\bar{p}$ Interactions at $\sqrt{s} = 630$ and 1800 GeV", F. Abe et al (The CDF Collaboration) *Phys. Rev. Lett.* **61** (17 October 1988) 1819.

Vita

David Austen Smith

He continued his studies at the University of California at Berkeley and received a B.A. in physics in 1981. Then, graduate school at the University of Illinois. After earning an M.S. in physics, he won a fellowship for a year at the Ecole Polytechnique in Paris. Years after his return to Urbana, in 1988, he completed the PhD degree and lived happily ever after.



2017 ProQuest Distribution Agreement

This Agreement is between the author (Author) and ProQuest LLC, through its ProQuest Dissertation Distribution business (formerly ProQuest/UMI). Under this Agreement, Author grants ProQuest certain rights to preserve, archive and distribute the dissertation or thesis (the Work), abstract, and index terms provided by Author to ProQuest.

Section I. License for Inclusion of the Work in ProQuest Publishing Program

Grant of Rights. Author hereby grants to ProQuest the **non-exclusive**, worldwide right to reproduce, distribute, display and transmit the Work (in whole or in part) in such tangible and electronic formats as may be in existence now or developed in the future. Author further grants to ProQuest the right to include the abstract, bibliography and other metadata in the ProQuest Dissertations & Theses database (PQDT) and in ProQuest Dissertation Abstracts International and any successor or related index and/or finding products or services.

ProQuest Publishing Program - Election and Elements. The rights granted above shall be exercised according to the publishing option selected by Author in Section III, Author Options, and subject to the following additional Publishing Program requirements:

- **Distribution of the Work.** Except as restricted by Author in the publishing option selected, the rights granted by Author automatically include (1) the right to allow sale and distribution of the Work, in whole or in part, by ProQuest and its sales agents and distributors and (2) the right to make the Abstract, bibliographic data and any meta data associated with the Work available to search engines and harvesters.
- **Restrictions.** ProQuest will use commercially reasonable efforts to restrict the distribution of the Work as provided under the publishing option selected by Author or *as later elected by Author* through direct contact with ProQuest. Such election is subject to Author's Degree Granting Institution Directives. With respect to restrictions requested after submission of the Work, Author acknowledges that ProQuest cannot recall or amend previously distributed versions of the Work.
- **Removal of Work from the Program.** ProQuest may elect not to distribute the Work if it believes that all necessary rights of third parties have not been secured. Refer to the website http://www.proquest.com/products_umi/dissertations/ for information about copyright and your dissertation or thesis. If Author's degree is rescinded, and/or the degree-granting institution so directs, ProQuest will expunge the Work from its publishing program in accordance with its then current publishing policies.
- **Degree Granting Institution Directives.** Author is solely responsible for any conflict between policies and directions of Author's degree-granting institution, Author's choice of publishing model, and/or any restriction Author places on the use of the Work. For the avoidance of doubt, ProQuest is not responsible for access to the Work that is provided by Author's degree-granting institution through its library or institutional repository. Author must work directly with Author's degree granting institution to ensure application of any restrictions to access relating to the Work by Author's degree granting institution.

Delivery of the Work. Author shall provide to ProQuest the Work and all necessary supporting documents during the online submission process, according to the Instructions accompanying this agreement.

Rights Verification. Author represents and warrants that Author is the copyright holder of the Work and has obtained all necessary rights to permit ProQuest to reproduce and distribute third party materials contained in any part of the Work, including all necessary licenses for any non-public, third party software necessary to access, display, and run or print the Work. Author is solely responsible and will indemnify ProQuest for any third party claims related to the Work as submitted for publication.

Open Access Publishing Plus

☒ **YES** I want the broadest possible dissemination of my work, and I want to provide free global access to the electronic copy of my work via the internet.

☒ **YES** I understand that I will not be eligible to receive royalties.

I want major search engines (e.g. Google, Yahoo) to discover my work. Learn more: <http://www.proquest.com/en-US/products/dissertations/google.shtml>

☐ **Yes**
☒ **No**

Acknowledgment: I have read, understand and agree to this ProQuest Publishing Agreement, including all rights and restrictions included within the publishing option chosen by me as indicated above.

REQUIRED Author's signature _____ Date 5 July 2017

(Print Name) David Austen Smith

Institution conferring degree University of Illinois at Urbana-Champaign

Dissertation/Master's Thesis Submission Form

Please print clearly in block letters

☐ M (Master's Thesis)

☒ D (Dissertation)

Personal Information

Last Name _____ Smith _____ Middle Name or Initial _____ Austen _____
First Name _____ David _____ Country (ies) of Citizenship _____

Degree & Dissertation Information

Title of Dissertation/ Thesis Study of muons associated with jets in proton-antiproton collisions at sqrt(s) = 1.8 TeV _____
Institution conferring degree _____ University of Illinois at Urbana-Champaign _____ Degree awarded (abbreviate; e.g., Ph.D.) _____ PhD _____
College, School, or Division _____ Year degree awarded _____ 1989 _____
Department or Program _____ Physics _____ Year manuscript completed _____ 1988 _____
Advisory/Committee Chair _____ Lee Holloway _____
Committee Member _____ Jim Wiss _____ Committee Member _____
Committee Member _____ Committee Member _____
Committee Member _____ Committee Member _____

Language of manuscript _____
Primary Subject Category: Enter the 4-digit code and category name from the Subject Category Guide that most closely describes the area of your research. Code_0798_ Category_particle physics _____

You may suggest two additional subject categories that may aid in the discovery of your work in our digital database.

Code_____ Category_____ Code_____ Category_____

Provide up to 6 keywords or short phrases for citation indices, library cataloging, and database searching.

_____ collider detector at fermilab _____ _____ muon detection _____ _____ jet production _____
_____ proton-antiproton collisions _____ _____ pion punchthrough _____ _____

Current Contact Information

Current Email Address _____ smith@cenbg.in2p3.fr _____

Street Address _____

Please provide your postal address if you are interested in receiving royalties on sales of your thesis.

City _____ Province _____ Daytime Phone +33 5 57 12 08 91

Country _____ Postal Code _____ Evening Phone +33 6 85 89 66 38

Permanent Contact Information

Permanent Email Address _____ smith@cenbg.in2p3.fr _____

Street Address (line 1) _____ CENBG, 19 rue du Solarium _____

City Gradignan Province _____ Future Phone _____

Country France Postal Code 33170 Alternate Future Phone _____

THIS PAGE MUST ACCOMPANY YOUR MANUSCRIPT AND THE REST OF YOUR SUBMISSION MATERIALS

Subject Categories

The ProQuest Dissertations & Theses (PQDT) database and the ProQuest citation indices are arranged by subject categories. Please select the one category below that best describes your field of research or creative work. You may add one or two additional categories on your submission form that will also be associated with your work as secondary subjects.

Arts, Business, Education, Humanities, and Social Sciences

AREA, ETHNIC, AND GENDER STUDIES

African American studies	0296
African studies	0293
American studies	0323
Asian American studies	0343
Asian studies	0342
Baltic studies	0361
Black studies	0325
Canadian studies	0385
Caribbean studies	0432
Classical studies	0434
East European studies	0437
Ethnic studies	0631
European studies	0440
French Canadian culture	0482
Gender studies	0733
GLBT studies	0492
Hispanic American studies	0737
Holocaust studies	0507
Islamic culture	0512
Judaic studies	0751
Latin American studies	0550
Middle Eastern studies	0555
Native American studies	0740
Near Eastern studies	0559
North African studies	0560
Pacific Rim studies	0561
Regional studies	0604
Scandinavian studies	0613
Slavic studies	0614
South African studies	0654
South Asian studies	0638
Sub Saharan Africa studies	0639
Women's studies	0453

BUSINESS

Accounting	0272
Arts management	0424
Banking	0770
Business	0310
Entrepreneurship	0429
Finance	0508
Management	0454
Marketing	0338
Sports management	0430

COMMUNICATIONS AND INFORMATION SCIENCES

Communication	0459
Information science	0723
Journalism	0391
Library science	0399
Mass communication	0708
Technical communication	0643
Web studies	0646

FINE AND PERFORMING ARTS

Art criticism	0365
Art history	0377
Cinematography	0435
Dance	0378
Design	0389
Film studies	0900
Fine arts	0357
Music	0413
Performing arts	0641
Theater	0465
Theater history	0644

EDUCATION

Adult education	0516
Art education	0273
Bilingual education	0282
Business education	0688
Community college education	0275
Continuing education	0651
Curriculum development	0727
Early childhood education	0518
Education	0515
Education finance	0277
Education policy	0458
Educational administration	0514
Educational evaluation	0443
Educational leadership	0449
Educational psychology	0525
Educational technology	0710
Educational tests & measurements	0288
Elementary education	0524
English as a second language	0441
Foreign language instruction	0444
Gifted education	0445
Health education	0680
Higher education	0745
Higher education administration	0446
History of education	0520
Home economics education	0278
Industrial arts education	0521
Instructional design	0447
Language arts	0279
Mathematics education	0280
Middle school education	0450
Multicultural education	0455
Music education	0522
Pedagogy	0456
Performing arts education	0457
Philosophy of education	0998
Physical education	0523
Reading instruction	0535
Religious education	0527
School counseling	0519
Science education	0714
Secondary education	0533
Social sciences education	0534
Sociology of education	0340
Special education	0529
Teacher education	0530
Vocational education	0747

HUMANITIES

HISTORY

African history	0331
American history	0337
Ancient history	0579
Asian history	0332
Black history	0328
Canadian history	0334
European history	0335
History	0578
History of Oceania	0504
History of science	0585
Latin American history	0336
Medieval history	0581
Middle Eastern history	0333
Military history	0772
Modern history	0582
Russian history	0724
World history	0506

LANGUAGE & LITERATURE

African literature	0316
American literature	0591
Ancient languages	0289
Asian literature	0305
British and Irish literature	0593
Canadian literature	0352
Caribbean literature	0360
Classical literature	0294
Comparative literature	0295
English literature	0593
French Canadian literature	0355
Germanic literature	0311
Icelandic & Scandinavian literature	0362
Language	0679
Latin American literature	0312
Linguistics	0290
Literature	0401
Literature of Oceania	0356
Medieval literature	0297
Middle Eastern literature	0315
Modern language	0291
Modern literature	0298
Rhetoric	0681
Romance literature	0313
Slavic literature	0314

PHILOSOPHY AND RELIGION

Aesthetics	0650
Biblical studies	0321
Canon law	0375
Clerical studies	0319
Comparative religion	0618
Divinity	0376
Epistemology	0393
Ethics	0394
Logic	0395
Metaphysics	0396
Pastoral counseling	0397
Philosophy	0422
Philosophy of Religion	0322
Philosophy of science	0402
Religion	0318
Religious history	0320
Spirituality	0647
Theology	0469

LAW AND LEGAL STUDIES

Alternative dispute resolution	0649
Intellectual property	0513
International law	0616
Law	0398
Patent law	0562

SOCIAL SCIENCES

Archaeology	0324
Area planning and development	0341
Criminology	0627
Cultural anthropology	0326
Demography	0938
Economic history	0509
Economic theory	0511
Economics	0501
Economics, Commerce-Business	0505
Economics, Labor	0510
Folklore	0358
Forensic anthropology	0339
Geography	0366
Individual & family studies	0628
International relations	0601
Labor relations	0629
Military studies	0750
Organization theory	0635
Organizational behavior	0703
Peace studies	0563
Physical anthropology	0327
Political Science	0615
Public administration	0617
Public policy	0630
Recreation and tourism	0814
Social research	0344
Social structure	0700
Social work	0452
Sociolinguistics	0636
Sociology	0626
Transportation planning	0709
Urban planning	0999

INTERDISCIPLINARY

Alternative energy	0363
Biographies	0304
Climate change	0404
Cultural resources management	0436
Energy	0791
Food science	0359
Home economics	0386
Information technology	0489
Multimedia	0558
Museum studies	0730
Sustainability	0640
Textile research	0994
Wood sciences	0746

Behavioral, Natural, and Physical Sciences

AGRICULTURE

Agriculture	0473
Agronomy	0285
Animal diseases	0476
Animal sciences	0475
Fisheries and aquatic sciences	0792
Forestry	0478
Horticulture	0471
Plant pathology	0480
Plant sciences	0479
Range management	0777
Soil sciences	0481
Urban forestry	0281
Wildlife management	0286

ARCHITECTURE

Architecture	0729
Architectural engineering	0462
Landscape architecture	0390

BEHAVIORAL SCIENCES

Animal behavior	0602
Behavioral sciences	0384
Clinical psychology	0622
Cognitive psychology	0633
Counseling psychology	0603
Developmental psychology	0620
Experimental psychology	0623
Occupational psychology	0624
Personality psychology	0625
Physiological psychology	0989
Psychobiology	0349
Psychology	0621
Quantitative psychology and psychometrics	0632
Social psychology	0451

BIOLOGICAL SCIENCES

Biochemistry	0487
Bioinformatics	0715
Biology	0306
Biomechanics	0648
Biophysics	0786
Biostatistics	0308
Cellular biology	0379
Developmental biology	0758
Endocrinology	0409
Entomology	0353
Evolution & development	0412
Genetics	0369
Histology	0414
Limnology	0793
Microbiology	0410
Molecular biology	0307
Morphology	0287
Neurosciences	0317
Parasitology	0718
Physiology	0719
Plant biology	0309
Systematic biology	0423
Virology	0720
Zoology	0472

ECOSYSTEM SCIENCES

Ecology	0329
Macroecology	0420
Paleoecology	0426

ENGINEERING

Aerospace engineering	0538
Artificial intelligence	0800
Automotive engineering	0540
Biomedical engineering	0541
Chemical engineering	0542
Civil engineering	0543
Computer engineering	0464
Computer science	0984
Electrical engineering	0544
Engineering	0537
Geological engineering	0466
Geophysical engineering	0467
Geotechnology	0428
Industrial engineering	0546
Mechanical engineering	0548
Mining engineering	0551
Naval engineering	0468
Nanotechnology	0652
Nuclear engineering	0552
Ocean engineering	0547
Operations research	0796
Packaging	0549
Petroleum engineering	0765
Plastics	0795
Robotics	0771
System science	0790

ENVIRONMENTAL SCIENCES

Conservation biology	0408
Environmental economics	0438
Environmental education	0442
Environmental engineering	0775
Environmental geology	0407
Environmental health	0470
Environmental justice	0619
Environmental law	0439
Environmental management	0474
Environmental philosophy	0392
Environmental science	0768
Environmental studies	0477
Land use planning	0536
Natural resource management	0528
Water resources management	0595
Wildlife conservation	0284

GEOSCIENCES

Aeronomy	0367
Atmospheric chemistry	0371
Atmospheric sciences	0725
Biogeochemistry	0425
Biological oceanography	0416
Chemical oceanography	0403
Continental dynamics	0406
Geobiology	0483
Geochemistry	0996
Geographic information science and geodesy	0370
Geology	0372
Geomorphology	0484
Geophysics	0373
Hydrologic sciences	0388
Marine geology	0556
Meteorology	0557
Mineralogy	0411
Paleoclimate science	0653
Paleontology	0418
Petroleum geology	0583
Petrology	0584
Physical geography	0368
Physical oceanography	0415
Planetology	0590
Plate tectonics	0592
Remote sensing	0799
Sedimentary geology	0594

HEALTH AND MEDICAL SCIENCES

Aging	0493
Alternative medicine	0496
Audiology	0300
Dentistry	0567
Epidemiology	0766
Gerontology	0351
Health care management	0769
Health sciences	0566
Immunology	0982
Kinesiology	0575
Medical ethics	0497
Medical imaging and radiology	0574
Medicine	0564
Mental health	0347
Nursing	0569
Nutrition	0570
Obstetrics and gynecology	0380
Occupational health	0354
Occupational therapy	0498
Oncology	0992
Ophthalmology	0381
Osteopathic medicine	0499
Pathology	0571
Pharmaceutical sciences	0572
Pharmacology	0419
Physical therapy	0382
Public health	0573
Public health occupations education	0500
Speech therapy	0460
Surgery	0576
Toxicology	0383
Veterinary medicine	0778

**MATHEMATICAL AND
PHYSICAL SCIENCES**

Acoustics	0986
Analytical chemistry	0486
Applied mathematics	0364
Astronomy	0606
Astrophysics	0596
Atomic physics	0748
Chemistry	0485
Condensed matter physics	0611
Electromagnetics	0607
High temperature physics	0597
Inorganic chemistry	0488
Low temperature physics	0598
Materials science	0794
Mathematics	0405
Mechanics	0346
Molecular chemistry	0431
Molecular physics	0609
Nanoscience	0565
Nuclear chemistry	0738
Nuclear physics	0756
Optics	0752
Organic chemistry	0490
Particle physics	0798
Physical chemistry	0494
Physics	0605
Plasma physics	0759
Polymer chemistry	0495
Quantum physics	0599
Statistics	0463
Theoretical mathematics	0642
Theoretical physics	0753